Photoelectron holography of semiconductor interfaces and study of MBE-grown GaAs(111) surfaces
by Jianchao Wu

A thesis submitted in partial fulfillment of the requirements for the degree of Doctor of Philosophy in Physics
Montana State University
© Copyright by Jianchao Wu (1996)

Abstract:
The microscopic structures and properties of semiconductor surfaces and interfaces are successfully investigated by several different techniques in this thesis.

First, the small cone photoelectron holographic imaging technique, in conjunction with the LEED observation, has been applied to study the interfacial structures of Se/Ge(100)-lx2, Ga/Ge(111)-1x1 and Ge/Si(100)-2xl samples. The results for the Se/Ge(100)-lx2 suggest that two different regions coexist on the surface. One is fully terminated by Se adatoms at bridge sites, and another is half-covered by Se adatoms on the Ge displaced surface. This is the first experiment to determine the atomic structure of Se/Ge(100)-1x2 sample. The results for the GaZGe(111)-1x1 unambiguously show that the Ga atoms occupy both T4 sites and H3 sites. The results for the GeZSi(100)-2x1 clearly indicate that the Ge adsorption displaces the surface Si atoms from the terraces and forms the Ge dimers on the surface. This determination is in agreement with the combined results of the studies by LEEM, LEED and STM [41].

Second, the GaAs(111)A and GaAs(111)B surfaces, prepared by the MBE growth technique, have been studied by HREELS, XPS, UPS and LEED. The MBE growth with Si-doping produces a p-type semiconductor for GaAs(111)A and a n-type for GaAs(111)B, and both surfaces have the same 2x2 reconstruction. The HREELS results from the clean GaAs(111)A and GaAs(111)B surfaces show the Fuchs-Kleiwer surface optical phonon energy at 35.5 meV, but different plasmon-excitation features. Following atomic hydrogen exposure, both As-H and Ga-H stretching modes are observed on the GaAs(111)B surface, while only Ga-H stretching mode appears in the HREELS spectra of GaAs(111)A surface, which can be explained by the Ga-vacancy buckling model of GaAs(111)A[48]. The hydrogen disruption is observed on the GaAs(111)B surface, but it does not take place on the GaAs(111)A surface.

PHOTOELECTRON HOLOGRAPHY OF SEMICONDUCTOR INTERFACES AND STUDY OF MBE-GROWN GaAs(111) SURFACES

by

Jianchao Wu

A thesis submitted in partial fulfillment

of the requirements for the degree

of

Doctor of Philosophy

in

Physics

MONTANA STATE UNIVERSITY

Bozeman, Montana

April, 1996

D378
W9501

APPROVAL

of a thesis submitted by

Jianchao Wu

This thesis has been read by each member of the thesis committee and has been found to be satisfactory regarding content, English usage, format, citations, bibliographic style, and consistency, and is ready for submission to the College of Graduate Studies.

4/16/96
Date

Chairperson, Graduate committee

Approved for the Major Department

5-1-96
Date

Head, Major Department

Approved for the College of Graduate Studies

5/10/96
Date

Graduate Dean

STATEMENT OF PERMISSION TO USE

In presenting this thesis in partial fulfillment of the requirements for a doctoral degree at Montana State University-Bozeman, I agree that the Library shall make it available to borrowers under rules of the Library. I further agree that copying of this thesis is allowable only for scholarly purposes, consistent with "fair use" as prescribed in the U.S. Copyright Law. Requests for extensive copying or reproduction of the thesis should be referred to University Microfilms International, 300 North Zeeb Road, Ann Arbor, Michigan 48106, to whom I have granted "the exclusive right to reproduce and distribute my dissertation in and from microform along with the non-exclusive right to reproduce and distribute my abstract in any format in whole or in part."

Signature Jianchao Wu

Date 4-12-96

DEDICATED TO WEILING, PHILIP, LINSEN

AND MY PARENTS

ACKNOWLEDGMENTS

I am very grateful to my thesis advisor, Dr. Gerald J. Lapeyre. His guidance and support throughout past six years enabled me to successfully complete this work. Thank you Jerry!

I would like to thank Dr. James R. Anderson for the advice and support to my training in surface science and experimental aspect of this work. His reading and correcting this thesis is especially appreciated. The author also acknowledges Dr. Cliff Olson at Synchrotron Radiation Center (SRC) for the valuable advice and assistance regarding the monochromators and other experimental apparatus. I would also like to thank Dr. J. Schaefer for his guidance during the early stage of HREELS work. The author would also like to thank the other committee members, Dr. John Hermanson, Dr. Richard Smith and Dr. George Tuthill, for their comments regarding the improvement of this thesis.

The author would like to thank Dr. Huasheng Wu, whose advice and support have been especially valuable. I would also like to thank Dr. Hong Yu. I learned a lot of vacuum techniques in working with him. The author is very grateful to Dr. Mary Keeffe and Cui Chen for their great help and contribution in the experimental setup and data collection at SRC. I would also like to thank the secretarial and technical staff at the MSU Physics Department for their assistance and support.

Finally, a warm thank goes to my wife, Weiling, for her loving care of our little children while working as a full-time engineer, great contribution and sacrifices to our family.

TABLE OF CONTENTS

APPROVAL ii

STATEMENT OF PERMISSION OF USE iii

ACKNOWLEDGMENTS v

TABLE OF CONTENTS vi

LIST OF TABLES ix

LIST OF FIGURES x

ABSTRACT xiii

1. INTRODUCTION 1
   - Motivation of the Present Work and Structure of the Thesis 2
   - Photoelectron Diffraction and Holography 3
   - Study of MBE-grown GaAs(111) Surfaces 5

2. PRINCIPLES OF PHOTOELECTRON HOLOGRAPHY 6
   - Angular Resolved Photoemission 6
   - Photoexcitation Factor 8
   - Atomic Scattering Factor 12
   - Photoelectron Diffraction 13
   - Holographic Inversion 16
   - Small-cone Summation 19
   - Effects of Multiple-Scattering 21

3. EXPERIMENTAL EQUIPMENT AND PROCEDURES OF PHOTOELECTRON HOLOGRAPHY 25

Synchrotron Radiation Photon Source 25

A Combined ERG-Seya Beamline 27

Electron Energy Analyzer 28

Sample Preparation 29

Data Acquisition and Analysis Procedures 32

4. INSTRUMENTATION AND EXPERIMENTAL PROCEDURES FOR STUDIES OF MBE-GROWN GaAs(111) SURFACES 37

Instrumental Layout 37

Molecular Beam Epitaxy System 40

High Resolution Electron Energy Loss Spectroscopy 41

XPS, UPS and LEED 42

Sample Preparation 43

5. EXPERIMENTAL RESULTS AND DISCUSSIONS OF PHOTOELECTRON HOLOGRAPHY 45

Se/Ge(100)-1x2 45

Ga/Ge(111)-1x1 60

Ge/Si(100)-2x1 73

6. EXPERIMENTAL RESULTS AND DISCUSSIONS OF STUDIES OF MBE-GROWN GaAs(111) SURFACES 85

Introduction 85

MBE-grown GaAs(111)A 88

LEED, XPS and UPS Studies 88

HREELS Studies 93

MBE-grown GaAs(111)B 101

7. CONCLUSIONS 109

REFERENCES 112

LIST OF TABLES

Table | Page

1. The Ge atom positions for the Se/Ge(100)-1x2 sample 57

2. The atomic positions for Ga/Ge(111)-1x1 system 62

3. Comparison of the bond lengths between this work and theoretical calculation 62

4. Positions of the Si atoms in the images for Ge/Si(100)-2x1 system 75

5. Comparison of the bond lengths obtained from different groups for Ge/Si(100)-2x1 .. 75

LIST OF FIGURES

Figure Page

1. The photoemission phenomenon 6
2. Energy-level diagram for photoemission process 7
3. Initial and final momentum states in scattering 11
4. The phenomenon of photoelectron diffraction 13
5. Intensity loci due to scattering path differences 19
6. The chosen small-cone with a half width w for a given position **R** 21
7. Phase and amplitude of the CIS inversion vs. polar angle for Ga/Ge(111)-1x1 23
8. Drawing of single- and multiple- scattering contours 24
9. Diagram of synchrotron radiation storage ring 26
10. Layout of ERG-SEYA Namioka monochromators 27
11. Layout of the hemispherical analyzer 29
12. Layout of vacuum system for photoelectron holographic experiment 31
13. Drawings of measured CIS emission directions of (111) and (100) surfaces 33
14. A typical EDC of Ge 3d and its Gaussian line-fitting for Ge/Si(100)-2x1 34
15. A CIS curve I(k) and its normalized curve $\chi(k)$ for Ge/Si(100)-2x1 36
16. Diagram of the MBE system 38
17. Analysis chamber layout 39
18. Diagram of a and a 4^0 miscut Ge(100) surfaces 46
19. A CIS curve I(k) and its normalized curve $\chi(k)$ for Se/Ge(100)-1x2 49

20. Phase and amplitude of the CIS inversion vs. polar angle for Se/Ge(100)-1x2 50

21. Some CIS I(k) curves and their non-diffractive curves $I_0(k)$ for Se/Ge(100)-1x2 51

22. Planar cuts of the image function for Se/Ge(100)-1x2 52

23. Line scans passing through the spot B for Se/Ge(100)-1x2 55

24. Drawings of 2x1 and 1x2 single-domain LEED patterns 58

25. Diagram of the structure for Se/Ge(100)-1x2 59

26. Representation of LEED and real-space structures in top view for Ge(111)-c(2x8)... 63

27. Energy distribution curve at hν=130 eV for Ga/Ge(111)-1x1 64

28. A CIS curve I(k) and its normalized curve $\chi(k)$ for Ga/Ge(111)-1x1 65

29. Some CIS I(k) curves and their non-diffractive curves $I_0(k)$ for Ga/Ge(111)-1x1 66

30. Planar cuts of the image function for Ga/Ge(111)-1x1 67

31. Line scans passing through the spot A for Ga/Ge(111)-1x1 71

32. Diagram of the Ga atom's positions at T_4 and H_3 sites for Ga/Ge(111)-1x1 72

33. Energy distribution curve at hν=150 eV for Ge/Si(100)-2x1 76

34. Phase and amplitude of the CIS inversion vs. polar angle for Ge/Si(100)-2x1 77

35. Some CIS I(k) curves and their non-diffractive curves $I_0(k)$ for Ge/Si(100)-2x1 78

36. Planar cuts of the image function for Ge/Si(100)-2x1 79

37. Line scans passing through the spot B for Ge/Si(100)-2x1 82

38. Schematics of the Si(100)-2x1 and Ge/Si(100)-2x1 surface reconstruction 83

39. Indication of a Ge-Ge dimer in real-space and in holographic image 84

40. HREELS phenomenon 87

41. Changes in the line shapes of Ga 3d and As 3d due to hydrogen adsorption..............90

42. GaAs(111)A vacancy buckling model..91

43. Energy-level diagram at the surface for p-type GaAs(111)A......................................93

44. HREELS spectra at different primary beam energies for GaAs(111)A surface..........98

45. HREELS spectra at a series of hydrogen coverages for GaAs(111)A.........................99

46. Hydrogen uptake curve for GaAs(111)A...100

47. Structure of hydrogen adsorbed GaAs(111)A surface..100

48. Top view of the As-trimer model for GaAs(111)B-2x2..102

49. Energy-level diagram at the surface for n-type GaAs(111)B-2x2..............................103

50. HREELS spectra at different beam energies for GaAs(111)B-2x2............................104

51. HREELS spectrum of GaAs(111)B before and after hydrogen exposure..................105

52. HREELS spectrum of GaAs(111)B with hydrogen coverage of 1000 L....................108

ABSTRACT

The microscopic structures and properties of semiconductor surfaces and interfaces are successfully investigated by several different techniques in this thesis.

First, the small cone photoelectron holographic imaging technique, in conjunction with the LEED observation, has been applied to study the interfacial structures of Se/Ge(100)-1x2, Ga/Ge(111)-1x1 and Ge/Si(100)-2x1 samples. The results for the Se/Ge(100)-1x2 suggest that two different regions coexist on the surface. One is fully terminated by Se adatoms at bridge sites, and another is half-covered by Se adatoms on the Ge displaced surface. This is the first experiment to determine the atomic structure of Se/Ge(100)-1x2 sample. The results for the Ga/Ge(111)-1x1 unambiguously show that the Ga atoms occupy both T_4 sites and H_3 sites. The results for the Ge/Si(100)-2x1 clearly indicate that the Ge adsorption displaces the surface Si atoms from the terraces and forms the Ge dimers on the surface. This determination is in agreement with the combined results of the studies by LEEM, LEED and STM [41].

Second, the GaAs(111)A and GaAs(111)B surfaces, prepared by the MBE growth technique, have been studied by HREELS, XPS, UPS and LEED. The MBE growth with Si-doping produces a p-type semiconductor for GaAs(111)A and a n-type for GaAs(111)B, and both surfaces have the same 2x2 reconstruction. The HREELS results from the clean GaAs(111)A and GaAs(111)B surfaces show the Fuchs-Kleiwer surface optical phonon energy at 35.5 meV, but different plasmon-excitation features. Following atomic hydrogen exposure, both As-H and Ga-H stretching modes are observed on the GaAs(111)B surface, while only Ga-H stretching mode appears in the HREELS spectra of GaAs(111)A surface, which can be explained by the Ga-vacancy buckling model of GaAs(111)A[48]. The hydrogen disruption is observed on the GaAs(111)B surface, but it does not take place on the GaAs(111)A surface.

CHAPTER 1

INTRODUCTION

The microscopic structures and properties of semiconductor surfaces and interfaces are a major and fundamental field of study in the solid state physics. For the determination of surface structures, the photoelectron holographic imaging technique has drawn a lot of attention in the past few years. Unlike conventional diffraction measurements, where a proposed structure model is iteratively improved to obtain a best fit to the experimental data using a variety of adjustable parameters, the holographic approach permits direct calculation from the raw data without approximation or adjustable parameters and thus provides unambiguous, unique three-dimensional images of the surface and interface atomic structures. The first part of this thesis reports an investigation of the interface structures by the photoelectron holographic imaging technique. The second part will present high-resolution electron energy-loss spectroscopy (HREELS), ultra-violet photoelectron spectroscopy (UPS), x-ray photoelectron spectroscopy (XPS) and low-energy electron diffraction (LEED) studies of GaAs(111)A and GaAs(111)B surfaces grown by the Molecular Beam Epitaxy (MBE).

Motivation of the Present Work and Structure of the Thesis

The atomic structure of an adatom layer formed on the Ge and Si surfaces is of great interest in both surface research and practice because Si and Ge are heavily used semiconductors, and much effort has been used to determine these structures by various kinds of techniques. The purpose of the first part of the present work is to apply the small-cone photoelectron holography technique to determine some adsorbate structures on Si and Ge surfaces, since this method can effectively reveal the three-dimensional images of surface and interface structures without any assumption of structure model.

Over recent years there has been a great increase in interest in the studies of polar surfaces of GaAs(111) due to their technological applications, such as the development of novel electro-optical devices and low-threshold-current lasers [16, 17]. Thus, it is necessary to grow device-quality surfaces of GaAs(111) by MBE and also understanding of their electronic properties. However, most work on the GaAs(111)A and GaAs(111)B surfaces is performed on the sputtered/annealed surfaces. The facility in the CRISS (Center for Research in Surface Science) lab, Physics Department, Montana State University-Bozeman enables us to grow GaAs(111)A and GaAs(111)B surfaces with MBE , transfer the samples into the analysis chamber without exposure to air, and perform the HREELS, XPS, UPS and LEED studies. It would be very profitable to carry out the study on the MBE-grown surfaces and compare the results obtained from the surfaces produced by these two different techniques.

The thesis is organized as follows. Chapter 2 describes the photoemission phenomenon, the principle of photoelectron diffraction and holography, and the small-cone transform. Chapter 3 describes the experimental equipment, setup and procedures, sample preparation, and the data acquisition and analysis of photoelectron holography. Chapter 4 introduces the instrumentation and experimental procedures for the studies of MBE-grown GaAs(111) surfaces. In Chapter 5, we focus on the photoelectron holographic results and discussion for Se/Ge(100)-1x2, Ga/Ge(111)-1x1, and Ge/Si(100)-2x1 samples. Chapter 6 presents the studies of MBE-grown GaAs(111)A and GaAs(111)B surfaces with HREELS, XPS, UPS and LEED techniques. Chapter 7 summarizes the thesis.

Photoelectron Diffraction and Holography

Photoelectron diffraction occurs when a photoemitted electron finds more than one path into a photoelectron detector. One path is provided by direct propagation from the emitting atom (emitter) to the detector (reference wave), while additional paths are available when the photoelectron scatters elastically from nearby atoms (scatterers). Liebsch [1] suggested that photoelectron diffraction could be observed from adsorbates on a surface and that the interference pattern would contain information about the geometry of atoms surrounding the photoemitting adsorbates on surfaces. In 1986, Szoke [2] pointed out that the two-dimensional photoelectron diffraction pattern is a hologram which can be reconstructed to create an image of the three-dimensional crystal structure of a solid surface. The first

experimental work based on this single-energy photoelectron holography technique was performed by Harp *et al* [3] on Cu(100), and it confirmed this phenomenon. Since then, many measurements and calculations [4-6] have been made to determine surface structures. However, all the results showed twin images (spurious maximum intensity at the position inverted about the emitter from the real atom position), as well as poor accuracy in determining the atom position and large artifacts.

In 1992, Tong, *et al* [7] introduced the technique of energy-dependent photoelectron holography, in which the energy-dependent diffraction curves are obtained by measuring the photoelectron energy distribution curve (EDC) over a range of photon energies for a set of emission angles. Then the spectra are inverted with respect to the wave number and summed in real space to obtain the image function. This approach would eliminate the twin image, reduce background noise, as well as give more accurate measurements of atom positions. The first experiment with using this new technique was made by Wu *et al* on the Si(111) $\sqrt{3}\,\mathrm{x}\,\sqrt{3}$-Al surface with impressive results in 1993 [8]. In 1994, Wu *et al* proposed the small-cone method to significantly reduce the artifacts and improve the quality of the image[9]. Since then, quite a few experimental results[10-12] have proved this new imaging technique to be very effective in determining the surface and interface structures.

Study of MBE-grown GaAs(111) Surfaces

The III-V compound semiconductors have ordinarily been grown on (100) oriented substrates, because high quality epitaxial layers can be grown under a wide range of growth conditions by MBE. However, over recent years there has been a great increase in interest in the growth on GaAs(111) substrates [13-15]. There are two kinds of GaAs(111) surfaces: GaAs(111)A and GaAs(111)B. If the surface is Ga-terminated, it is called GaAs(111)A. If the surface is As-terminated, it is called GaAs(111)B. The special properties of the (111) surface suggest the possibility of fabricating novel electro-optical devices with strong piezoelectrically generated internal electric fields, and low-threshold-current lasers [16, 17]. High quality expitaxial films on GaAs(111) substrates and the understanding of their surface structure and electronic characteristics are crucial for turning this possibility into reality.

The HREELS technique is a very surface sensitive tool for studying the electronic structures of compound semiconductor surfaces, in particular vibrations of adsorbed gases, such as hydrogen. In addition, XPS (excitation photon energy $h\nu$=151.4eV) spectra provide surface stoichiometry information, the UPS spectra show the valence-band features, while LEED exhibits the surface reconstruction patterns. Thus, HREELS, in conjunction with XPS, UPS and LEED, is very a fascinating technique to study semiconductor surfaces as well as their interaction with hydrogen.

CHAPTER 2

PRINCIPLES OF PHOTOELECTRON HOLOGRAPHY

Angular Resolved Photoemission

The most powerful experimental tools for probing the electronic structure of solids are to be found in the area of photoelectron spectroscopy. An incoming photon with sufficient energy $h\nu$ is incident upon the surface of a solid and generates the photoelectrons emitted from the sample as shown in Fig. 1.

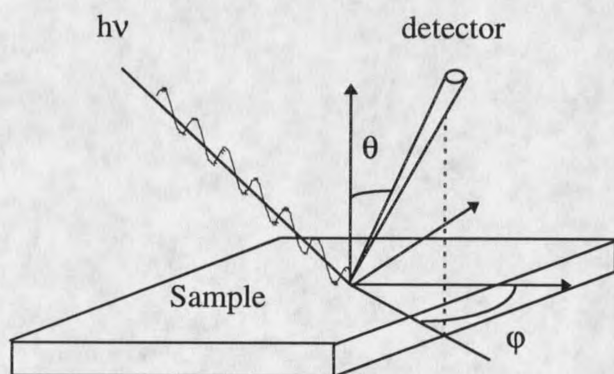

Fig. 1. The photoemission phenomenon. The direction of photoelectrons is defined by the polar angle θ and azimuthal angle φ.

Photoemission spectra are interpreted for most practical purposes within the single-particle approximation. That is, the energy of the photoexcited electron can be written as $E_K = h\nu - E_b - \Phi_w$ where E_b is the binding energy of core-level and Φ_w is the work function of the sample(see Fig. 2).

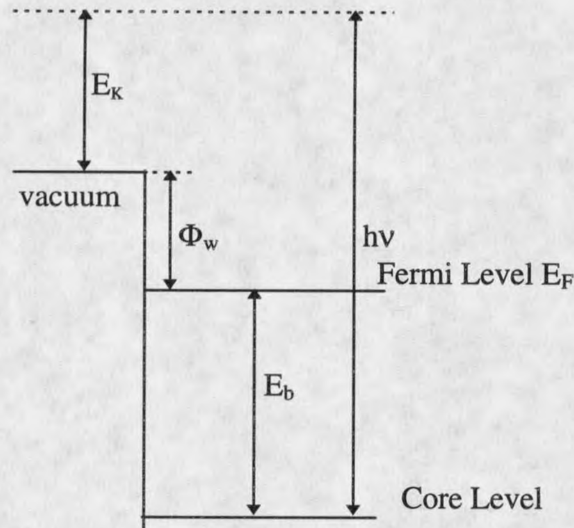

Fig. 2. Energy-level diagram for photoemission process.

In angle-resolved photoemission, if one has measured the kinetic energy of a photoelectron, and also its direction of propagation, one has automatically measured its momentum or wave vector **K** since $E = \hbar^2 K^2 / 2m$. This follows from the energy conservation and the conservation of wave vector parallel to the surface.

$$\mathbf{K}_{//} = \mathbf{k}_{//} \tag{2.1}$$

where $K_{//}$ is the parallel component of the external electron wave vector, and $k_{//}$ is the parallel component of the electron wave vector inside the sample. The conservation of wave vector in the normal direction breaks down due to the potential barrier at the surface. From the energy conversation,

$$E(k) = E(K) + V_{in} \tag{2.2}$$

where V_{in} is called the inner potential or the surface potential barrier [18], $E(K) = \hbar^2 K^2 / 2m$ is the kinetic energy of a photoelectron outside the sample, and $E(k) = \hbar^2 k^2 / 2m$ is the kinetic energy inside the sample. From (2.1) and (2.2), we can get

$$\mathbf{k}_{\perp}^2 = \mathbf{K}_{\perp}^2 + 2m_e V_{in} / \hbar^2 \tag{2.3}$$

where m_e is the electron mass. The intensity of the photoemitted electron flux depends upon not only the magnitude of the electron momentum (photoexcitaion cross section), but also the emission direction (photoexcitation angular dependence). Both effects could be described by one function, the photoexcitation factor $F_k(\hat{\mathbf{k}})$, where $\hat{\mathbf{k}}$ is a unit vector in the direction of electron momentum and k is the magnitude of the electron momentum.

Photoexcitation Factor

A polarized photon field can be described as

$$\mathbf{A}(\mathbf{r}, t) = \hat{\varepsilon} A_0 \exp[i(\mathbf{q} \cdot \mathbf{r} - \omega t)] \tag{2.4}$$

where $\mathbf{A}(\mathbf{r}, t)$ is the vector potential of the electromagnetic field, $\hat{\varepsilon}$ is the unit vector in the polarization direction, A_0 is the amplitude of the vector potential, ω is the photon angular frequency, $\mathbf{q}$ ($q = \omega/c = 2\pi/\lambda$) is the photon wave vector and $\mathbf{r}$ is the position vector measured from the center of an atom. The photon energy in our experiments is usually is below 250 eV. That is, the wave length λ is greater than 50 Å. It means $\mathbf{q}\cdot\mathbf{r} \approx a_0/\lambda << 1$, where a_0 is the Bohr radius. Thus, Eq (2.4) can be reduced to

$$\mathbf{A}(\mathbf{r}, t) = \hat{\varepsilon} A_0 \exp[-i\omega t] \tag{2.5}$$

In our experiment, $\hat{\varepsilon}$ is chosen along the z direction.

The one-particle Hamiltonian operator that describes the atom's interaction with the electromagnetic field in first-order perturbation approximation is given by [19]

$$\hat{H}_1 = -\frac{e}{2m_e c}(\hat{P}\cdot\mathbf{A} + \mathbf{A}\cdot\hat{P}) \tag{2.6}$$

where $\hat{P} = \frac{\hbar}{i}\nabla$ is the momentum operator. Then, the transition matrix element can be presented as

$$M_{i,f} = \langle f|\hat{H}_1|i\rangle = -\frac{e}{2m_e c}\int \Psi_f^*(\hat{P}\cdot\mathbf{A} + \mathbf{A}\cdot\hat{P})\Psi_i d\mathbf{r} \tag{2.7}$$

where $|f\rangle$ and $|i\rangle$ are respectively the final and initial states obtained from the unperturbed Hamiltonian $\hat{H}_0 = \frac{\hat{P}^2}{2m_e} + eV(r)$, while $\Psi_f = \langle r|f\rangle$ is the final state eigenfunction and Ψ_i =

$\langle r|i\rangle$ is the initial state eigenfunction. With the gauge transformation, we can always choose $\nabla \cdot \mathbf{A} = 0$. Thus, in the above integrand, $\hat{P}\cdot \mathbf{A}\Psi_i = \frac{\hbar}{i}\nabla \cdot (\mathbf{A}\Psi_i) = \frac{\hbar}{i}[(\nabla \cdot \mathbf{A})\Psi_i + \mathbf{A}\cdot \nabla\Psi_i]$.

The first term vanishes, and we have $\hat{H}_1 = -\frac{e}{m_e c}\mathbf{A}\cdot\hat{P}$. By the commutation rule $\hat{P} = \frac{im_e}{\hbar}[\hat{H}_0, \mathbf{r}]$, the transition matrix element can be further written as

$$M_{i,f} = -\frac{ie}{\hbar m_e c}e^{-i\omega t}\langle f|\hat{\varepsilon} A_0 \cdot (\hat{H}_0 \mathbf{r} - \mathbf{r}\hat{H}_0|i\rangle = \frac{e}{i\hbar m_e c}(E_f - E_i)e^{-i\omega t}A_0\langle f|\hat{\varepsilon}\cdot \mathbf{r}|i\rangle \quad (2.8)$$

where E_f is the energy of final state, E_i is the energy of initial state and $E_i - E_f = \hbar\,\omega$.

Assuming the angle between $\hat{\varepsilon}$ and $\mathbf{r}$ is θ, then Eq (2.8) is simplified as

$$M_{i,f} = \frac{ie\omega}{m_e c}e^{-i\omega t}A_0\langle f|r\cos(\theta)|i\rangle \quad (2.9)$$

Consider a spinless particle subjected to a spherically symmetric potential. The wave equation is known to be separable in spherical coordinates and the eigenfunctions can be written as [20] $\langle \mathbf{r}|nlm\rangle = R_{nl}(r)Y_l^m(\theta,\phi)$, where the position vector $\mathbf{r}$ is specified by the spherical coordinates r, θ and ϕ, and n stands for the principle quantum number, while l and m are the angular momentum quantum numbers. $M_{i,f}$ can be written as

$$M_{i,f} = \frac{ie\omega}{m_e c}A_0 e^{-i\omega t}\int Y_{lm}^*(\theta,\phi)\cos(\theta)\,Y_{l_0 m_0}(\theta,\phi)d\Omega\int R_{nl}(r)R_{n_0 l_0}(r)r^3 dr \quad (2.10)$$

where $d\Omega = \sin(\theta)d\theta d\phi$. By the orthogonality of the spherical harmonics, we will have a non-vanishing transition only if

$$l = l_0 \pm 1, \quad m = m_0 \quad (2.11)$$

This is called the dipole transition selection rule. Then the photoexcitation factor is defined as [21]

$$F_k(\hat{\mathbf{k}}) = \frac{2m_e}{\hbar^2}\sum_{lm} Y_{lm}(\hat{\mathbf{k}})M_{i,f} \tag{2.12}$$

where $\hat{\mathbf{k}}$ stands for (θ,ϕ). In the simplest case: the initial state is an s state, that is, $m_0=0$, $l_0=0$, then from Eq (2.12) we can get $F_k(\hat{\mathbf{k}}) \propto \cos(\theta)$. It means that the photoexcitation is highest in the polarization direction for the s-state excitation.

If only the photoexcitation effect is considered, then the photoelectron wave function is given by [21]

$$\Psi(\mathbf{k}) = \frac{2m_e}{\hbar^2}\sum_{lm} R_{nl}(r)Y_{lm}(\hat{\mathbf{r}})M_{i,f} \tag{2.13a}$$

$$= \frac{e^{ikr}}{r}F_k(\hat{\mathbf{k}}) \qquad r \to \infty \tag{2.13b}$$

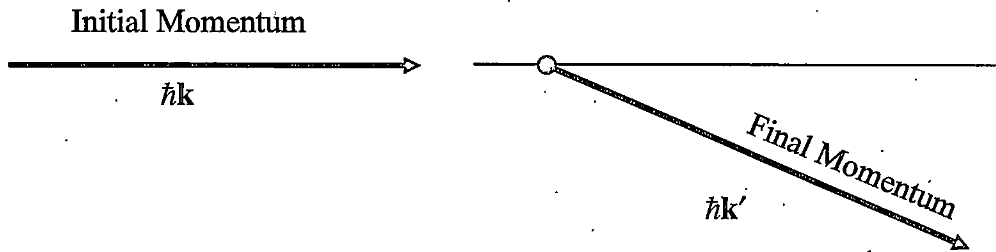

Fig. 3. Initial and final momentum states in scattering.

Atomic Scattering Factor

A photoelectron generally undergoes a number of scatterings before leaving a solid. In quantum mechanics [20], this effect can be described by an atomic scattering factor $f(\mathbf{k}', \mathbf{k})$, where $\mathbf{k}$ the initial wave vector and $\mathbf{k}'$ is the final wave vector after scattering (see Fig. 3).

For the time-independent scattering process, we assume that the Hamiltonian is written as $\mathbf{H} = \mathbf{H}_0 + \mathbf{V}(\mathbf{r})$, where $\mathbf{H}_0$ stands for the kinetic-energy operator. Then in the first-order perturbation approximation, $f(\mathbf{k}', \mathbf{k})$ for the outgoing wave is represented as

$$f(\mathbf{k}', \mathbf{k}) = -\frac{4\pi^2 m_e}{\hbar^2}\left\langle \mathbf{k}' \middle| V(\mathbf{r}) \middle| \psi^+ \right\rangle \tag{2.14a}$$

$$= -\frac{4\pi^2 m_e}{\hbar^2}\int d\mathbf{r}' \frac{e^{-i\mathbf{k}'\cdot\mathbf{r}'}}{(2\pi)^{3/2}} V(\mathbf{r}')\left\langle \mathbf{r}' | \psi^+ \right\rangle \tag{2.14b}$$

at large distances. $\left\langle \mathbf{r}' \middle| \Psi^+ \right\rangle$ denotes the outgoing scattered wave function. In terms of partial-wave expansion, $f(\mathbf{k}', \mathbf{k})$ can be written as [20]

$$f(\mathbf{k}', \mathbf{k}) = f_k(\theta) = \frac{1}{k}\sum_{l=0}(2l+1)e^{i\delta_l}\sin\delta_l P_l(\cos\theta) \tag{2.15}$$

where θ is the scattering angle, δ_l is the phase of the outgoing wave and is a function of k, and $P_l(\cos\theta)$ is described as

$$P_l(\cos\theta) = \frac{(-1)^l}{2^l l!}\frac{d^l(1-\cos^2\theta)^l}{d(\cos\theta)^l} \tag{2.16}$$

If only the scattering effect is considered, then the scattered outgoing spherical wave at larger distances can be written as

$$\Psi(r) = \frac{e^{ikr}}{r} f(\mathbf{k}', \mathbf{k}) \tag{2.17}$$

Photoelectron Diffraction

A photon with energy hν is incident on the surface and ejects a photoelectron from an atom (emitter). Part of the photoelectron wave, called reference wave Ψ_D, will directly propagate into the detector, while the rest of photoelectron wave will be scattered by the neighboring atoms and then go to the detector, called object wave Ψ_S. The reference wave will interfere with the object waves and form a two-dimensional diffraction pattern. This phenomenon is called photoelectron diffraction and is illustrated in Fig. 4.

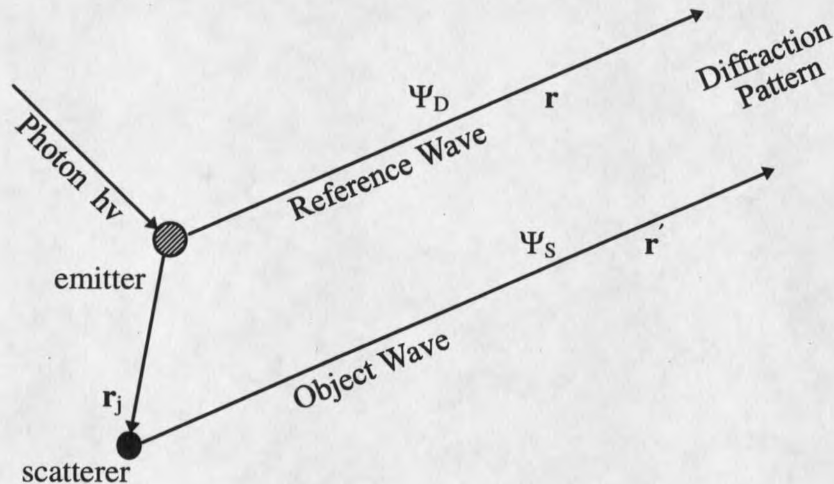

Fig. 4. The phenomenon of photoelectron diffraction.

Only the waves from the same emitter are coherent and can interfere with each other. The waves from different emitters are incoherent. Thus they do not interfere with each other, and their intensities are just added together. Next, it will be shown that the three dimensional images of the surface structures can be reconstructed from the diffraction patterns.

If we place the origin of the coordinate system at atom α, which is the emitter, the photoelectron final wave function at the observation point is given by

$$\psi(\mathbf{k}) = \psi_D(\mathbf{k}) + \psi_S(\mathbf{k}) \tag{2.18}$$

where $\psi_D(\mathbf{k})$ is the reference wave function, $\psi_S(\mathbf{k})$ is the object wave function. From Eq. (2.13), $\Psi_D(\mathbf{k}) = \frac{e^{ikr}}{r} F_k(\hat{\mathbf{k}})$ at large distances. The object wave function is given as

$$\Psi_S(\mathbf{r}') = \Psi_D(\mathbf{r}_j) \frac{e^{ikr'}}{r'} f_k(\hat{\mathbf{k}} \cdot \hat{\mathbf{r}}_j) \tag{2.19}$$

$$\Psi_D(\mathbf{r}_j) = \frac{e^{ikr_j}}{r_j} F_k(\hat{\mathbf{r}}_j) \tag{2.20}$$

From Fig. 4, we can see

$$\mathbf{r}' = \mathbf{r} - \mathbf{r}_j \tag{2.21}$$

Since r and r' are very large compared to r_j, Eq (2.21) can be written as

$$r' = r(1 - \hat{\mathbf{k}} \cdot \hat{\mathbf{r}}_j) \tag{2.22}$$

Thus, Eq (2.19) becomes

$$\Psi_S(\mathbf{r}') = \frac{e^{ikr_j}}{r_j} F_k(\hat{\mathbf{r}}_j) \frac{e^{ikr - i\mathbf{k}\cdot\mathbf{r}_j}}{r} f_k(\hat{\mathbf{k}} \cdot \hat{\mathbf{r}}_j) \tag{2.23a}$$

$$= \Psi_D(\mathbf{k}) A(\mathbf{k}, \mathbf{r}_j) e^{i(kr_j - \mathbf{k}\cdot\mathbf{r}_j)} \tag{2.23b}$$

where

$$A(\mathbf{k}, \mathbf{r}_j) = \frac{F_k(\hat{\mathbf{r}}_j)}{F_k(\hat{\mathbf{k}})} \frac{f_k(\hat{\mathbf{k}} \cdot \hat{\mathbf{r}}_j)}{r_j} \tag{2.24}$$

$A(\mathbf{k},\mathbf{r}_j)$ is called the effective scattering factor.

There are more than one atom around the emitter and thus the object wave function is the summation of the scattered waves from each scatterer.

$$\Psi_S(\mathbf{k}) = \Psi_D(\mathbf{k})\sum_j A(\mathbf{k}, \mathbf{r}_j)e^{i(kr_j - \mathbf{k}\cdot\mathbf{r}_j)} \tag{2.25}$$

So the final wave function is

$$\Psi(\mathbf{k}) = \Psi_D(\mathbf{k})\left(1 + \sum_j A(\mathbf{k}, \mathbf{r}_j)e^{i(kr_j - \mathbf{k}\cdot\mathbf{r}_j)}\right) \tag{2.26}$$

Then, the photoelectron diffraction intensity $I(\mathbf{k})$ is written as

$$\begin{aligned} I(\mathbf{k}) &= |\Psi(\mathbf{k})|^2 = \left(\Psi_D(\mathbf{k}) + \Psi_S(\mathbf{k})\right)\left(\Psi_D(\mathbf{k}) + \Psi_S(\mathbf{k})\right)^* \\ &= I_0(\mathbf{k})\left(1 + \sum_j A(\mathbf{k}, \mathbf{r}_j)e^{i(kr_j - \mathbf{k}\cdot\mathbf{r}_j)} + \sum_j A^*(\mathbf{k}, \mathbf{r}_j)e^{-i(kr_j - \mathbf{k}\cdot\mathbf{r}_j)}\right. \\ &\quad \left. + \sum_j \sum_n A(\mathbf{k}, \mathbf{r}_j)A^*(\mathbf{k}, \mathbf{r}_n)e^{i(kr_j - \mathbf{k}\cdot\mathbf{r}_j)}e^{-i(kr_n - \mathbf{k}\cdot\mathbf{r}_n)}\right) \end{aligned} \tag{2.27}$$

Where $I_0 = |\Psi_D(\mathbf{k})|^2$. The last term in Eq. (2.27) can be ignored because of $|A| < 1$. I_0 is the reference wave intensity and does not contain any diffraction information. So we define a normalized hologram function $\chi(\mathbf{k})$ by removing the reference wave as much as possible.

$$\chi(\mathbf{k}) \equiv I(\mathbf{k})/I_0(\mathbf{k}) - 1 \tag{2.28a}$$

$$= \sum_j A(\mathbf{k}, \mathbf{r}_j)e^{i(kr_j - \mathbf{k}\cdot\mathbf{r}_j)} + \sum_j A^*(\mathbf{k}, \mathbf{r}_j)e^{-i(kr_j - \mathbf{k}\cdot\mathbf{r}_j)} \tag{2.28b}$$

This hologram function $\chi(\mathbf{k})$ contains just the oscillating (interference) part of the hologram.

The experimental energy-dependent photoelectron diffraction spectra are obtained by measuring the core-level peak intensities over a range of photon energies and a set of emission

angles. Each energy-dependent curve I(**k**) is a Constant Initial-state Spectrum (CIS) [22]; that is, each spectrum is recorded by varying the photon energy hν while keeping the initial state energy E_i constant. $I_0(\mathbf{k})$ is taken as the smooth, slowly varying part of I(**k**). Then we can get the normalized diffraction function χ(**k**). However, χ(**k**) represents the diffraction pattern in **k** space, we need to perform a Fourier transform to create a image in the real space.

Holographic Inversion

The spatially resolved imaging by energy-dependent photoelectron diffraction takes two steps[5]. First, all normalized diffraction spectra are individually Fourier transformed to three-dimensional vector space. Then the complex transformed amplitudes are summed over all emission directions $\hat{\mathbf{k}}$. In the Fourier transformation of Tong *et al.* [7], each χ(**k**) (**k** can be written as $k\hat{\mathbf{k}}$) is transformed in terms of the vector **R**

$$\Phi_{\hat{k}}(\mathbf{R}) = \int_{k_{min}}^{k_{max}} dk\, \chi(k\hat{\mathbf{k}}) e^{-ik(R-\hat{k}\cdot\mathbf{R})} g(k) \qquad (2.29)$$

where g(k) is a smooth window function to reduce the artificial oscillations near the end points k_{max} and k_{min} of $\chi(k\hat{\mathbf{k}})$, since the selection of $I_0(\mathbf{k})$ might produce these artificial oscillations around the end points in $\chi(k\hat{\mathbf{k}})$.

The function g(k) is chosen as a Hanning function [23].

$$g(k)=\begin{cases}\sin^2\dfrac{\pi(k-k_{min})}{2(k_1-k_{min})} & k_{min}<k<k_1\\ 1 & k_1<k<k_2\\ \cos^2\dfrac{\pi(k-k_2)}{2(k_{max}-k_2)} & k_2<k<k_{max}\end{cases} \tag{2.30}$$

where $k_1 = k_{min} + b\dfrac{k_{max}-k_{min}}{2}$. $0 \le b \le 1$.

$$k_2 = k_{max} - b\frac{k_{max}-k_{min}}{2}. \quad 0 \le b \le 1.$$

Substituting Eq. (2.28b) into Eq. (2.29), one obtains:

$$\Phi_{\hat{k}}(\mathbf{R}) = \sum_j \int_{k_{min}}^{k_{max}} A(\mathbf{k},\mathbf{r}_j) e^{-ik[R(1-\hat{k}\cdot\hat{R})-r_j(1-\hat{k}\cdot\hat{r}_j)]} g(k)dk +$$

$$\sum_j \int_{k_{min}}^{k_{max}} A^*(\mathbf{k},\mathbf{r}_j) e^{-ik[R(1-\hat{k}\cdot\hat{R})+r_j(1-\hat{k}\cdot\hat{r}_j)]} g(k)dk \tag{2.31}$$

The function $\left|\Phi_{\hat{k}}(\mathbf{R})\right|$ is a maximum along the locus $C_{\hat{k},1}$

$$R(1-\hat{\mathbf{k}}\cdot\hat{\mathbf{R}}) = r_1(1-\hat{\mathbf{k}}\cdot\hat{\mathbf{r}}_1) \tag{2.32}$$

Since $\mathbf{r}_1$ and $\mathbf{k}$ are fixed, $r_1(1-\hat{\mathbf{k}}\cdot\hat{\mathbf{r}}_1)$ is a constant. Then

$$R = \frac{\text{constant}}{1-\cos(\hat{\mathbf{k}}\cdot\hat{\mathbf{R}})} \tag{2.33}$$

This is the equation of a paraboloid of solution with $\hat{\mathbf{k}}$ as its principle-axis direction, and the function $\Phi_{\hat{k}}(\mathbf{R})$ has a maximum amplitude on this paraboloid. One can see that if $\mathbf{R} = \mathbf{r}_1$, $\left|\Phi_{\hat{k}}(\mathbf{R})\right|$ always has a maximum no matter what $\hat{\mathbf{k}}$ is. This means that all parabolic loci

intersect at the atom position $\mathbf{r}_1$ and form a bright spot. If there are other atoms $\mathbf{r}_2, \mathbf{r}_3, \ldots$ in the solid with the same single-scattering path difference, i.e., if

$$r_j(1-\hat{\mathbf{k}}\cdot\hat{\mathbf{r}}_j) = r_1(1-\hat{\mathbf{k}}\cdot\hat{\mathbf{r}}_1) \tag{2.34}$$

then the positions of these other atoms must fall on the same paraboloid. The situation is depicted schematically in Fig. 5, where $\mathbf{r}_1$ and $\mathbf{r}_2$ have the same path difference with respect to a transformed photoelectron diffraction spectrum in direction $\hat{\mathbf{k}}$. However, if we consider another transformed photoelectron diffraction spectrum in a different direction $\hat{\mathbf{k}}'$, then the new parabolic loci, $C_{\hat{k}',1}$ and $C_{\hat{k}',2}$, are spatially resolved. Mathematically, this reflects the fact that if

$$r_1(1-\hat{\mathbf{k}}\cdot\hat{\mathbf{r}}_1) = r_2(1-\hat{\mathbf{k}}\cdot\hat{\mathbf{r}}_2) \tag{2.35a}$$

then

$$r_1(1-\hat{\mathbf{k}}'\cdot\hat{\mathbf{r}}_1) \neq r_2(1-\hat{\mathbf{k}}'\cdot\hat{\mathbf{r}}_2) \tag{2.35b}$$

for any two atoms $\mathbf{r}_1 \neq \mathbf{r}_2$ and two directions $\hat{\mathbf{k}} \neq \hat{\mathbf{k}}'$. By using all transformed diffraction spectra along different emission directions, the parabolic loci intersect to form bright spots. These spots provide spatially resolved information of atomic positions in these planes of view.

Mathematically, we obtain the spatially resolved images by summing the complex Fourier functions over a span of emission directions

$$U(\mathbf{R}) = \left|\sum_{\text{all } \hat{k}} \Phi_{\hat{k}}(\mathbf{R})\right|^2 \tag{2.36}$$

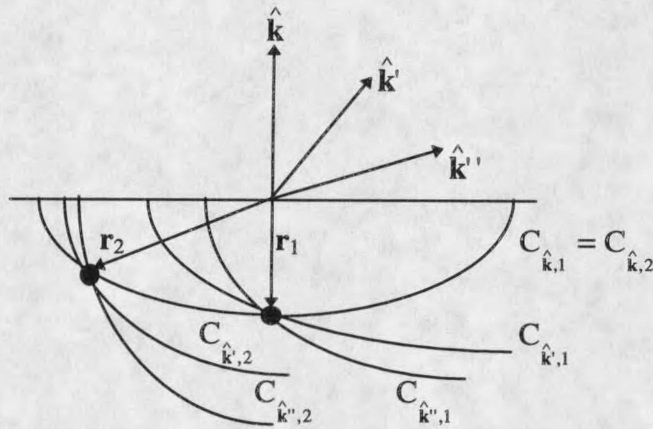

Fig. 5. Intensity loci due to scattering path differences for atoms $\mathbf{r}_1$, $\mathbf{r}_2$ and emission directions $\hat{\mathbf{k}}$, $\hat{\mathbf{k}}'$ and $\hat{\mathbf{k}}''$. The intersections of the contours produce images.

Small-Cone Summation

In Eq. (2.36), all the CIS inversion curves are summed to obtain an image intensity function (this method is called the full window summation). However, in 1994, Wu *et al* [9, 10] introduced the small-cone method based on the experimentally determined phase and magnitude of the field generated by inversion of spectra, which effectively reduces artifacts (artifacts refer to some bright spots in the images caused by inappropriate algorithm of data analysis rather than real atoms).

From the discussion in last section, we know that $\Phi_{\hat{k}}(\mathbf{R})$ has the maximum magnitude for each direction $\hat{\mathbf{k}}$ when $\mathbf{R} = \mathbf{r}_j$, which is noted as $\Phi_{\hat{k}}^{max}(\mathbf{r}_j)$. The image function U(**R**) in Eq. (2.36) would have a large intensity at the jth atom's position $\mathbf{r}_j$ if all the $\Phi_{\hat{k}}^{max}(\mathbf{r}_j)$ were in phase. However, the experimental results (see Fig. 7, Fig. 20, and Fig. 34) show that $\Phi_{\hat{k}}^{max}(\mathbf{r}_j)$ has a relatively constant phase with a larger amplitude only in a small-emission direction range, not over all the emission directions. Outside that region, $\Phi_{\hat{k}}^{max}(\mathbf{r}_j)$ has a relatively rapid changing phase with a smaller amplitude. Therefore, unlike Eq. (2.36), the small-cone method only adds the in-phase $\Phi_{\hat{k}}^{max}(\mathbf{r}_j)$ together to construct an image function and reduces the artifacts.

$$U(\mathbf{R}) = \left| \sum_{\hat{k} \in \mathrm{Cone}(-\hat{\mathbf{R}}, w)} \Phi_{\hat{k}}(\mathbf{R}) \right|^2 \qquad (2.37)$$

For each point **R**, the sum of the CIS inversion spectra is just over a small range of $\hat{\mathbf{k}}$ directions which are within a small cone of angular width w centered on $-\hat{\mathbf{R}}$ (see Fig. 6). The half width w can be obtained from the experimental data by plotting the phases and amplitudes of $\Phi_{\hat{k}}^{max}(\mathbf{r}_j)$ vs. emission angle, which can be obtained by transforming different CIS's to the point $\mathbf{R} = \mathbf{r}_j$ using Eq. (2.29). Figure 7 shows the phase and amplitude the CIS inversion at the position Ga atom A as a function of polar angle for Ga/Ge(111)-1x1 (see Fig. 30(a) and Fig. 30(b), one of the results will be presented in Chapter 5). The azimuthal angles are 0^0 for the positive polar angle and 180^0 for the negative polar angle.

The intensity loci from the different scatterers overlap at some region. When they are in phase, some artifact will be produced. Since the intensity loci used in the summation are within the small cone, the number and intensities of such artifacts are reduced compared to the full window method. Hence the quality of image is further improved by the small cone method.

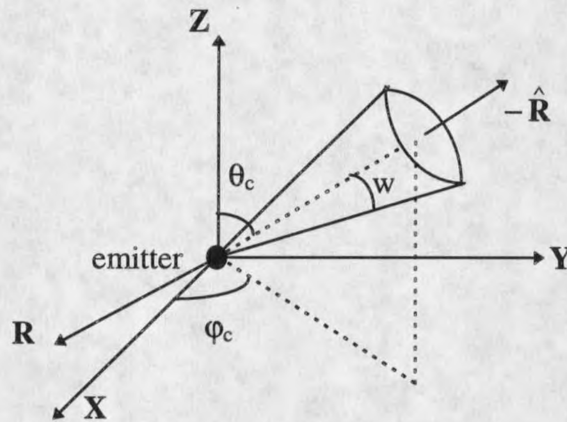

Fig. 6. The chosen small cone with a half width w for a given position **R**.

Effects of Multiple-Scattering

In the above discussion, only single-scattering is considered. However, a photoelectron generally undergoes a number of multiple scatterings before leaving a solid. Thus, their effect must be considered. If we place the origin of the coordinate system at atom α, which is the emitter, the photoelectron scattering wave function for an atom at $\mathbf{r}_\beta$ is given by [7]

$$\Psi_s(\mathbf{r}) = \frac{e^{ikr}}{r}\left[f_k(\hat{\mathbf{k}}\cdot\hat{\mathbf{r}}_\beta)F_k(\hat{\mathbf{r}}_\beta)\frac{e^{ikr_\beta}}{r_\beta} + f_k(\hat{\mathbf{k}}\cdot\hat{\mathbf{r}}_{\beta\gamma})f_k(\hat{\mathbf{r}}_{\beta\gamma}\cdot\hat{\mathbf{r}}_\gamma)F_k(\hat{\mathbf{r}}_\gamma)\frac{e^{ikr_\gamma}}{r_\gamma}\frac{e^{ikr_{\beta\gamma}}}{r_{\beta\gamma}} + \cdots \right] e^{-i\mathbf{k}\cdot\mathbf{r}_\beta} + \cdots$$

$$r \to \infty. \tag{2.38}$$

where $\mathbf{r}_{\beta\gamma} = \mathbf{r}_\beta - \mathbf{r}_\gamma$. The first term in Eq. (2.38) is the single-scattering event at atom $\mathbf{r}_\beta$, the second term includes an intermediate scattering at atom $\mathbf{r}_\gamma$, before scattering at $\mathbf{r}_\beta$ (double-scattering event), and so on. Using Eq. (2.38), we can write down explicitly the different orders of scattering contributions to $\chi(\mathbf{k})$ for paths that scatter from atom $\mathbf{r}_\beta$,

$$\chi(\mathbf{k}) = \left(A(\mathbf{k},\mathbf{r}_\beta)e^{ikr_\beta} + B(\mathbf{k},\mathbf{r}_\beta,\mathbf{r}_\gamma)e^{i(kr_\gamma + kr_{\beta\gamma})} + \cdots \right) e^{-i\mathbf{k}\cdot\mathbf{r}_\beta} + \cdots \tag{2.39}$$

Again, the factor A($\mathbf{k}$, $\mathbf{r}_\beta$) is defined in Eq. (2.24) and

$$B(\mathbf{k},\mathbf{r}_\beta,\mathbf{r}_\gamma) = \frac{f_k(\hat{\mathbf{k}}\cdot\hat{\mathbf{r}}_{\beta\gamma})}{r_{\beta\gamma}} \frac{f(\hat{\mathbf{r}}_{\beta\gamma}\cdot\hat{\mathbf{r}}_\gamma)}{r_\gamma} \frac{F_k(\hat{\mathbf{r}}_\gamma)}{F_k(\hat{\mathbf{k}})} \tag{2.40}$$

Substituting $\chi(\mathbf{k})$ into Eq. (2.29) generates intensity maxima having loci satisfying the relation

$$R - \hat{\mathbf{k}}\cdot\mathbf{R} = \rho_\beta - \hat{\mathbf{k}}\cdot\mathbf{r}_\beta \tag{2.41}$$

where $\rho_\beta = r_\gamma + \left|\mathbf{r}_\beta - \mathbf{r}_\gamma\right|$. The solution of Eq. (2.41), i.e.,

$$R = \frac{\rho_\beta - \hat{\mathbf{k}}\cdot\mathbf{r}_\beta}{1 - \hat{\mathbf{k}}\cdot\hat{\mathbf{R}}} \tag{2.42}$$

is independent of $\hat{\mathbf{k}}$ if and only if

$$\rho_\beta = r_\beta \tag{2.43a}$$

and $\hat{\mathbf{R}} \parallel \hat{\mathbf{r}}_\beta$ (2.43b)

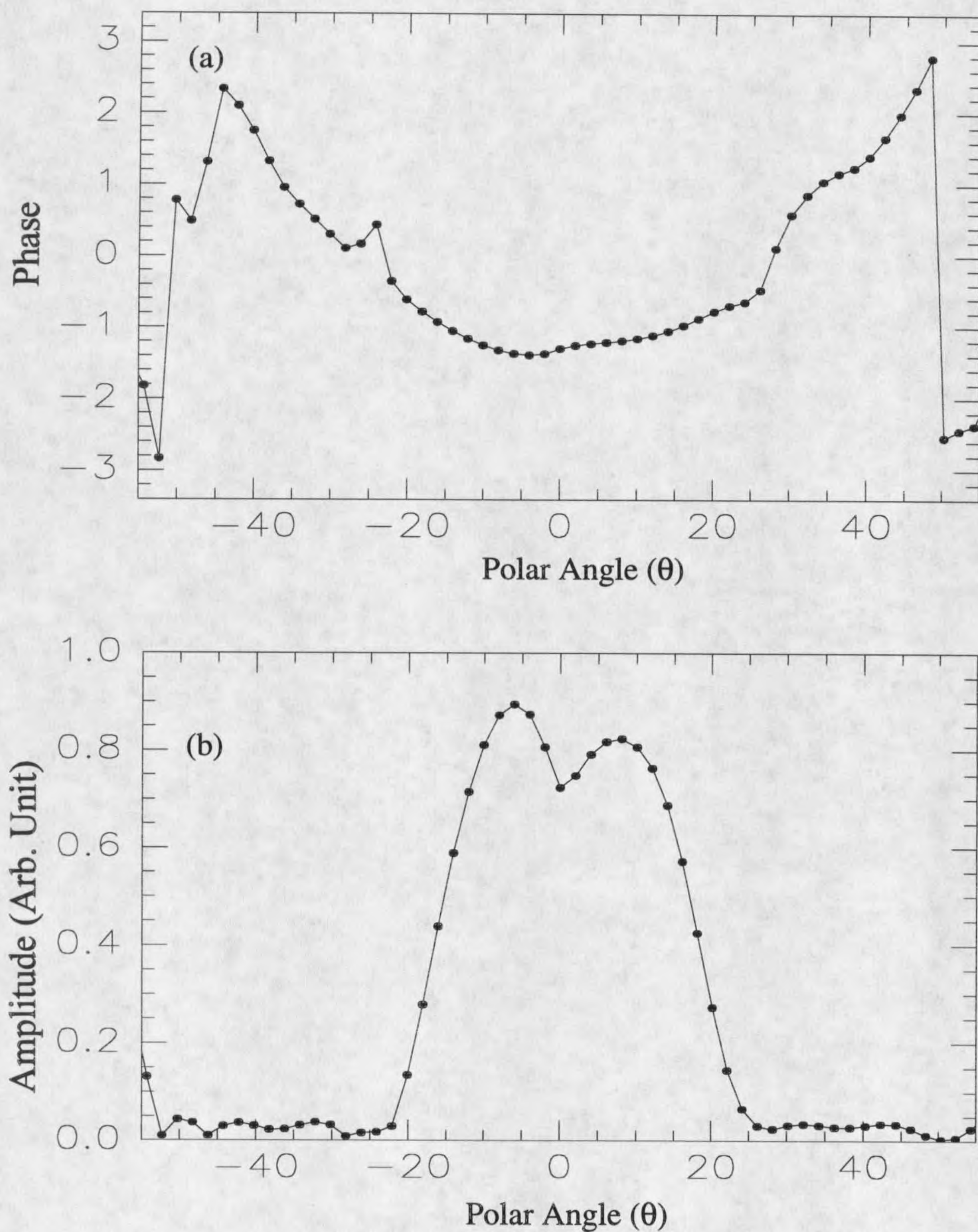

Fig. 7. (a) Phase and (b) amplitude of the CIS inversion vs. polar angle at the position of Ga atom A for Ga/Ge(111)-1x1 sample. $\varphi = 0^0$ if $\theta > 0$ and $\varphi = 180^0$ if $\theta < 0$.

With these two conditions satisfied, the solution of Eq. (2.42) is $R = r_\beta$, and together with Eq. (2.43b) yields $\mathbf{R} = \mathbf{r}_\beta$. In other words, only at $\mathbf{R} = \mathbf{r}_\beta$ would all the intensity loci for all different $\hat{\mathbf{k}}$ directions intersect at a single point. Therefore, while multiple-scattering paths generate a multitude of high-order intensity loci, these loci do not all intersect at a single point. As a result, the intensity in real space due to multiple-scattering paths is very weak compared to the intensity at true atomic positions $\mathbf{R} = \mathbf{r}_\beta$. Figure 8 depicts the single-scattering and multiple-scattering loci for different directions arising from an atom at $\mathbf{r}_1$. Therefore, the multiple-scattering effects are eliminated in this photoelectron holographic process.

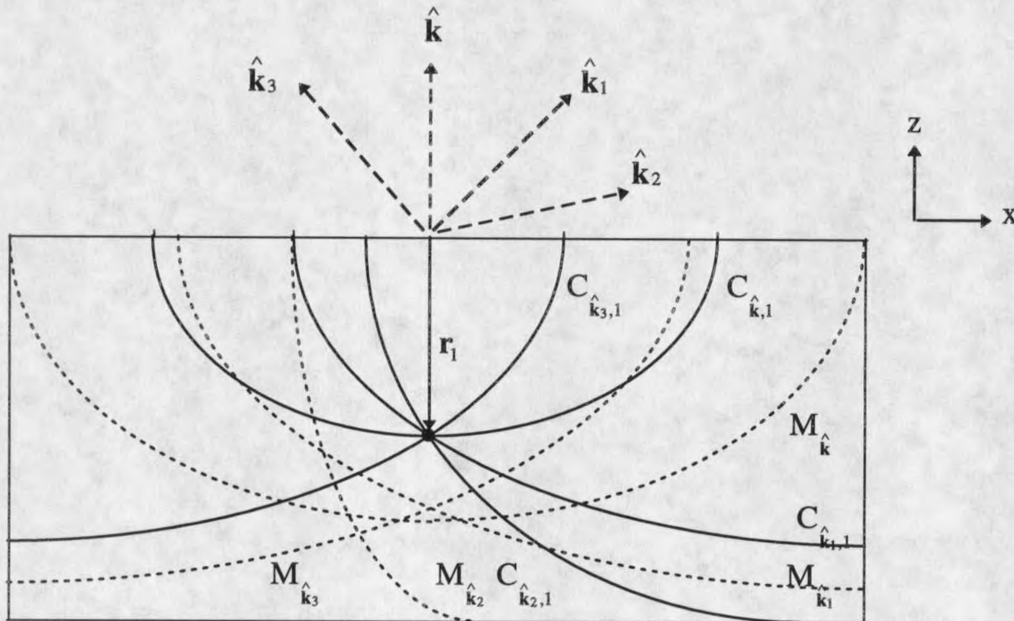

Fig. 8. A schematic drawing of single-scattering contours (solid lines) and multiple scattering contours (dashed lines) corresponding to an atom at $\mathbf{r}_1$ and emission directions $\hat{\mathbf{k}}$, $\hat{\mathbf{k}}_1$, $\hat{\mathbf{k}}_2$ and $\hat{\mathbf{k}}_3$.

CHAPTER 3

EXPERIMENTAL EQUIPMENT AND PROCEDURES OF PHOTOELECTRON HOLOGRAPHY

Synchrotron Radiation Photon Source

All experimental work on photoelectron holography was performed at Iowa/Montana beamline of Synchrotron Radiation Center (SRC), University of Wisconsin-Madison. The synchrotron radiation is generated in a large electron storage ring under ultrahigh vacuum (UHV), as shown in Fig. 9. Electrons are generated from tungsten filaments and are accelerated to about 108 MeV in the microtron. Then the electrons are injected into the storage ring in 15 bunches with a time separation of 19.8 ns and energized to 800 MeV or 1 GeV. The radio frequency (RF) cavity is required to maintain the electron energy. The electrons travel around the ring with a velocity approaching the speed of light. The bending magnets change the electron trajectory and make the electrons radiate highly concentrated electromagnetic wave in the tangential direction of the orbit.

The radiation from an electron storage ring has several unique characteristics which make it extremely attractive as an experimental probe. It is a continuum source in a energy range from the infrared to several keV, where no other such source exists; it is polarized with

the electric field vector in the plane of the electron orbit; it is highly collimated; it is stable in source position and intensity since the stored packet of electrons is carefully controlled.

Since the synchrotron radiation is a continuum photon source, a monochromator is needed to select particular frequencies. In next section, we will discuss a combined ERG (Extended Range Grasshopper) – Seya-Namioka (Seya, for brevity) monochromator system (it is also called the Iowa/Montana beamline).

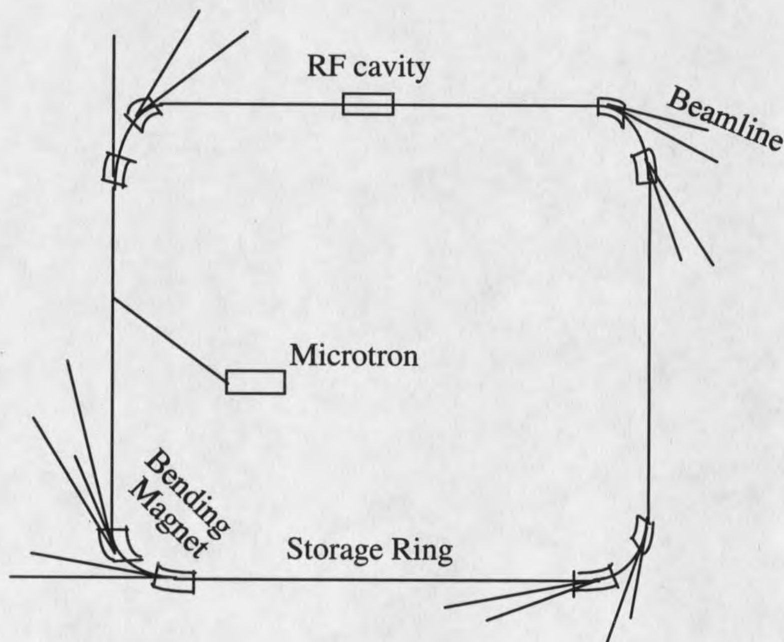

Fig. 9. A schematic diagram of synchrotron radiation storage ring.

A Combined ERG-Seya Beamline

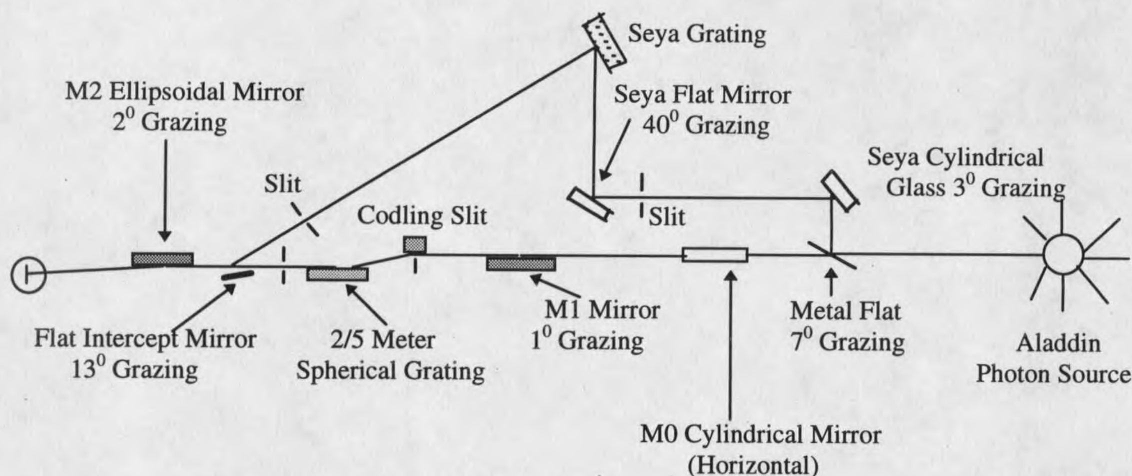

Fig. 10. Schematic layout of ERG-Seya Namioka monochromators.

The monochromators used in the experiments are on the Iowa/Montana beamline; its optical layout is shown in Fig. 10 [24, 25]. This beamline is equipped with two monochromators, the ERG and Seya. It covers the photon energy range from 5 eV to 1 keV. The two monochromators were configured so that they use the same final refocusing mirror. This means that light from either monochromator will be incident on the sample from the same direction and will be focused at the same spot. Each monochromator has several different gratings for covering different energy ranges.

The ERG monochromator has two gratings, the 2 meter and 5 meter gratings (the radius of curvature of the grating). The 2 meter grating provides the photon energy from 40

eV to 240 eV, while the 5 meter grating covers the photon energy from 300 eV to 1200 eV. The Seya monochromator has four different gratings covering energy range from 5 eV to 50 eV. The ERG is mainly used for measuring core-level spectra, while the Seya is useful for valence-band and Fermi-level measurements. The photon flux and resolution depends upon the monochromator type, grating, photon energy and slit width, the details of which can be found elsewhere [24]. Since the entrance and exit slits are adjustable, users can optimize the flux/resolution factor for a given experiment.

Electron Energy Analyzer

The electron energy analyzer used in the experiments is the angle-resolved hemispherical analyzer (HA-50) made by Vacuum Science Workshop, which is attached on a goniometer. The goniometer is mounted on the rotational table so that the polar angle θ between the sample normal and the direction of collection can be varied. The goniometer can swing the HA-50 up and down in the vertical plane for changing the analyzer's vertical acceptance angle ψ.

The half acceptance angle of the HA-50 is about 2^0 and the mean radius of the hemisphere is 50 mm with a resolution $E/\Delta E$ of about 100, which are very good parameters for angle-resolved photoemission measurements. Figure 11 shows a schematic of the hemispherical analyzer. The lens system transfers the electrons emitted from the sample onto the entrance slit by varying the deflection voltages. The electrons from the sample are retarded

or accelerated by the ramping voltage to the pass energy. Those electrons with the detected kinetic energy pass through the hemispherical path, arrive the exit slit, and hit the channeltron. A channeltron is a continuous dynode electron multiplier, where an electron is multiplied through secondary electron emission by a factor of about 10^6 [26].

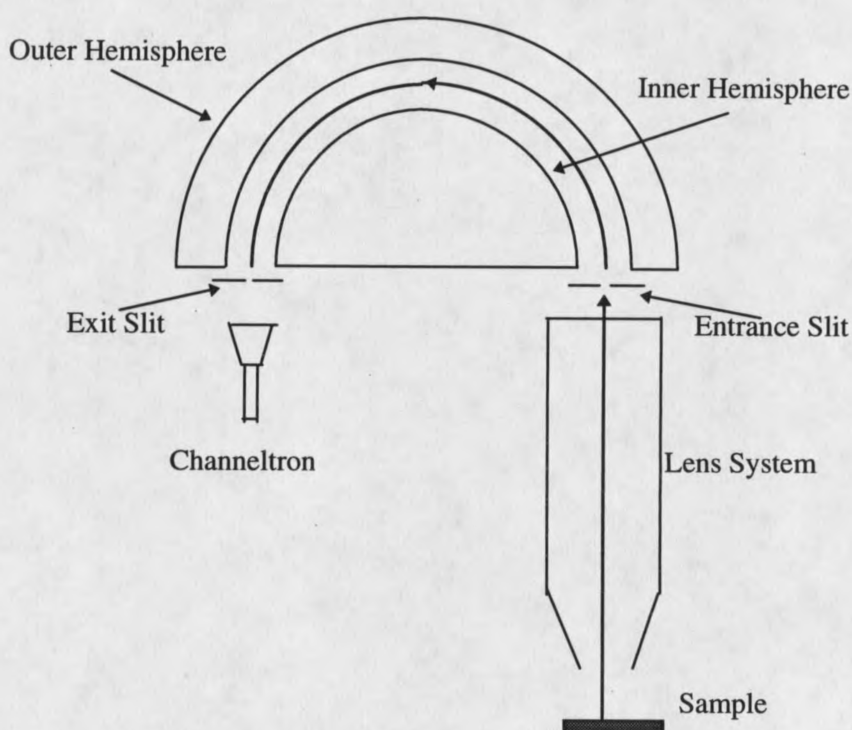

Fig. 11. A schematic layout of the hemispherical analyzer.

Sample Preparation

Clean Si(100) and Ge(100) vicinal surfaces exhibit steps and dimer-reconstructed terraces. The adjacent terraces separated by single steps have dimer directions perpendicular

to each other, which leads to a mixed 2x1+1x2 (i.e. two domains) LEED pattern. Consequently, any experimental results will be ambiguous. It is found that a vicinal (100) surface with the normal direction about 4^0 off the (100) has only double-layer steps with terrace width about 40 Å [27, 28]. Thus, the dimer directions are all the same on the entire surface forming a single-domain 2x1 LEED pattern. In the experiments, both Ge(100) and Si(100) wafers are a 4^0 vicinal cut off the (100) direction to obtain a single domain. All substrates (Ge(100), Ge(111) and Si(100)) are mounted on the sample holder and then the sample and the holder are outgassed by passing electric current through the sample for several hours in the intermediate chamber (see Fig. 12), where the base pressure is about 1×10^{-9} torr.

The base pressure in the analysis chamber is maintained at 9×10^{-11} torr or below, where Ge(100) and Ge(111) surfaces are cleaned by Ar^+ sputtering followed by an anneal up to about 875^0 C [27]. In order to obtain a high-quality clean Ge surfaces, the substrates are held at about 500^0 C when Ar^+ sputtering. After several cycles of sputtering and annealing, the clean Ge(111) surface shows a good c(2x8) LEED pattern, while the clean Ge(100) surface shows a good single domain 2x1 LEED structure. The Si(100) sample is heated to 1150^0 C for about 10 seconds maintaining the vacuum pressure below 1×10^{-9} torr and cooled down quickly to 850^0 C, then gradually cooled down to room temperature. A good single domain 2x1 LEED structure is obtained.

The quartz crystal oscillator (QCO) was used for the thickness monitoring of the deposition on the clean surfaces. The Ge was deposited on the Si(100) substrate held at 500^0 C by evaporation from a tantalum basket. The surface still maintained a single domain 2x1

LEED pattern. The Se flux was obtained by evaporating ZnSe rather than using elemental Se since the latter is toxic. A piece of ZnSe crystal was placed into a tantalum boat and heated to produce the Se flux. Both Se and Zn atoms were deposited on the Ge(100) 2x1 surface when the source was heated up to about 900^0 C. Then the sample was annealed to about 525^0 C to desorb all Zn atoms from the surface and leave the surface covered with only Se atoms. A well order 1x2 LEED pattern was formed. The Ga was evaporated onto the Ge(111) c(2x8) surface from a tantalum boat and LEED showed a 1x1 pattern. During the evaporation, the pressure was kept below $1x10^{-9}$ torr.

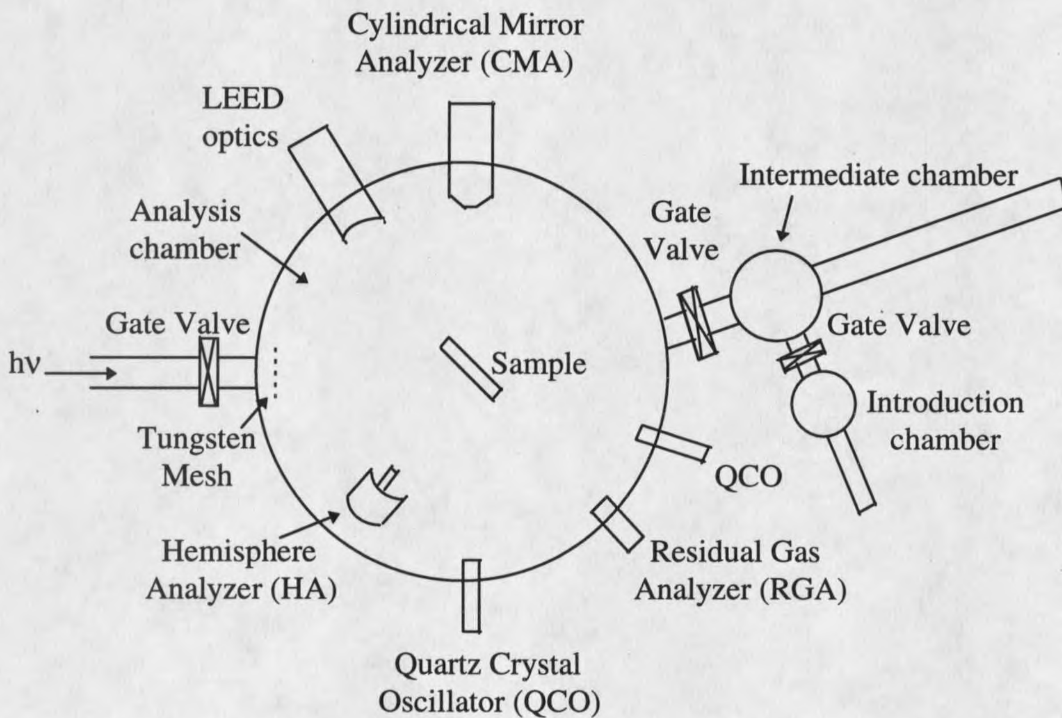

Fig. 12. The layout of vacuum system, which consists of three chambers: introduction chamber, intermediate chamber and analysis chamber.

Data Acquisition and Analysis Procedures

The energy-dependent photoelectron diffraction data are obtained by measuring the CIS spectra over a set of emission angles (θ,φ). The selection of the measuring range is based on the sample symmetry, which should be an irreducible region of the reciprocal lattice. The Ga/Ge(111) sample has three-fold rotational symmetry about the (111) direction and has three mirror planes. Thus, the irreducible region is a 1/6 of the emission hemisphere (shown in Fig. 13(a)). For Se/Ge(100) and Ge/Si(100) samples, which have two-fold rotational symmetry and two mirror planes, the irreducible region is a quadrant of the emission hemisphere (shown in Fig. 13(b)). In order to keep the same solid angle on the emission hemisphere for each measuring direction, $\Delta\theta$ is chosen to be constant and $\Delta\varphi$ is obtained from the equation $\Delta\varphi = \Delta\theta / \sin(\theta)$.

A CIS spectrum is obtained by measuring a set of spectra of the given core-level of the adsorbed atoms, spaced over a certain energy range, i.e. a set of energy distribution curves (EDC's). The photon energy $h\nu$ is chosen by keeping the momentum step Δk constant and calculating from the equation

$$h\nu = \eta^2 k^2 / 2m_e + \text{binding_energy} + \text{work_function}$$

Each EDC is fitted by Gaussian peaks with linear background (see Fig. 14). The area of the Gaussian peaks is defined as the intensity of the core-level peak. Since the photon flux changes with photon energy and time, all EDC signals are normalized to the mesh current, which is proportional to the photon flux. By plotting the intensity I(k) vs. k, we get a CIS

spectrum. Fig. 15(a) shows a typical CIS of the Ge 3d core-level for the Ge/Si(100)-2x1 sample.

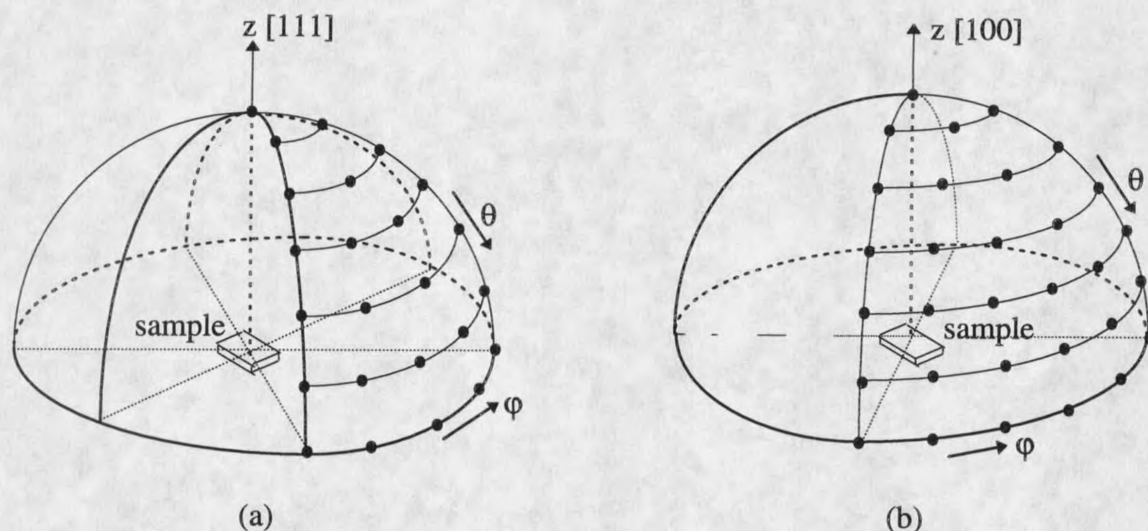

Fig. 13. Schematic drawings of measured CIS emission directions for (a) [111] and (b) [100] oriented surfaces.

A non-diffractive background $I_0(k)$ is generated for each CIS by means of a spline smoothing routine from GENPLOT [29], and then the normalized diffraction curve is given by $\chi(k) = I(k)/I_0(k) - 1$ (see Fig. 14). The choice of $I_0(k)$ does not cause any change of atom calculated position and only affects slightly the intensity ratio among the atoms in the final image [10].

The discrete $\chi(\mathbf{k})$ curves are then mapped to the whole emission hemisphere according to the symmetry of the sample. The small-cone method requires the number of CIS's to be equal for all small cones involved, so we need to make $\chi(\mathbf{k})$ continuous. A B-spline

interpolation method in three dimensions is used to form a continuous function $\chi(\mathbf{k})$ from the discrete data[10]. Then $\chi(\mathbf{k})$ is transformed to $\Phi_{\hat{k}}(\mathbf{R})$ in real space by Eq. (2.29). Finally, the image function $U(\mathbf{R})$ is obtained by small-cone summation in the form of Eq. (2.37).

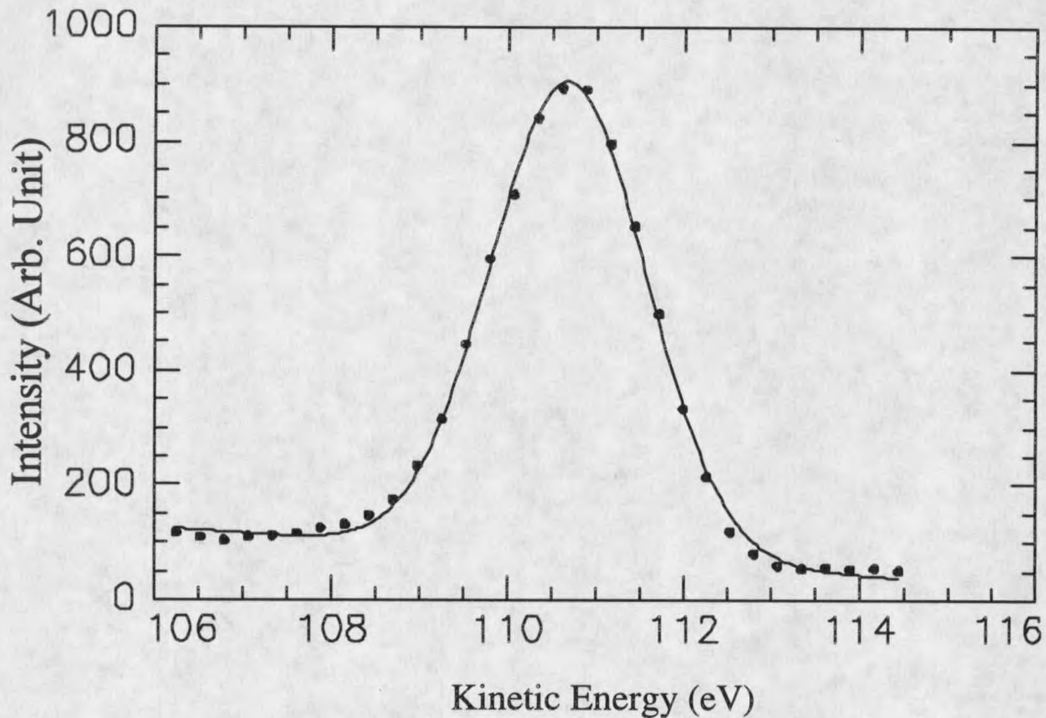

Fig. 14. A typical EDC of Ge 3d core-level (dots) and its Gaussian line-fitting (solid line) for Ge/Si(100)-2x1 sample. The photon energy is 145 eV and the emission direction is $\theta = 60^0$, $\varphi = 10^0$.

A coordinate transformation, from the small-cone coordinate system to the emission hemisphere coordinate system in which the experimental data are collected and analyzed, will

be encountered when constructing the image function U(**R**). Such transformation must ensure the same angular distribution of CIS's used with respect to the small-cone axis (θ_c, φ_c) for all small cones. The small-cone axis is chosen as the z' direction (see Fig. 6). A set of emission directions (θ_I', φ_I') are chosen in the small-cone coordinate system by keeping $\Delta\theta_I'$ constant while $\Delta\varphi_I' \approx \Delta\theta_I'/\sin(\theta_I')$. Next, we will explain how to transform the chosen angles (θ_I', φ_I') to the angles (θ_I, φ_I) in the emission hemisphere coordinate system.

The unit vector in the direction (θ_I', φ_I') in the small-cone coordinate system is

$$\mathbf{X}_i' = (\sin\theta_I'\cos\varphi_I', \sin\theta_I'\sin\varphi_I', \cos\varphi_I') \tag{3.1}$$

The matrix of the coordinate transformation is written as

$$M = \begin{pmatrix} \cos\theta_c \cos\varphi_c & -\sin\varphi_c & \sin\theta_c \cos\varphi_c \\ \cos\theta_c \sin\varphi_c & \cos\varphi_c & \sin\theta_c \sin\varphi_c \\ -\sin\theta_c & 0 & \cos\theta_c \end{pmatrix} \tag{3.2}$$

Thus, the unit vector $\mathbf{X}_i$ (x_i, y_i, z_i) in the direction (θ_I, φ_I) can be computed from

$$\mathbf{X}_i = \mathbf{X}_i' M^* \tag{3.3}$$

where M^* is the transpose matrix of M. Then, the angles (θ_I, φ_I) in the emission hemisphere coordinate system can be obtained by

$$(\theta_I, \varphi_I) = (\cos^{-1}(z_i), \tan^{-1}(y_i/x_i)) \tag{3.4}$$

Finally, the software MATHEMATICA [30] is used to construct a continuous image function in three dimensions from the discrete image function U(**R**) and display the images.

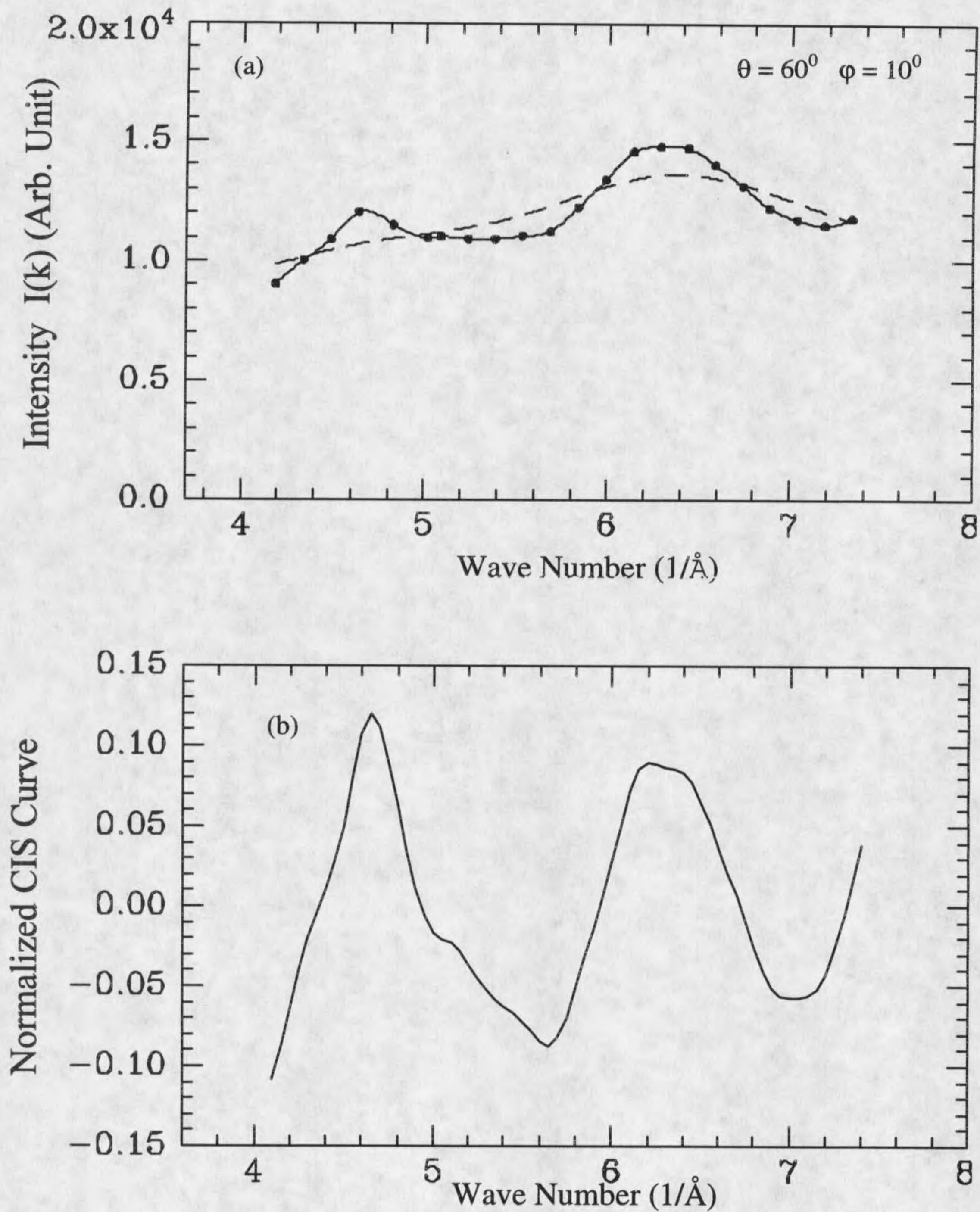

Fig. 15. (a) A CIS curve I(k) (dots and solid line) of Ge 3d and its non-diffractive curve $I_0(k)$ (dashed line) for Ge/Si(100)-2x1; (b) normalized diffraction curve $\chi(k)=I(k)/I_0(k)-1$.

CHAPTER 4

INSTRUMENTATION AND EXPERIMENTAL PROCEDURES FOR STUDIES OF MBE-GROWN GaAs (111) SURFACES

Instrumental Layout

The experiments for the studies of MBE-grown GaAs(111) surfaces were performed at the Center for Research in Surface Science (CRISS), Montana State University-Bozeman. The system has two main UHV chambers, a MBE growth chamber (Perkin-Elmer model 430) and analysis chamber, connected by an UHV transfer tube. The MBE growth chamber is equipped with an 10 keV reflection high-energy electron diffraction (RHEED), a quadrupole mass analyzer (QMA) and Knudsen effusion cells for Ga, As and Si sources. The analysis chamber is equipped with HREELS, LEED, XPS, UPS and QMA. Figure 16 shows a schematic of the MBE growth chamber, while the schematic drawing of the analysis is depicted in Fig. 17.

The MBE growth chamber is pumped by a Perkin-Elmer ion pump to maintain the vacuum pressure about 8×10^{-11} torr. The analysis chamber is pumped by a Varian ion pump, a Leybold turbo pump backed with a mechanical pump, as well as a titanium sublimation pump

(TSP). The base pressure in the analysis chamber is about $1x10^{-10}$ torr. The transfer tube, where the pressure is kept at $1x10^{-9}$ torr, is pumped by a Varian ion pump and a TSP.

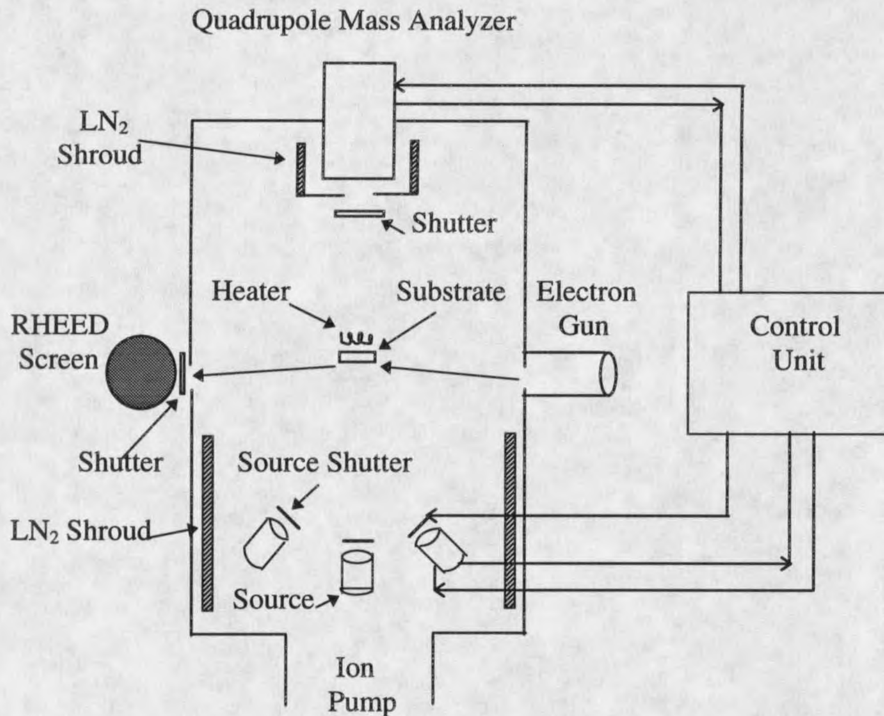

Fig. 16. Schematic diagram of the molecular beam epitaxy (MBE) system.

The data acquisition system consists of a host computer, CAMAC and a data acquisition unit (DAU) which is a computer built-in the control unit for the Leybold multichannel energy analyzer used in XPS and UPS. The host computer is a HP-300 series and is interfaced with the DAU and CAMAC system. The CAMAC crate contains a GPIB crate controller, a timer scaler and a 4-channel 16 bit digital to analog converter (DAC). The output of the DAC is connected via an operational amplifier in series with the HREELS ramp

control unit to scan the analyzer slit potential. The channeltron signal is amplified by a preamplifier and passes through a filter which discriminates low amplitude noises and outputs TTL pulses to a ratemeter and timer scaler. The counts are then read by the computer and stored. For the DAU, the host computer only specifies the scan parameters and the DAU controls the scan. After each scan, the DAU transfers the data to the host computer.

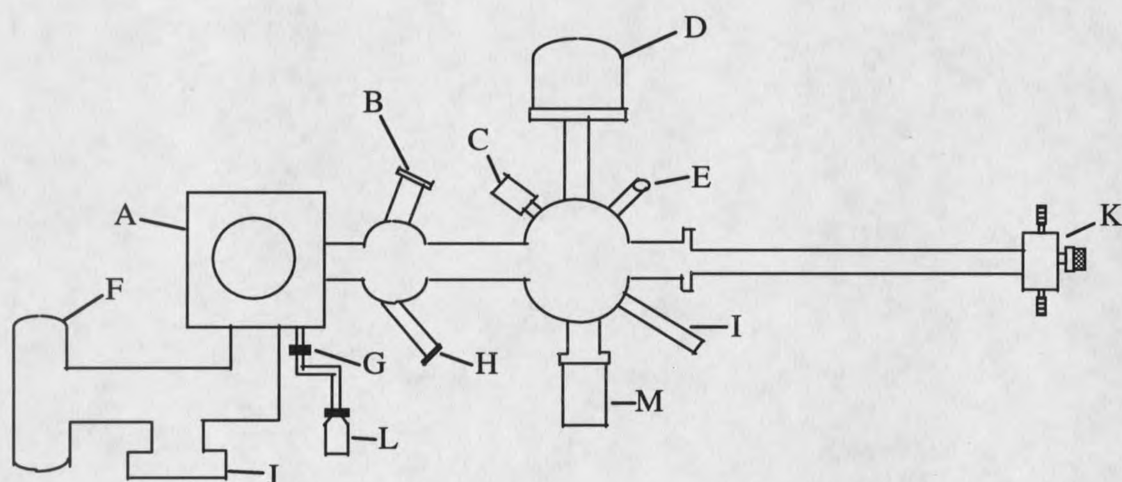

Fig. 17. Analysis chamber layout. (A) HREELS chamber; (B) LEED optics; (C) X-ray source; (D) Hemisphere energy analyzer; (E) Ultra-violet lamp; (F) Ion pump; (G) Leak valve; (H) Quadruple mass analyzer; (I) Quartz crystal oscillator; (J) Titanium sublimation pump; (K) x, y, z and θ manipulator; (L) Hydrogen gas tank; (M) Turbo pump with a mechanical pump.

Molecular Beam Epitaxy System (MBE)

A MBE system is basically a vacuum evaporation apparatus. The source ovens are resistivity-heated effusion cells with molybdenum cracking tube for the arsenic source to break tetramers down to dimers. The arsenic effusion cell with the cracker is capable of evaporating and cracking As_4 into As_2 for better sticking probabilities [31]. There are five effusion cells in the growth chamber, but only three of them are shown in Fig. 16, for providing Ga, As and the dopant Si elements. Thermocouples and shutters are provided for each oven, and the entire assembly is surrounded by a liquid-nitrogen shroud for cooling. The substrate is mounted on a holder about 8 inches from the orifices of the ovens. The holder is attached to a manipulator for precise positioning. The substrate is heated to the appropriate temperatures for epitaxial growth. It can also be heated before deposition for cleaning, and after deposition, for various heat treatments if desired.

In addition to sources and substrate, some supporting equipment is provided for the purposes of monitoring, analyzing and controlling. A UTI quadruple mass analyzer is located on top of the chamber and consists of three sections: the radio-frequency (RF) generator, the probe and the control console. It scans both the vaporizing and the residual species in the system. Another unit shown in Fig. 16 is a refection high energy electron diffraction (RHEED). The forward scattering geometry of RHEED is most appropriate for MBE in-growth surface analysis, since the electron beam is at grazing incidence whereas the molecular beams impinge almost normally on the substrate; thus, there is no interference between the

two units. An electron beam with 10 keV energy is directed at a low angle ($1^0 - 3^0$) to the surface of the film. Some of the electrons are reflected from the film and some are diffracted by the atoms arranged in the first few atomic layers. The diffracted electrons produce a pattern on a phosphor screen. The patterns contain a great deal of the information about the crystalline structure, the smoothness, and the thickness for certain surfaces. For this reason it is used to monitor the ordering and quality of the film that is grown.

High Resolution Electron Energy Loss Spectroscopy (HREELS)

HREELS is a very surface sensitive technique to study the vibrations of the surface phonon and plasmon modes and of chemisorbed molecules. Most HREELS spectrometers are based on a pair of 127^0 cylindrical capacitors employing real slits and coupled to a simple double-plate lens system [34]. This design was developed by Ibach [32] and Froitzheim [33] and has been proven very successful.

Electrons, emitted from a tungsten filament, are focused by three electrodes onto the monochromator entrance slit. After passing the two stages of monochromatization, the electron beam is accelerated to the primary beam energy and focused on the sample by two electrodes. The electrons reflected from the sample are decelerated and focused onto the analyzer entrance slit. The analyzer is very similar to the monochromator, except the slit potential is ramped to scan the energy. In this way, the whole spectrum enters the analyzer, but only the electrons with an energy equal to the path energy will reach the detector.

XPS, UPS and LEED

X-ray photoemission spectroscopy (XPS) uses the characteristic K_α emission line of the x-ray tube with the Al anode or the M_ζ emission line of the Zr anode provided in the x-ray tube to excite photoelectrons. The photon energy is 1486.4 eV for the Al anode and 151.4 eV for the Zr anode. Ultra violet photoemission spectroscopy (UPS) uses the narrow characteristic line of a noble gas (e.g. He, Ne) discharge glow to study the valence band structures of the samples. The discharge is induced by high voltage (about 700 eV for He, 200 eV for Ne) applied at two ends of a quartz capillary, which is called the discharge capillary. The generated ultra-violet light is led to the UHV chamber by another capillary (called the UHV guide capillary), with an inner diameter of about 1 mm. It is thus necessary to differentially pump the system in two stages. In this way, the pressure in the UHV chamber then can be maintained at lower 10^{-9} torr range. In this laboratory, the UPS is equipped with He gas. There are two lines, at 40.8 eV and 21.2 eV. The change of gas pressure will vary the intensity ratio of these two lines. The energy analyzer used for XPS and UPS is very similar to the one described in Chapter 3.

In our experiments, LEED is supplementary and used to monitor the surface order. It is a Varian four-grid electronic optics with a fluorescent screen and a power supply. The sample is placed at the spherical center of the grids. The inner grid and sample usually have the same potential to ensure a field-free region between the sample and the grids. The second and third

grids are used as a suppressor to obtain a sharp and low background pattern. The fourth grid is held at ground to shield the double grids from the screen voltage.

Sample Preparation

The GaAs(111) substrate (semi-insulating), supplied by American Xtal Technology, was mounted with indium solder on a molybdenum block. Then it was transferred into the transfer tube through the interlock chamber from air. After the substrate with the holder was outgassed at about 200^0 C for about two hours in the transfer tube, it was transferred into the MBE growth chamber. The liquid nitrogen was used to keep the growth chamber cool and prevent re-evaporation of impinging atoms, thus keeping the working pressure low. Ga, As and Si sources need to be heated for several hours before reaching the stable evaporating temperature. The oxide layer on the surface of the substrate was thermally removed by gradually heating it to about 600^0 C with an As over-pressure to maintain a stoichiometric surface[35]. The sample temperature was monitored by a thermocouple and also an infrared pyrometer. Then the substrate was cooled down to the growth temperature ranging from 525^0 C to 575^0 C. Before starting growth, the flux ratio between As and Ga was measured by the mass spectrometer and has adjusted to be in the range of 5 – 10. Then the growth with Si-doping was started by opening the Ga source shutter while the substrate was kept at about 550^0 C. The surface structure during the growth was monitored by RHEED. After growth, the sample was transferred into the analysis chamber through the UHV transfer tube without

exposure to air. The XPS and HREELS measurements showed no contamination on the surface, and the surface showed a very sharp LEED pattern.

To study the hydrogen adsorbed surfaces, the chemisorption surfaces were prepared by exposure to atomic hydrogen generated by a hot (2000 K) tungsten filament, which was used to dissociate hydrogen molecules. The filament was in the line of sight of the surface at a distance of 4 cm. The values for exposures are recorded in Langmuirs (1 L = 1×10^{-6} Torr·second) to denote the product of the total pressure (measured by an ion gauge) and the time of exposure.

CHAPTER 5

EXPERIMENTAL RESULTS AND DISCUSSION OF PHOTOELECTRON HOLOGRAPHY

Three samples, Se/Ge(100)-1x2, Ga/Ge(111)-1x1 and Ge/Si(100)-2x1, are investigated and analyzed by the small-cone photoelectron holographic imaging technique. The results and analyses are presented in this chapter. The comparison with the experimental or theoretical results obtained by other techniques, if available, are reported as well.

Se/Ge(100)-1x2

The clean Ge(100) surface under real conditions, like the Si(100) surface, has many terraces separated by monatomic steps. Each terrace shows a 2x1 reconstruction due to dimer formation of the surface Ge atoms, as shown in Fig. 18. As a result, the dimer-row directions on the adjacent terraces are perpendicular to each other, together forming two domains with a mixed 2x1+1x2 LEED pattern. One domain, whose dimer-row direction is parallel to the step-edge, is named type A, while another domain, whose dimer-row direction is perpendicular to the step-edge, is named type B [27]. This convention is often called the Chadi notation [27], which is the opposite of that originally suggested by Kroemer [36].

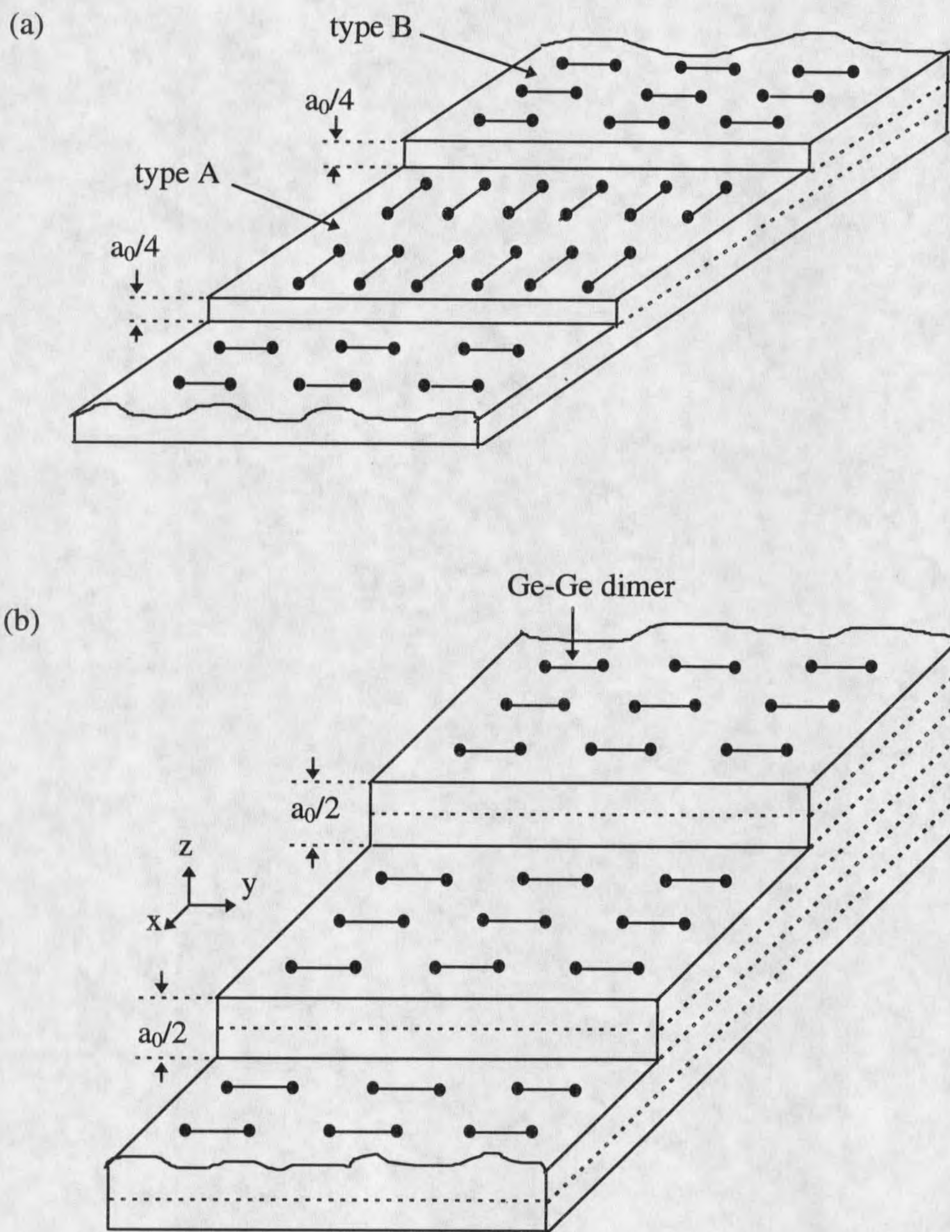

Fig. 18. (a) A Ge(100) surface. Three terraces shown are separated by two monatomic steps, type A and type B. (b) A 4^0 vicinal cut Ge(100) surface with only type B of terraces separated by double steps. a_0 is the lattice constant, which is 5.646 Å for Ge.

The measurements on a perfectly oriented (100) surface will involve both domains, and therefore be ambiguous. It is found that a vicinal (100) surface with the normal direction about 4^0 off the (100) direction has the terraces separated by only biatomic steps with the terrace width about 40 Å [27]. Thus, the dimer-row directions on the different terraces are all the same and the surface will show a single domain 2x1 LEED structure. Figure 18(b) is schematic drawing of a 4^0 miscut along (110) direction of Ge(100), which has only single type of terrace (type B). To make the system simpler and unambiguous, this 4^0 vicinal cut Ge(100)-2x1 surface was used in the experiment.

After Se was chemisorbed on the Ge(100) surface, the surface reconstruction has changed from a 2x1 LEED pattern to a 1x2 LEED pattern. A total of 97 CIS's were taken from the Se 3d core level. The CIS collection range was from 0^0 to 82.5^0 in polar angle with $\Delta\theta = 7.5^0$ and from 0^0 to 90^0 in azimuthal angle. Figure 19 shows a typical CIS with $I_0(k)$ and its normalized curves. The angular dependence of the phase and amplitude of the CIS inversion $\Phi_{\hat{k}}(\mathbf{R})$ at the position of Ge atom D is depicted in Fig. 20. It indicates that on the emission hemisphere there exists a small cone with about 20^0 half-width. Inside the cone, $\Phi_{\hat{k}}(\mathbf{R}_D)$ has a relatively constant phase with a larger amplitude. Thus, the small-cone with a 20^0 half width is chosen for the summation of $\Phi_{\hat{k}}(\mathbf{R})$.

The resultant image is the intensity function over three dimensions, which can only be displayed in two dimensions, i.e. a planar cut. The atomic images at different planar cuts are shown in Fig. 22(a-c), where the coordinates are shown in Fig. 18(b). The x axis is chosen along the dimer-row direction of the clean surface, the y axis is chosen along the step-edge

direction (that is the dimer direction) of the clean surface and the z axis is along the surface normal direction. The emitter (Se atom) is at the origin. Figure 22(a) is the horizontal planar cut of the image function at z = -1.2 Å. It reveals the four spots labeled by A, B, C and D. The intensity of spots C and D is about 75% of the intensity of spots A and B. Figure 22(b) is the vertical planar cut of the image function at x = 0 Å, which passes through spots A and B. Figure 22(c) is the vertical planar cut of the image function passing through spots C and D at y = 0 Å. The positions of the four spots are listed in Table 1. Fig. 23 shows the line scans passing through the spot B. These four spots with the intensity maxima are due to the surface Ge atoms from two types of regions, described as follows.

The photoelectron holography reveals the local atomic geometry around the emitter, and the LEED pattern reveals the long-range order on the surface. Thus, it is necessary to analyze both the holographic images and the LEED pattern to obtain the model of surface structures. From the atomic images (Fig. 22(a-c)) together with the LEED structures (shown in Fig. 24), the following model is proposed for Se/Ge(100)-1x2 system. During Se chemisorption, Ge dimers on the terraces are broken, and the Se atoms stay at the bridge sites bonded with the nearest two Ge atoms. In addition, some Ge atoms are displaced from the outer monolayer and migrate over the terrace to adhere to the nearest step edge, giving the appearance of simple step flow. This displacive phenomenon has been observed on the As/Si(100) by Scanning Tunneling Microscopy (STM) and Low-Energy Electron Microscopy (LEEM) [71, 72], and on Ge/Si(100) by LEEM [41]. Then, some Se atoms occupy the bridge sites on the displaced terraces at every other row and bond with the nearest Ge atoms.

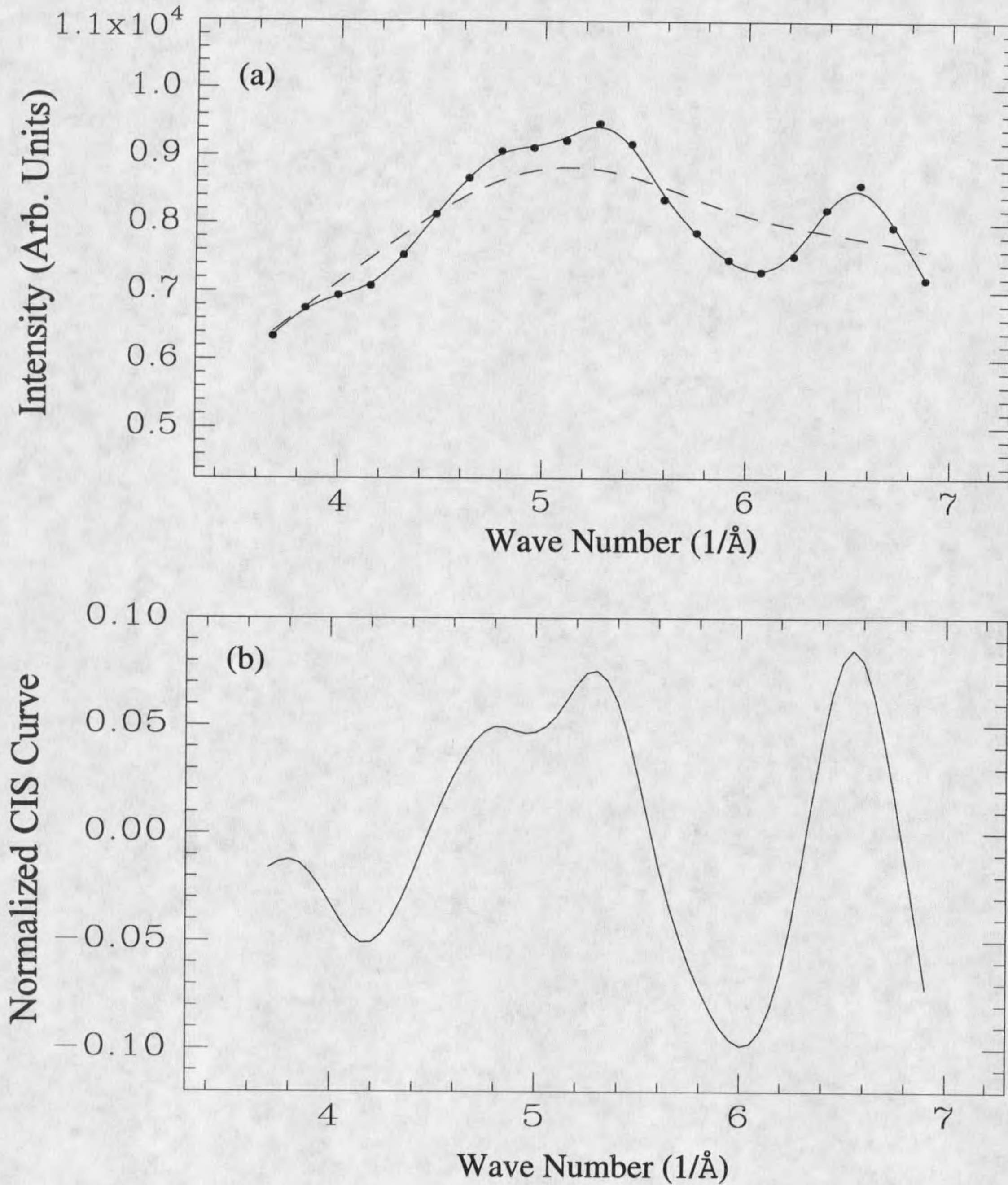

Fig. 19. (a) A CIS curve I(k) (dots and solid line) of Se 3d and its non-diffractive background curve $I_0(k)$ (dashed line) for Se/Ge(100)-1x2; (b) its normalized diffraction curve $\chi(k) = I(k)/I_0(k)-1$. It was taken at $\theta = 67.5^0$ and $\varphi = 90^0$.

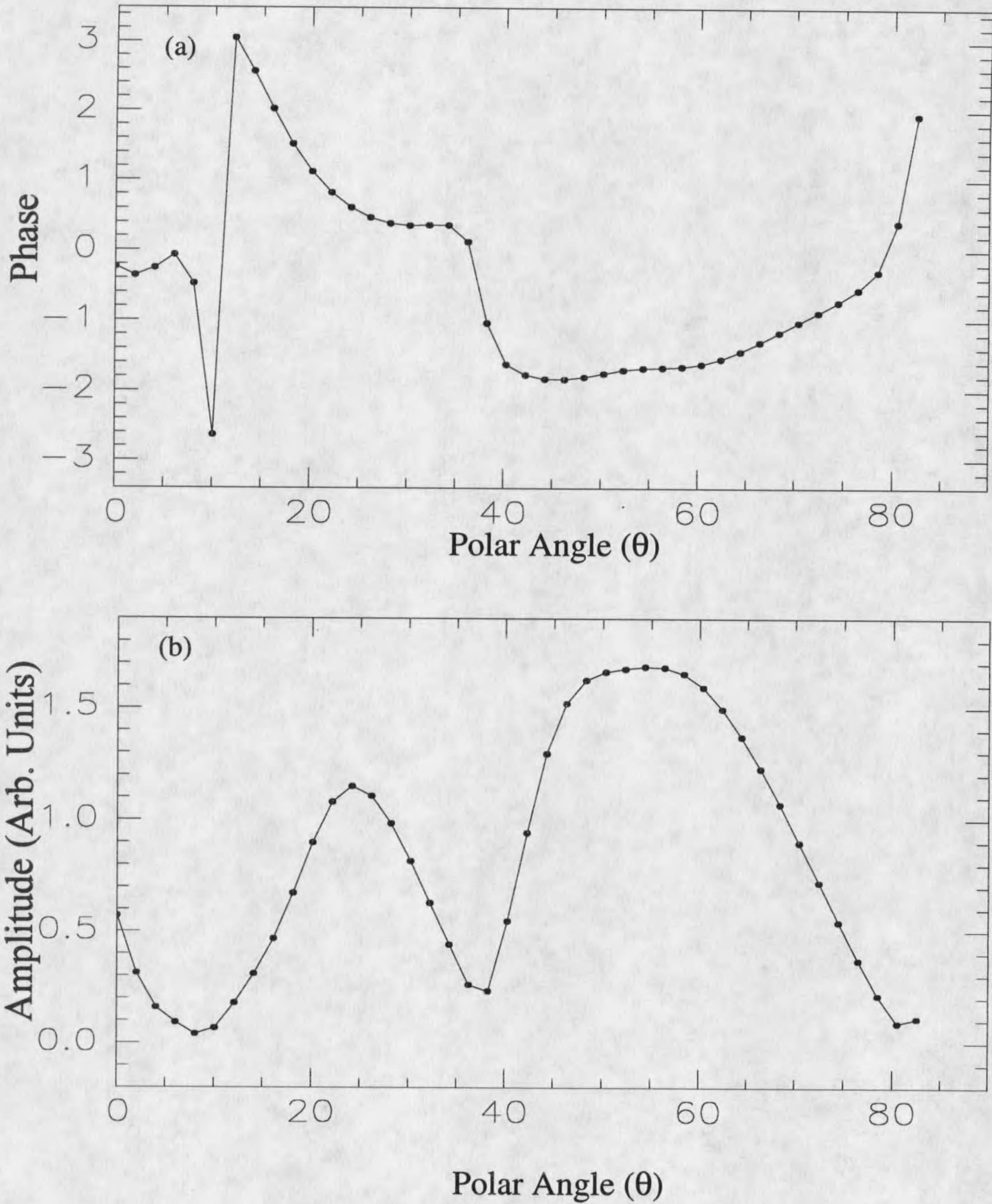

Fig. 20. (a) Phase and (b) amplitude of the CIS inversion vs. polar angle at the position of Ge atom D for Se/Ge(100)-1x2 sample. The azimuthal angle φ is 180^0.

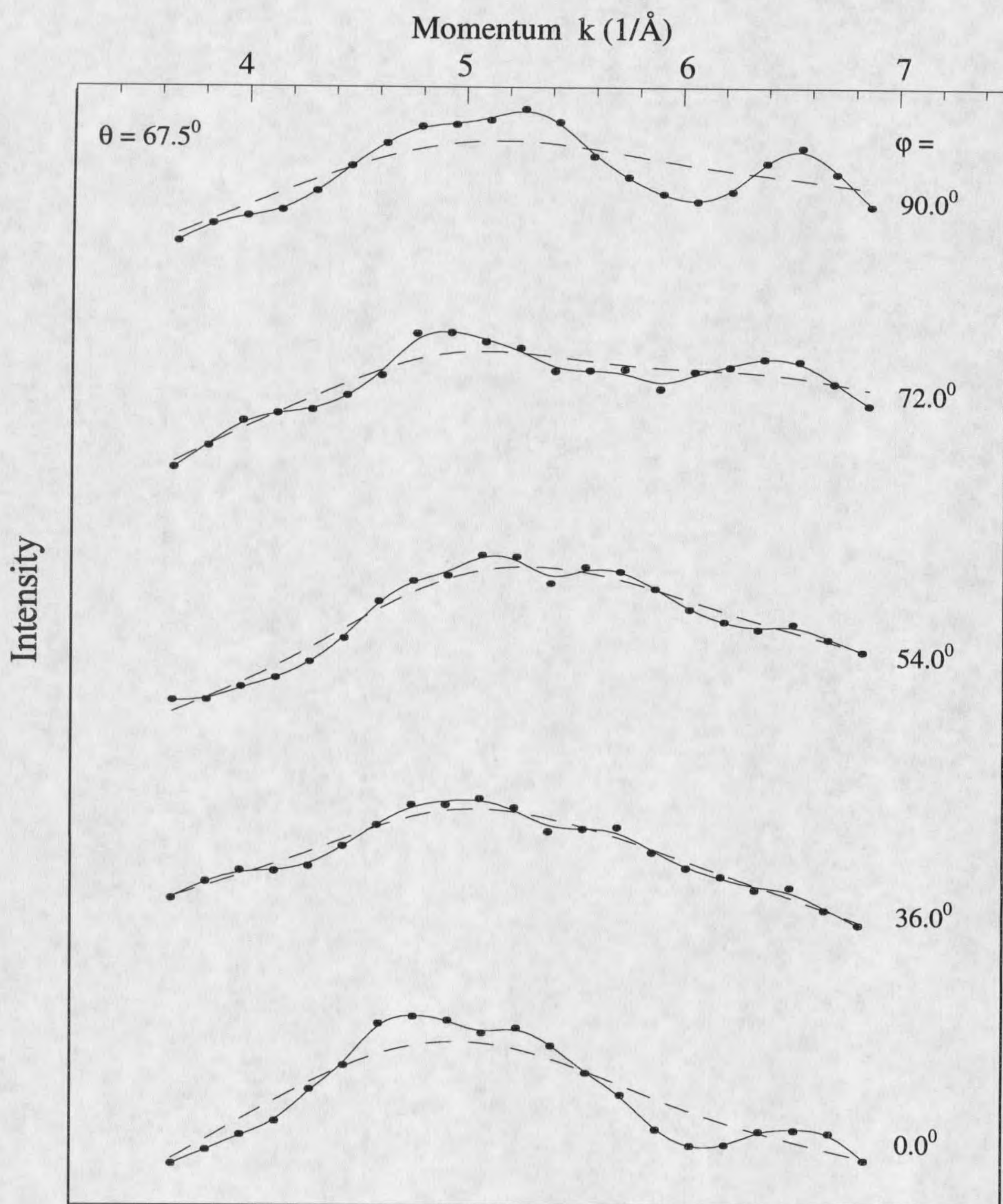

Fig. 21. Some CIS I(k) curves (dots and solid lines) from the Se 3d core level and their non-diffractive background $I_0(k)$ curves (dashed lines) for Se/Ge(100)-1x2 sample.

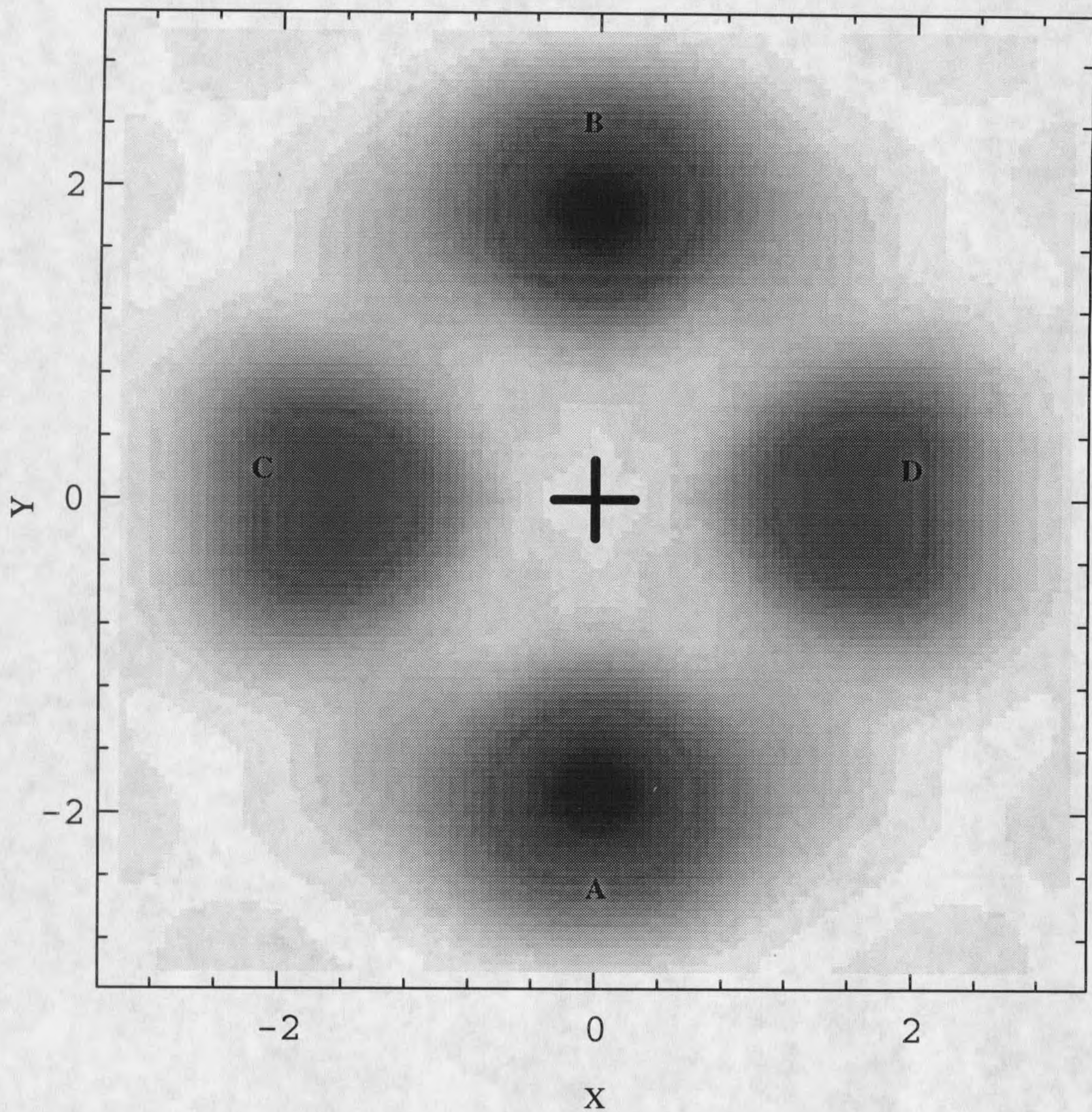

Fig. 22(a) X-Y horizontal planar cut of the image function for Se/Ge(100)-1x2 at z = -1.2 Å. The intensity maxima labeled by A, B, C and D are due to the first-layer Ge atoms. The intensities of spots C and D are about 75% of the intensities of spots A and B. Coordinate units: Å.

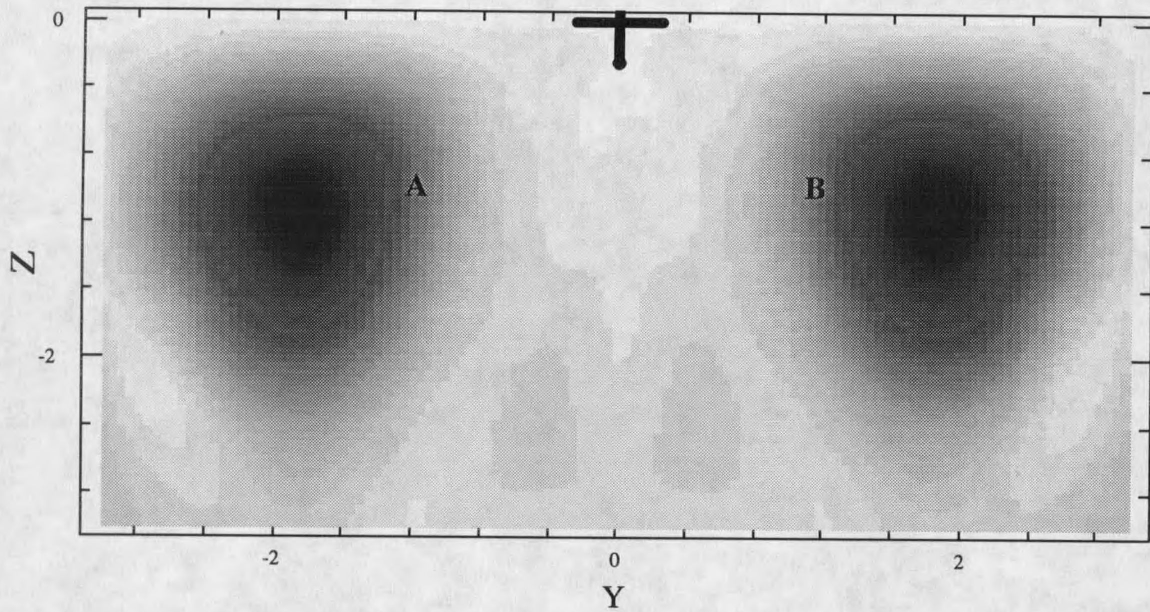

Fig. 22(b) Y-Z vertical planar cut of the image function at x = 0 Å for Se/Ge(100)-1x2. The cross marks the emitter position. The intensity maxima labeled by A and B are due to the first-layer Ge atoms. Coordinate units: Å.

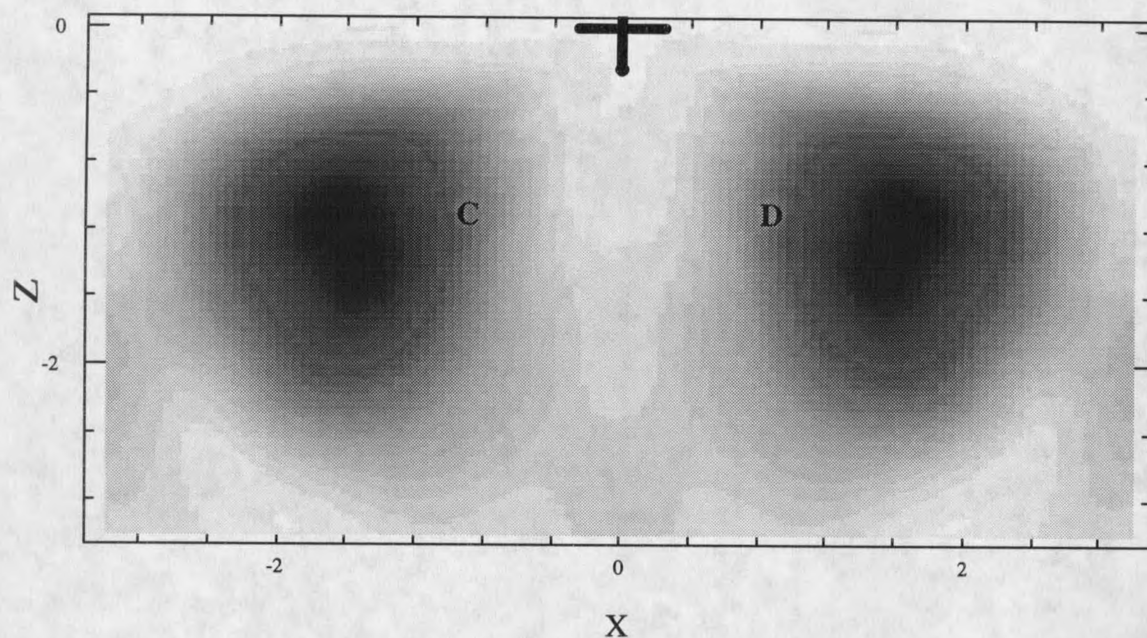

Fig. 22(c) X-Z vertical planar cut of the image function at y = 0 Å for Se/Ge(100)-1x2. The cross marks the emitter position. The intensity maxima labeled by C and D are due to the first-layer Ge atoms. Coordinate units: Å.

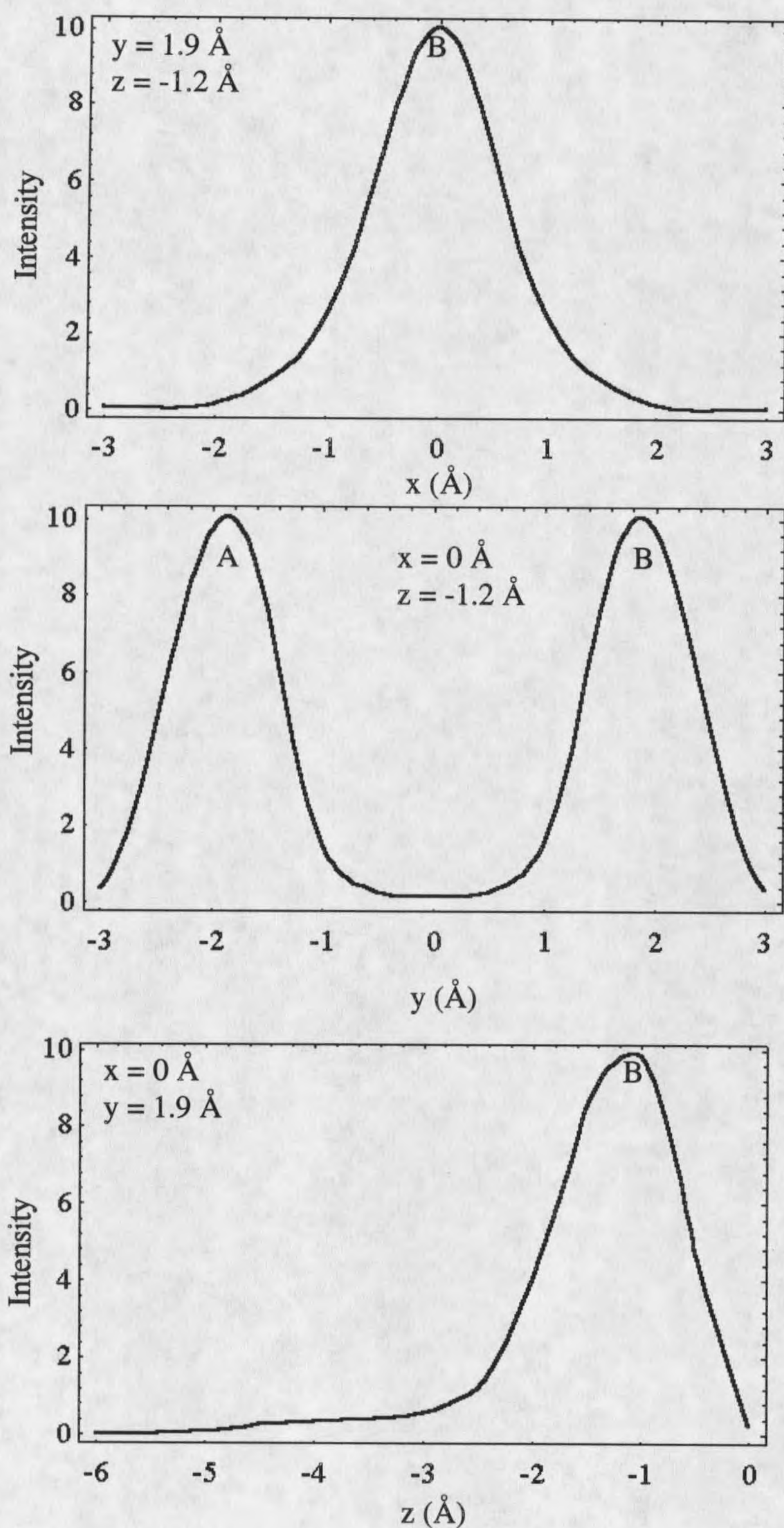

Fig. 23. Line scans passing through the spot B for Se/Ge(100)-1x2.

In terms of the above assumption, the atomic images in Fig. 22(a-c) and the LEED pattern in Fig. 24 can be explained as follows. The Se adsorption breaks the Ge dimers and some Se adatoms occupy the bridge sites bonding with the nearest two Ge atoms, which gives the two spots A and B in the atomic images. In this case, the LEED structure is 1x1. For the regions terminated by such Se adatoms, the Ge dangling bonds are saturated. From the point of view of surface energy, this surface reconstruction is favorable since all the dangle bonds are saturated, which usually implies the lower surface energy. Schematically, the situation is shown in region I of Fig. 25.

In addition, the adsorption of Se is accompanied by the displacement of Ge atoms from some regions of the surface. The displacive adsorption process may relate to the reduction of the surface stress, as explained by Tromp *et al* for the As/Si(100) [72] and Ge/Si(100) [41] samples. The step edge may also play a significant role in the displacive adsorption. The expelled Ge atoms move laterally and participate in growth at step edges. Some of the Se atoms then occupy the bridge sites on the displaced surface in every other row and bond with the nearest two Ge atoms, which gives the two spots C and D in the atomic images. This situation is shown in region II of Fig. 25. On the clean Ge(100)-2x1 surface, the Ge dangling bonds or Ge dimers are directed parallel to the step edge (i.e. along the y direction). After the surface Ge atoms are removed by the Se adsorption, the Ge dangling bonds are pointed perpendicular to the step edge (i.e. along x direction). Therefore, the Se atom occupation at the bridge sites in every other row results in the 1x2 single-domain LEED structure.

Based on the above discussion, one can see that two types of regions coexist on the surface. One is a fully Se-terminated region without displacive adsorption (region I), which produces the two spots A and B in the images and 1x1 LEED pattern. The emitters (Se atoms) in this type of regions are all equivalent adsorption sites. Another type is half Se-terminated region on the Ge atom displaced surface (region II), which produces the two spots C and D and 1x2 LEED pattern. The emitters (Se atoms) in region II are all in equivalent adsorption sites, but inequivalent from the emitters in region I. Since the photoelectron holographic image indicates an overall effect of the photoelectron diffraction contributed by all the emitters (Se atoms), the resultant images shows the four spots A, B, C, and D. The mixture of 1x2 and 1x1 LEED patterns still shows a 1x2 pattern.

The positions of the four spots in the atomic images, that are the atomic positions, are listed in Table 1. The atomic positions in the images could be off by the maximum of 0.2 Å. The emitter (Se atom) is at the origin. From the atomic positions, the bond lengths can be calculated. The bond length of Se-Ge in region I is 2.25 Å, the bond length of Se-Ge in region II is 2.1 Å. So far, no other experimental results or theoretical calculations are found in the literature for comparison.

Table 1. The Ge atom positions for the Se/Ge(100)-1x2 sample. The origin is the emitter (Se atom). Coordinate unit: Å.

Ge atoms labeled by	Corresponding Ge layer	Atomic position
A	first	(0, -1.9, -1.2)
B	first	(0, 1.9, -1.2)
C	first	(-1.7, 0, -1.2)
D	first	(1.7, 0, -1.2)

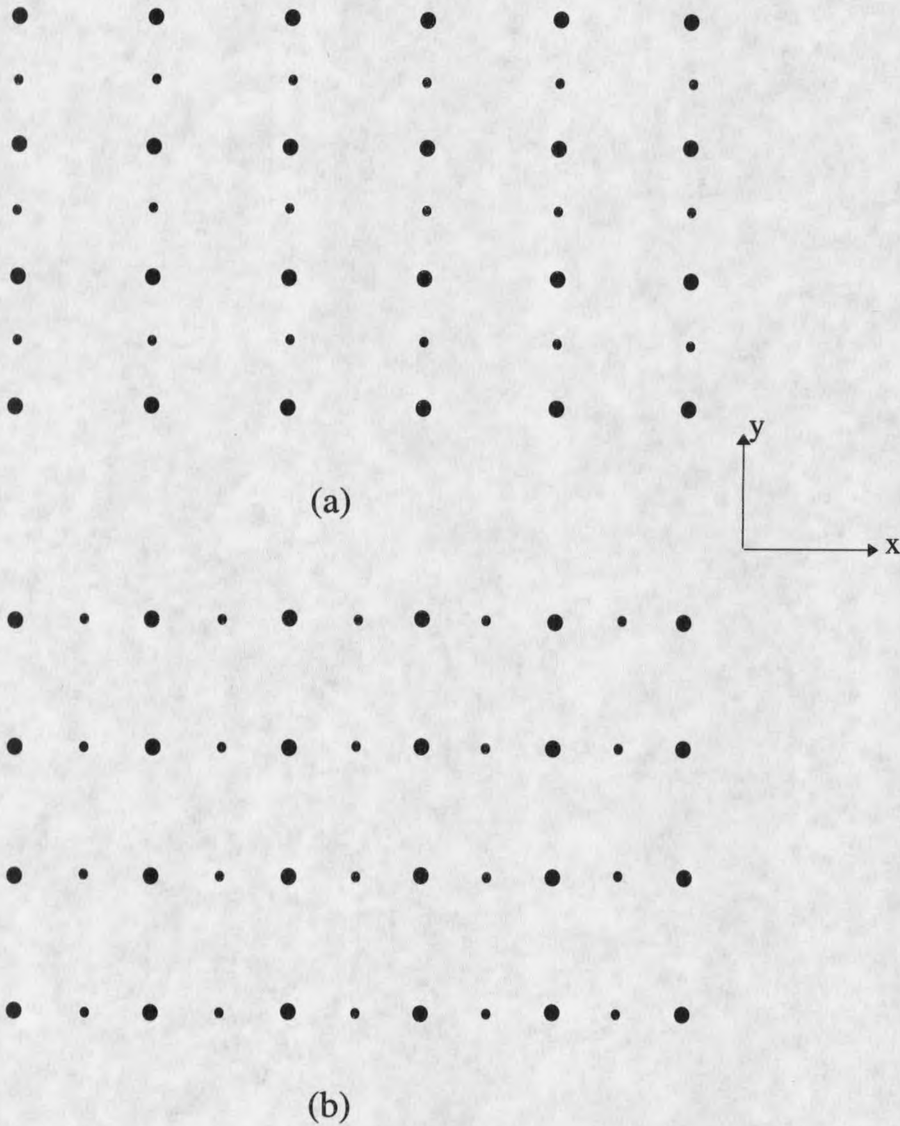

Fig. 24. Schematic drawings of (a) 2x1 single-domain LEED pattern for the clean Ge(100) surface; (b) 1x2 single-domain LEED pattern for the Se/Ge(100) sample. Y axis is along the step edge direction.

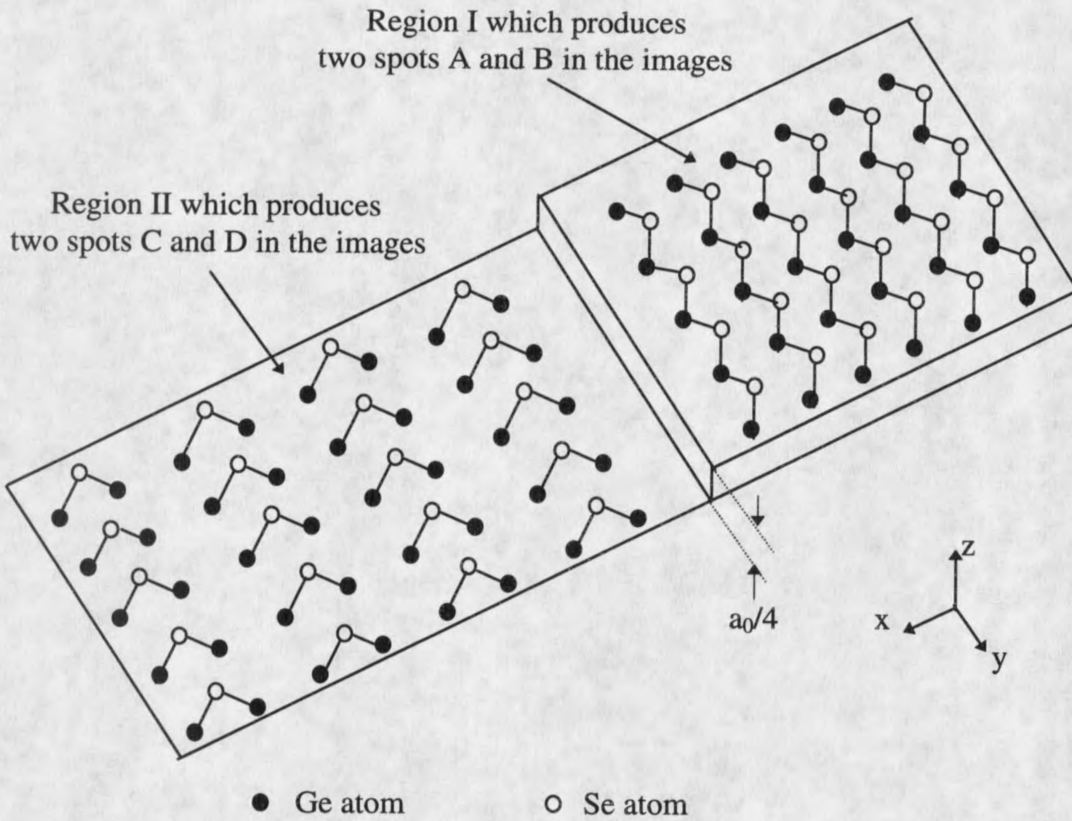

Fig. 25. Schematics of the Se/Ge(100)-1x2 structure. The surface contains two types of regions. Region I is fully Se-terminated region, on which the displacement of Ge atoms does not occur. This type of regions produces the two spots A and B in the atomic images and gives a 1x1 LEED pattern. Region II is half Se-terminated and the Se atoms adsorb on the Ge displaced region. This type of regions produces the two spots C and D in the atomic images and gives a 1x2 LEED pattern.

Ga/Ge(111)-1x1

After several cycles of Ar^+ sputtering and annealing, the clean Ge(111) surface shows a sharp c(2x8) LEED pattern. Figure 26 depicts the c(2x8) LEED structure and the surface reconstruction in real space [38]. It is an adatom structure, where the Ge adatoms occupy the three-fold symmetric sites atop second-layer substrate atoms (called T_4 sites) [38, 39]. After 0.6 monolayer gallium is deposited on the clean Ge(111) substrate held at room temperature, it shows a 1x1 LEED pattern with a somewhat high background. Figure 27 shows a typical wide-scan energy distribution curve for this sample at the photon energy of 130 eV. A total of 72 CIS's were taken from the Ga 3d core level. The collection range was from 0^0 to 82.5^0 in polar angle with $\Delta\theta = 7.5^0$ and from 0^0 to 60^0 in azimuthal angle. Figure 28 shows a typical CIS curve and its normalized curve. The phase and amplitude of the CIS inversion at the position of Ga atom A vs. the polar angles is indicated in Fig. 7. One can see that the half width of the small-cone is about 20^0, which was used in the data analysis.

The four atomic images are displayed in Fig. 30, where the coordinates are chosen from the LEED pattern (see Fig. 26(a)). Figure 30(a) is the X-Z vertical planar cut of the image function at y = 0 Å, where the cross at the origin represents the position of the emitter (Ge atom). It indicates four spots, labeled by A, B, E and H. Figure 30(b) is the X-Y horizontal planar cut passing through the second-layer Ge atom A at z = −2.3 Å. Figure 30(c) shows the X-Y horizontal planar cut of the image function at z = − 1.2 Å. It reveals six spots,

marked by B, C, D, E, F and G. They represent the first-layer Ge atoms. The intensity of spots B, D and F is about 10% of the intensity of spot A while it is about 8% for the spots C, E and G, as compared to the intensity of spot A in Fig. 30(a-c). The spot at the center in Fig. 30(c) is the tail of spot A, which can be seen in Fig. 30(a) or from the line scans shown in Fig. 31. Figure 30(d) is the X-Y horizontal planar cut passing through the third-layer Ge atom H at $z = -4.9$ Å. The intensity of spot H is about 6% of the spot A intensity in Fig. 30(a).

There are three possible positions where the Ga adsorbates might occupy; they are the on-top, T_4, and H_3 sites. If the Ga atoms were to occupy the top sites, then we should see that one Ge atom is below the emitter on the first-layer, followed by three Ge atoms on the second-layer in the atomic images. However, this case does not appear in the images and hence the top sites are excluded. If the Ga atoms are located on the T_4 sites, then the images will show three Ge atoms on the first-layer (spots B, D and F in Fig. 30(c)), and one Ge atom below the emitter on the second-layer (spot A in Fig. 30(a) and Fig. 30(b)), and further another Ge atom also below the emitter on the third-layer (spot H in Fig. 30(a) and Fig. 30(d)). This agrees with the observation, and it is therefore concluded that the Ga atoms do occupy T_4 sites. The other three spots C, E and G in the images demonstrate that the Ga atoms also occupy H_3 sites. This argument is consistent with the LEED results. Since some of the Ga atoms occupy T_4 sites, while others occupy H_3 sites, the surface is disordered. This will give us 1x1 LEED pattern with a high background.

In conclusion, the Ga adsorbates occupy both T_4 and H_3 sites, and will form the Ga-Ge bonds. Figure 32 depicts the T_4 site and H_3 site occupied by Ga atoms. All atomic positions

are listed in Table 2. The maximum discrepancy in our data is 0.2 Å. Table 3 lists the comparison of the bond lengths between this work and the theoretical calculation by Ricart *et* al [40]. The model used in the theoretical calculation is based on the assumption of the $\sqrt{3} \times \sqrt{3}$ LEED pattern, thus the calculation is done by assuming the Ge atom on either T_4 site or H_3 site.

Table 2. The atomic positions for Ga/Ge(111)-1x1 system obtained from this experiment.

Ge atom labeled by	Corresponding Ge layer	Atomic position (Å)
B	first	(-2.0, 0.0, -1.4)
C	first	(-1.0, 1.7, -1.2)
D	first	(1.0, 1.8, -1.4)
E	first	(2.0, 0.0, -1.2)
F	first	(1.0, -1.8, -1.4)
G	first	(-1.0, -1.7, -1.2)
A	second	(0.0, 0.0, -2.3)
H	third	(0.0, 0.0, -4.9)

Table 3. Comparison of the bond lengths between this work and the theoretical calculation by Ricart *et al* [40] for the Ga/Ge(111) system. All the lengths are in Å.

	T_4 site		H_3 site	
	Ga-Ge	Ge-Ge	Ga-Ge	Ge-Ge
This work	2.49	2.25	2.33	N/A
Calculation	2.53	2.54	2.65	2.48

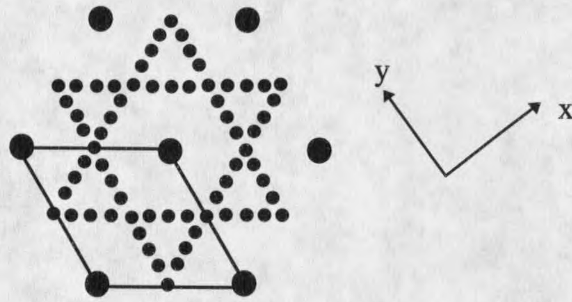

(a)

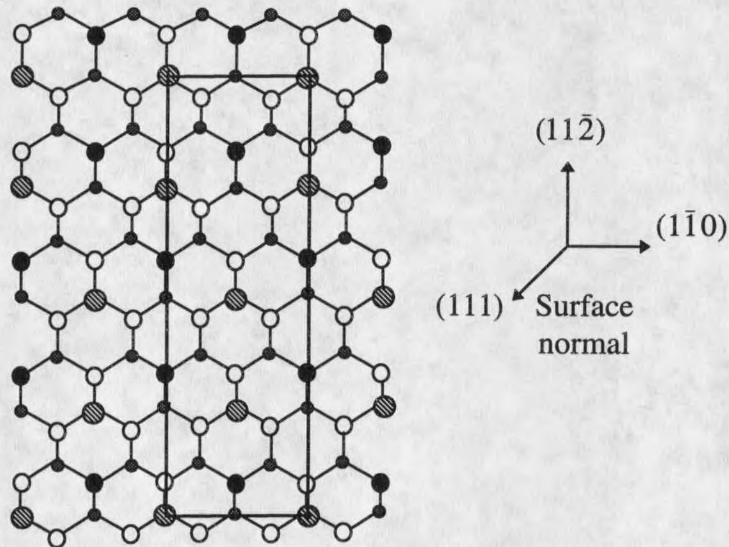

(b)

Adatom ● 1st-layer rest atom ○ 1st-layer non-rest atom • 2nd-layer atom

Fig. 26. Schematic representation of (a) the LEED structure and (b) the reconstructed surface in top view for the Ge(111)-c(2x8) sample. The bold lines outline the c(2x8) unit cell.

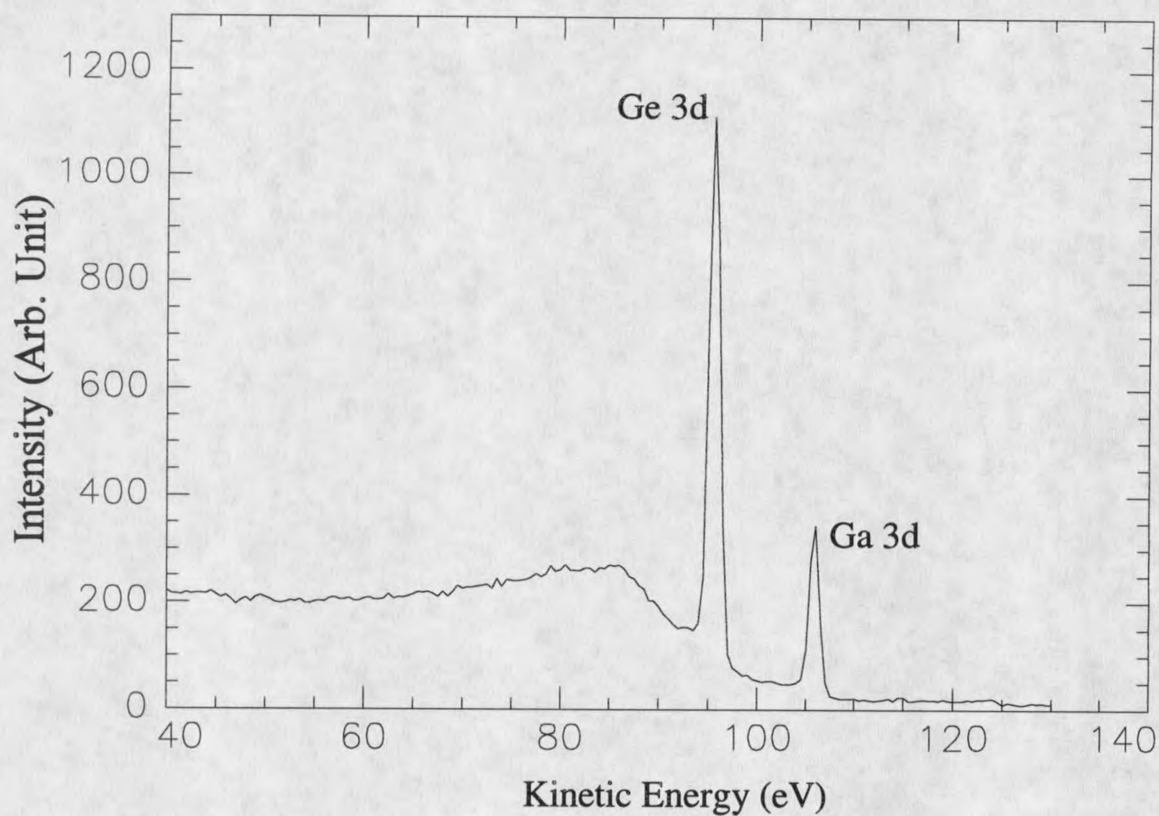

Fig. 27. Energy distribution curve at a photon energy of 130 eV for the Ga/Ge(111)-1x1 system. It was taken at $\theta = 82.5^0$ and $\varphi = 0^0$.

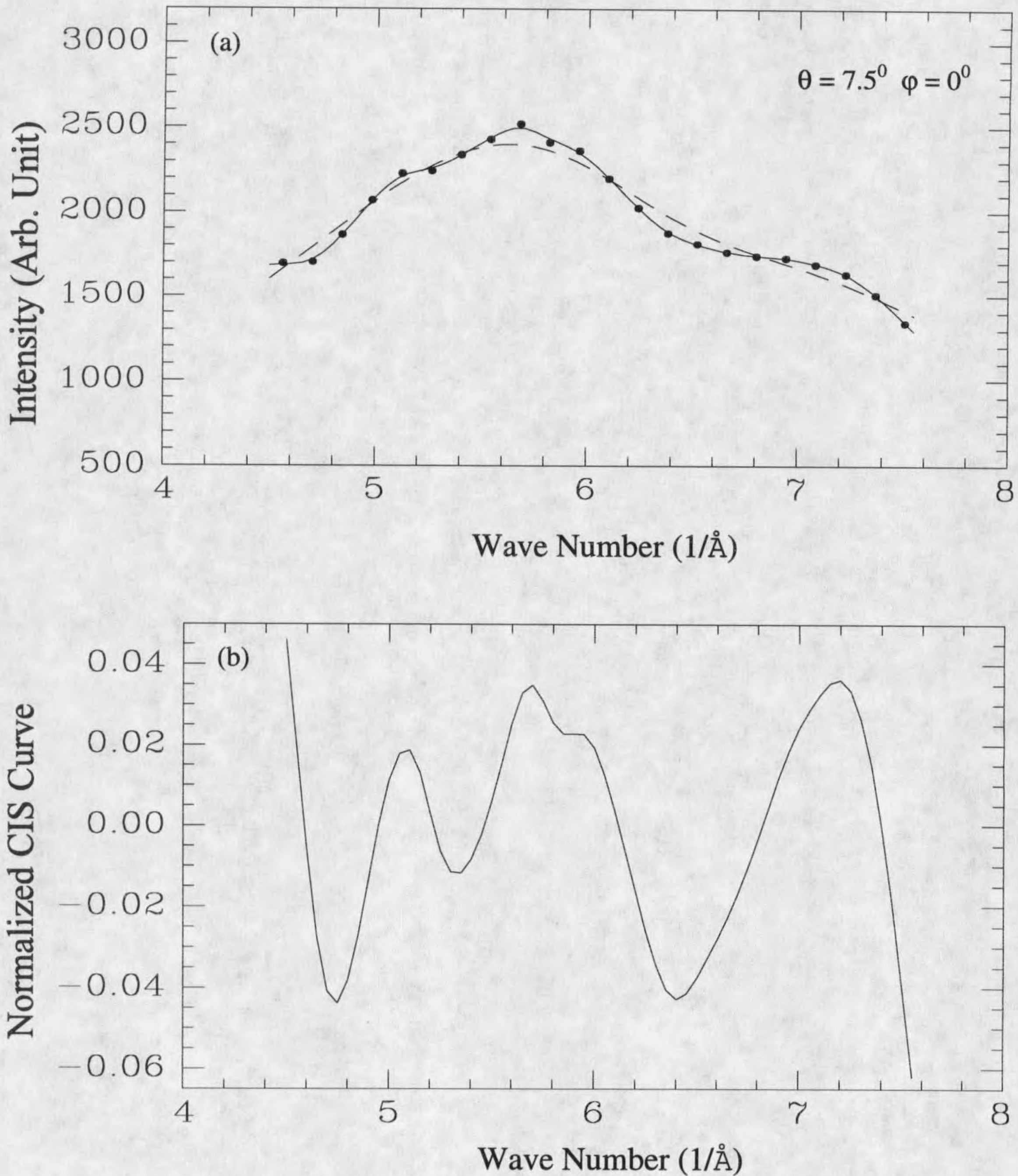

Fig. 28. (a) A CIS curve I(k) (dots and solid line) of Ga 3d and its non-diffractive background curve $I_0(k)$ (dashed line) for Ga/Ge(111)-1x1; (b) its normalized CIS curve $\chi(k)$.

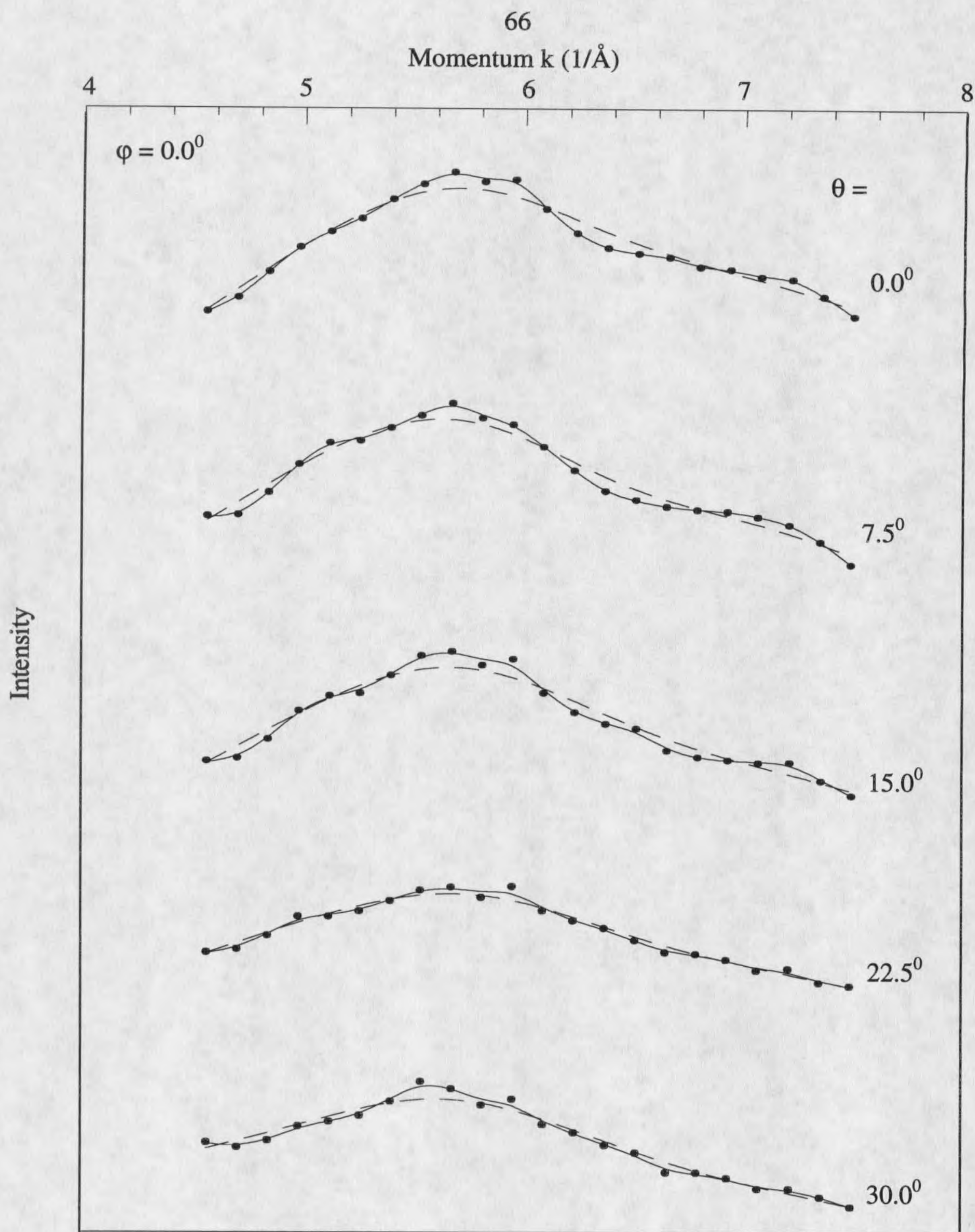

Fig. 29. Some CIS I(k) curves (dots and solid lines) from the Ga 3d core level and their non-diffractive background $I_0(k)$ curves (dashed lines) for Ga/Ge(111)-1x1 sample.

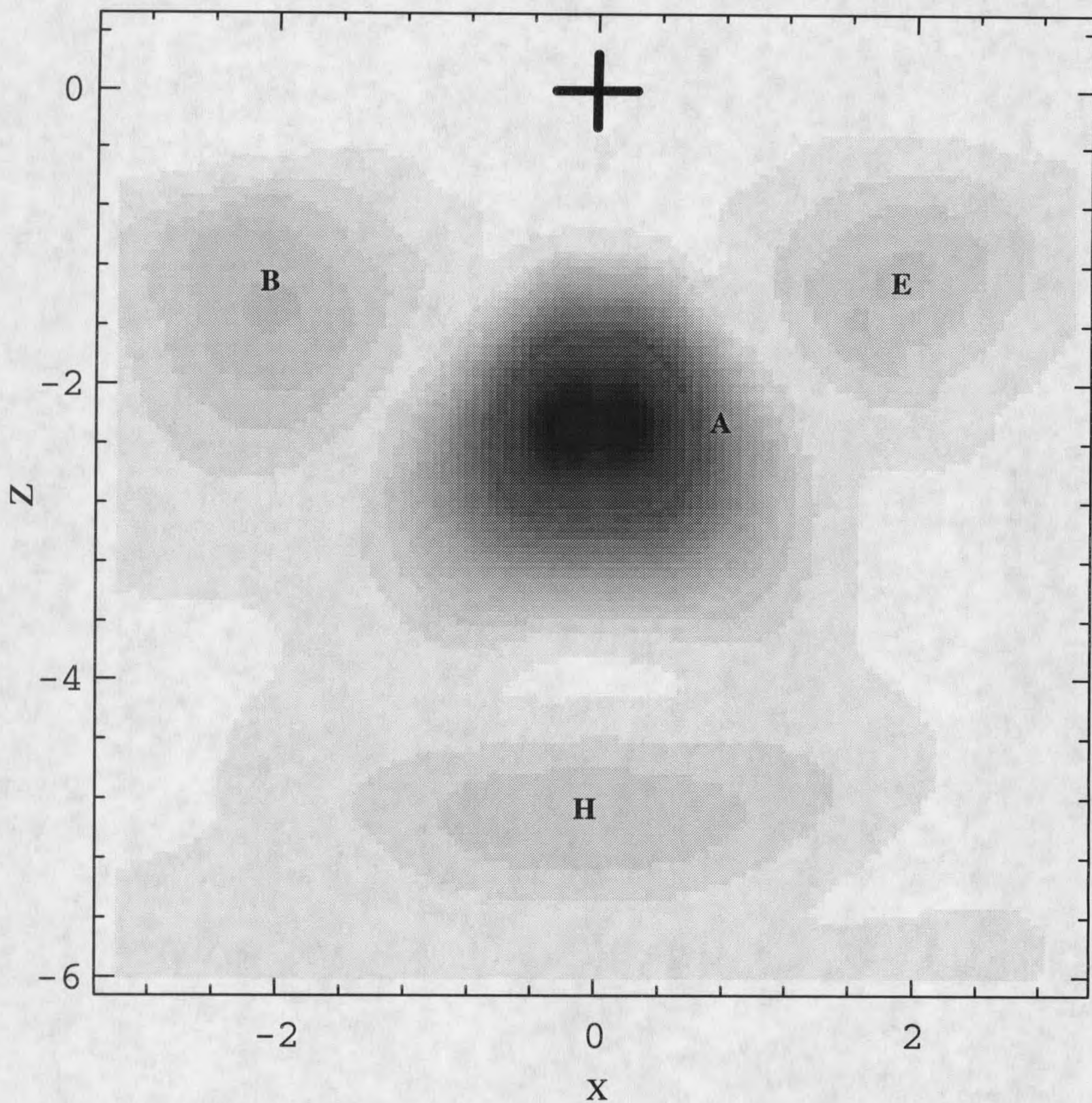

Fig. 30(a) X-Z vertical planar cut of the image function at y = 0 Å for Ga/Ge(111)-1x1 sample. The cross marks the emitter position. The intensity maxima represent the first-layer Ge atoms B and E, the second-layer Ge atom A and the third-layer Ge atom H. Coordinate units: Å.

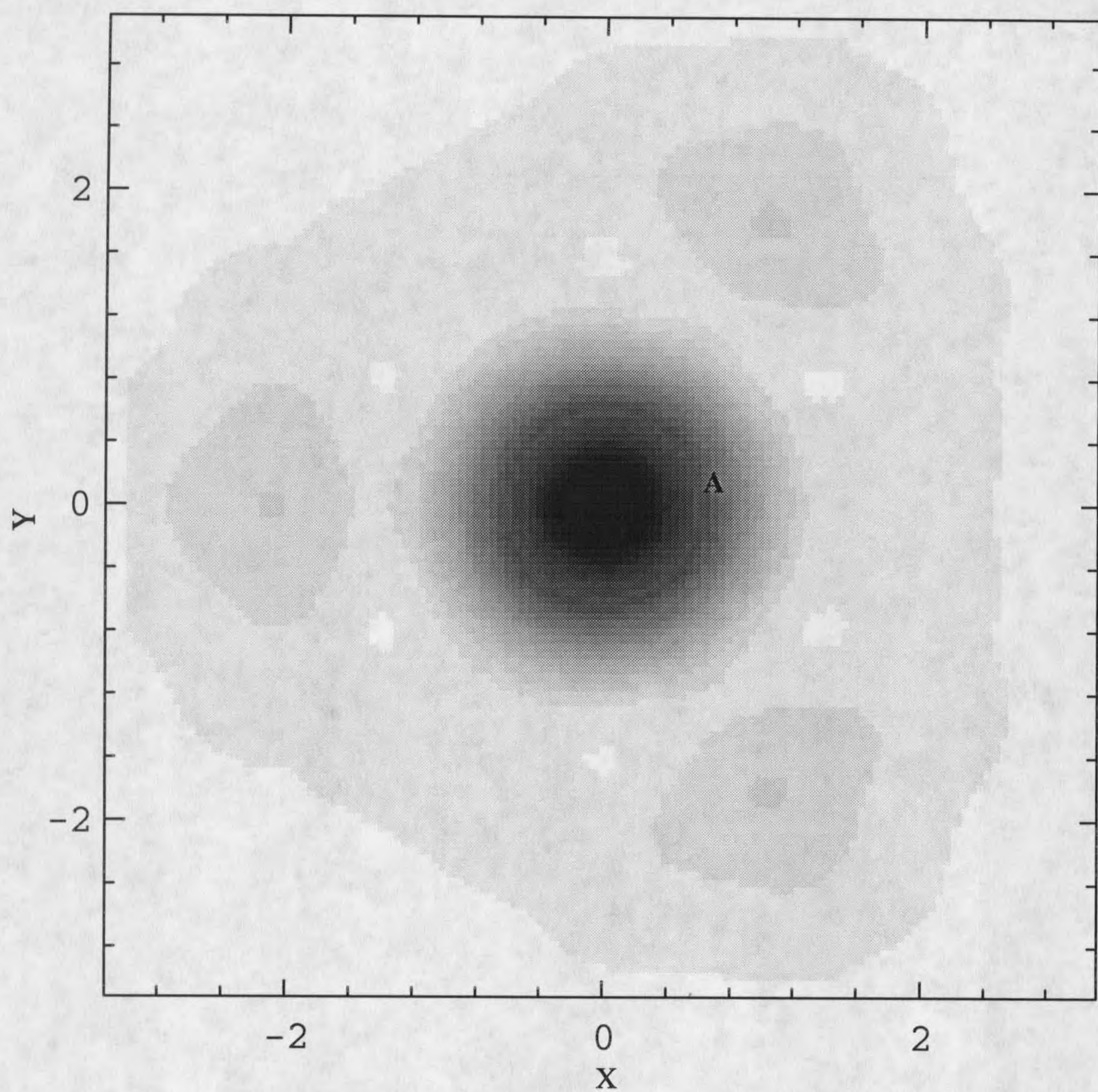

Fig. 30(b) X-Y horizontal planar cut passing through the second-layer Ge atom A at z = -2.3 Å of the image function for Ga/Ge(111)-1x1 sample. Coordinate units: Å.

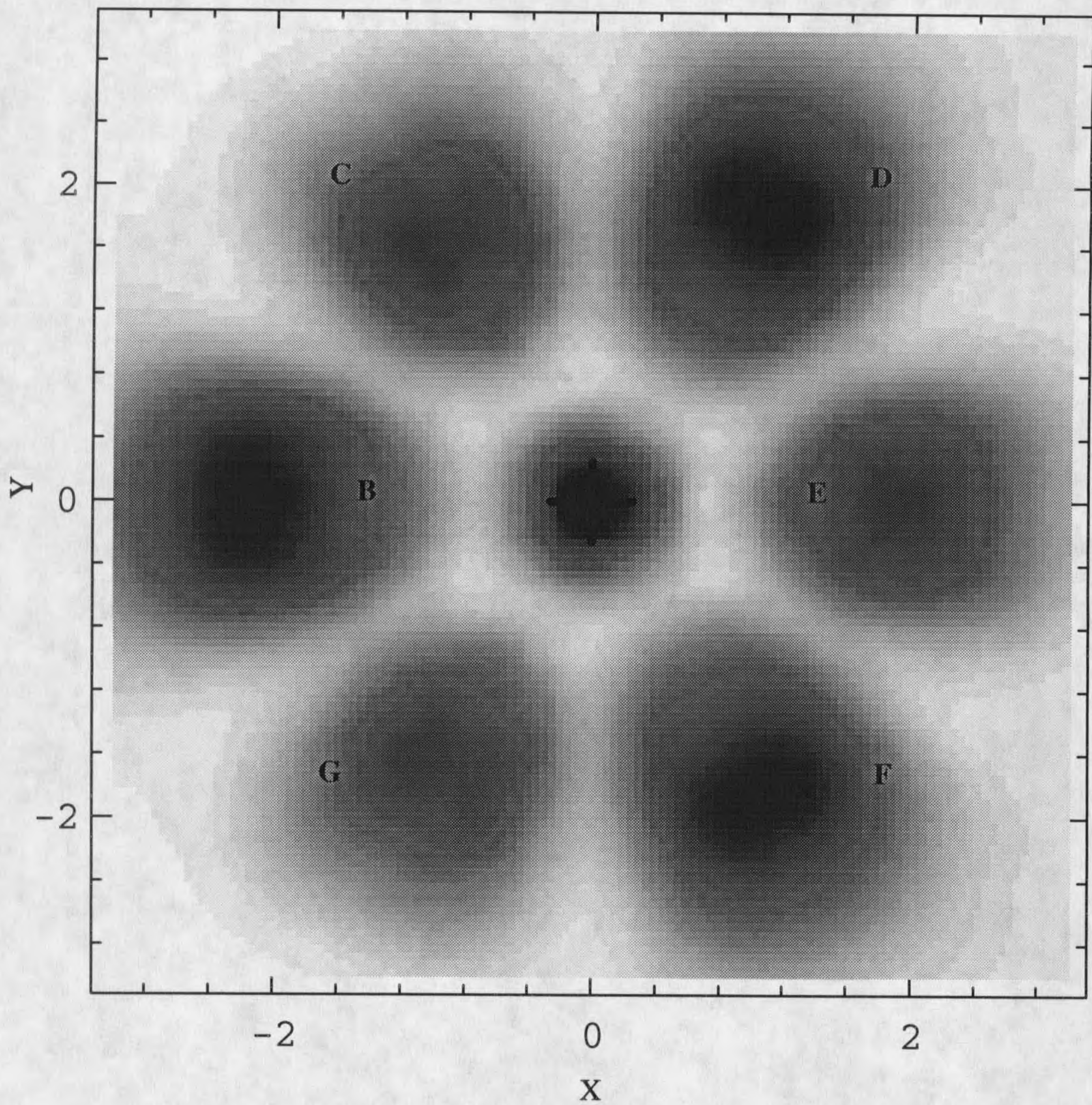

Fig. 30(c) X-Y horizontal planar cut of the image function for Ga/Ge(111)-1x1 at z = -1.2 Å. The intensity maxima labeled by B, C, D, E, F and G are due to the first-layer Ge atoms. The spot in the center is the tail of spot A. Coordinate units: Å.

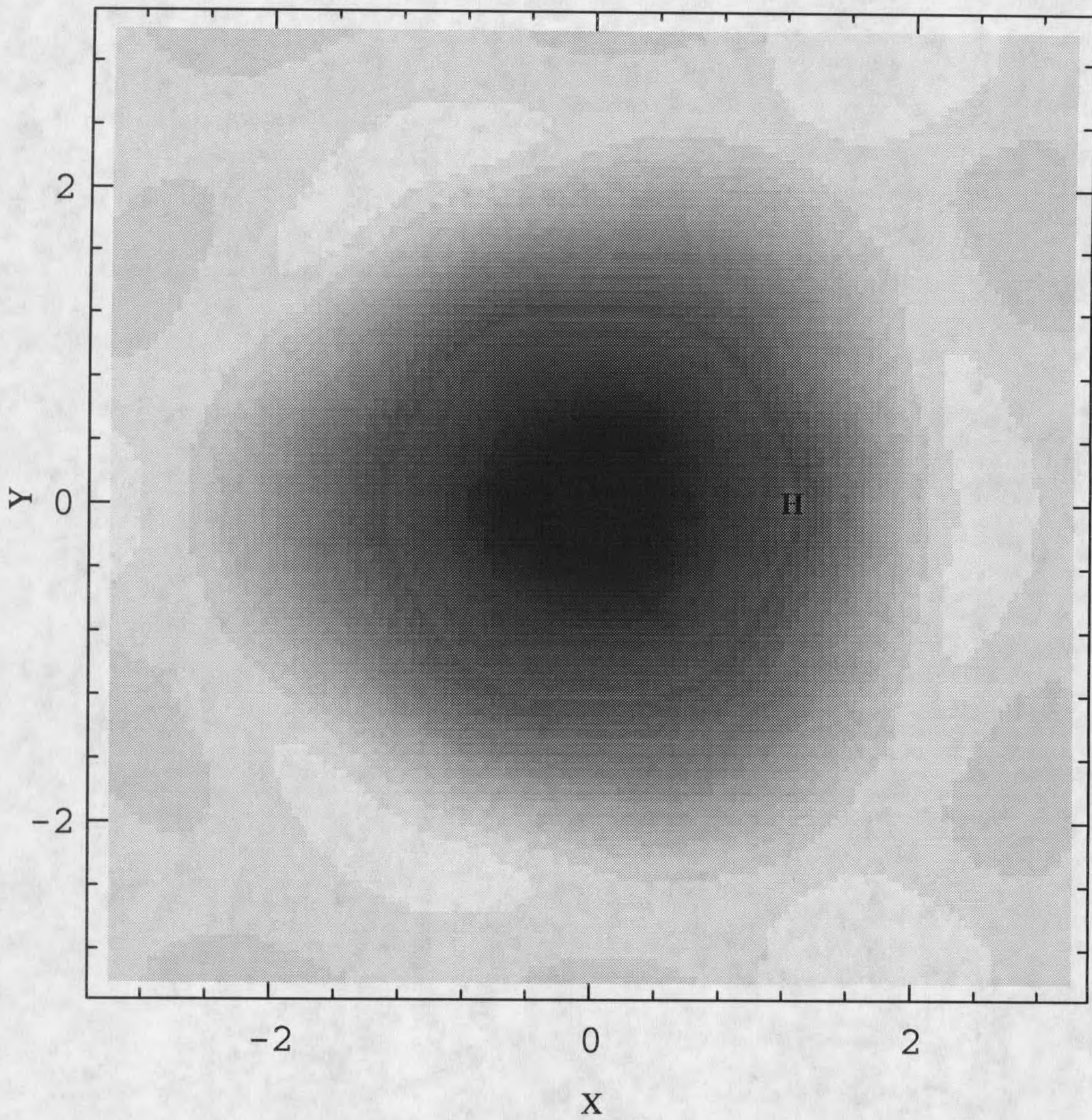

Fig. 30(d) X-Y horizontal planar cut passing through the third-layer Ge atom H at z = -4.9 Å of the image function for Ga/Ge(111)-1x1. The intensity of spot H is about 6% that of spot A. Coordinate units: Å.

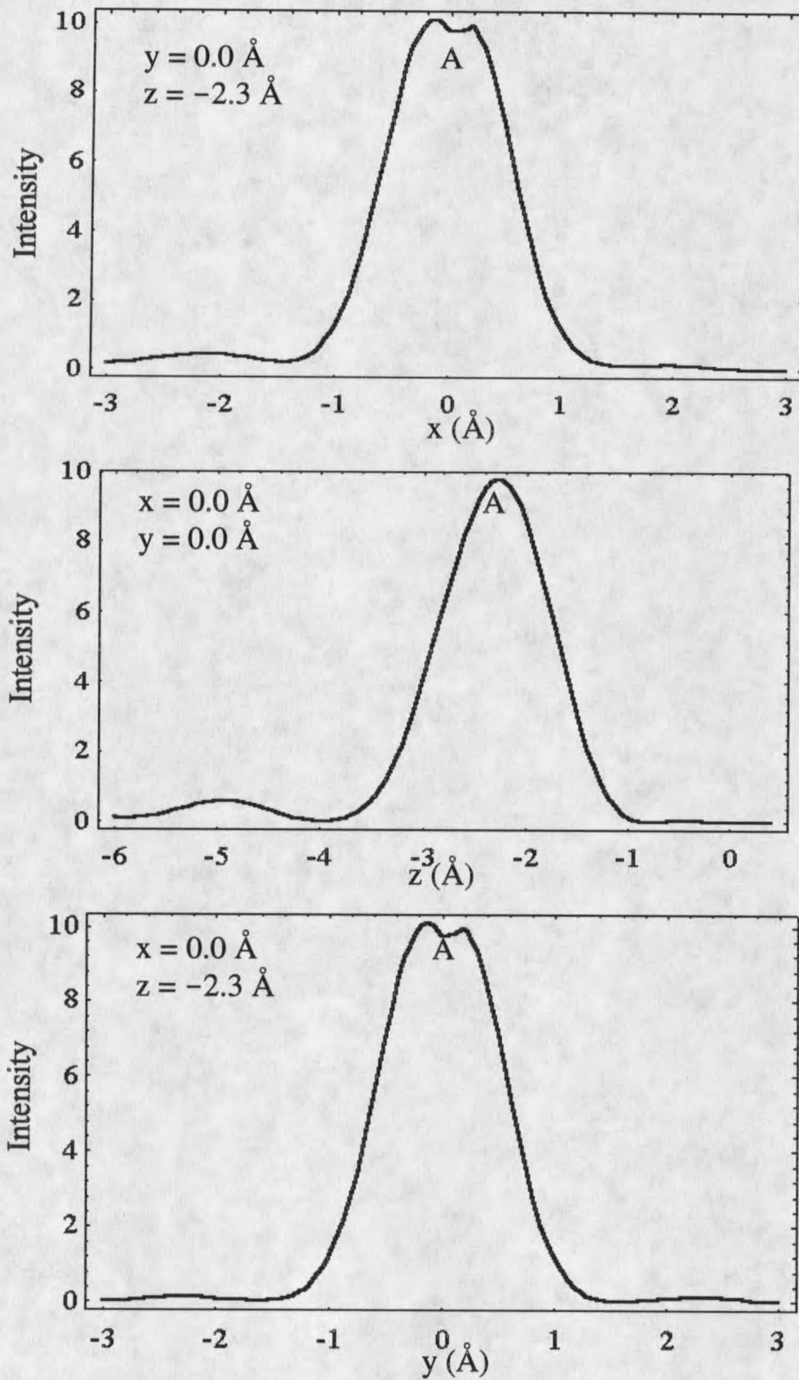

Fig. 31. Line scans passing through the spot A for Ga/Ge(111)-1x1 system. Intensity is in arbitrary units.

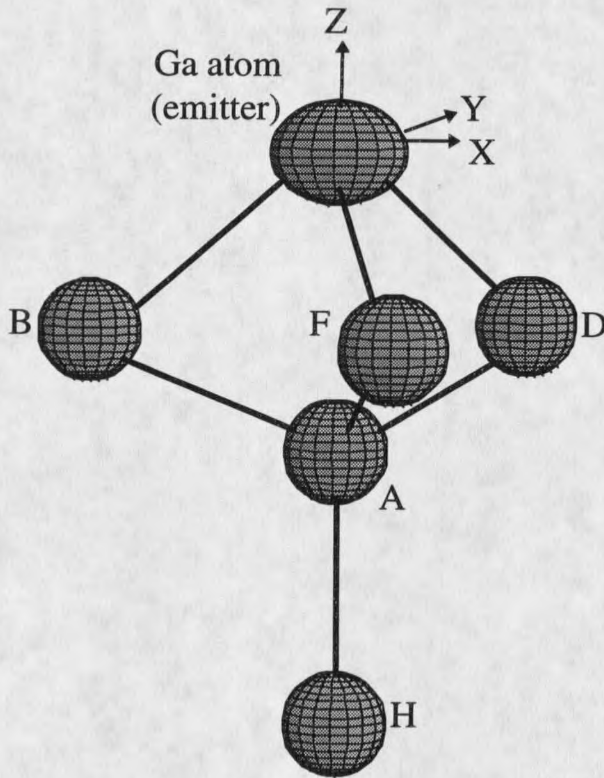

(a) T_4 site. A, B, D, F and H are Ge atoms.

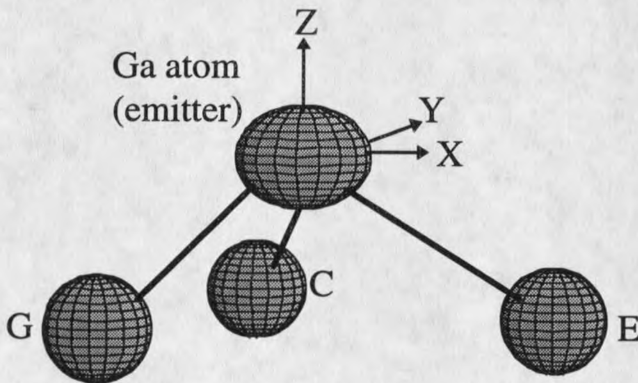

(b) H_3 site. C, E and G are Ge atoms.

Fig. 32. The structure model for Ga/Ge(111)-1x1. Ga atoms occupy both T_4 and H_3 sites.

Ge/Si(100)-2x1

The 4^0 vicinal cut Si(100) surface has the terraces separated by only biatomic steps and shows a single domain 2x1 LEED pattern, which is very similar to the vicinal Ge(100) surface (see Fig. 18(b)). After 0.5 monolayer Ge was deposited on the 4^0 vicinal cut of the Si(100)-2x1 substrate held at 450^0 C, the LEED pattern still remained as a 2x1 single domain with a slightly higher background. Figure 33 shows the wide-scan energy distribution curve at the photon energy of 150 eV. A total of 95 CIS's were collected from the Ge 3d core level. The measuring range was from 0^0 to 82.5^0 in polar angle with $\Delta\theta = 7.5^0$ and from 0^0 to 90^0 in azimuthal angle, i.e. one-fourth of the emission hemisphere, an irreducible symmetry element. Figure 14 depicts a typical CIS curve and its normalized curve. Figure 34 indicates the phase and amplitude of the CIS inversion at the position of the Si atom A vs. the polar angle. It can be seen that the half width of the small-cone is about 20^0.

Three images are shown in Fig. 36(a-c). The coordinates are chosen as follows (see Fig. 18(b) or Fig. 38): the X axis along the dimer-row direction of the substrate, the Y axis along the step-edge direction (i.e. the dimer direction), and the Z axis along the surface normal direction. Figure 36(a) is the horizontal planar cut of the image function at z = –1.2 Å. It indicates the four spots with the intensity maxima labeled by A, B, C, and D. As explained next, they are due to the first-layer Si atoms. The emitter (Ge atom) is at the origin. Figure 36(b) is the vertical planar cut of the image function at y = 0.5 Å, which passes through the spots A and B. Fig. 36(c) is the vertical planar cut through spots B and D at x = 1.8 Å. The

one-dimensional line scans for spot B are demonstrated in Fig. 37. The image distance between spot A and spot C, which is the same as the distance between spot B and spot D, is only 1 Å. This can not be real atomic separation since the separation between atoms is at least larger than 2 Å. This phenomenon is due to two non-equivalent emitter sites in this sample and will be explained later.

Apparently, the adsorption of Ge breaks the surface Si-Si dimers and forms Ge-Si bonds. At the same time, the Ge-Ge nearest neighbor image distance is 1.0 Å shorter than the inplane Si spacing, i.e. Ge dimers are formed and the dimer is along y direction (parallel to the step edge). From the Ge dimer direction determined by the images and the unchanged 2x1 LEED pattern after Ge adsorption, it is suggested that the chemisorbed Ge atoms replace the surface Si atoms from the terraces and then form Ge-Ge dimers. In this way, the surface will maintain the parallel dimer mode and the LEED will be still a single domain 2x1 pattern. This phenomenon has been reported by Tromp *et al* from the combined results of the studies by LEEM, STM and LEED techniques [41, 42, 73]. They suggested that the Ge submonolayer growth on Si(100) surface proceeds through a displacive adsorption process, whereby Ge dimers replace Si dimers on the terraces, allowing for more effective reduction of the Si-Ge misfit strain. The expelled Si atoms diffuse and adhere to the step edges.

Fig. 38 shows the surface reconstruction for the clean and Ge-adsorbed surfaces. One can see that the Ge atoms have two non-equivalent adsorption sites (Ge atom P represents one adsorption site and Ge atom Q represents another adsorption site shown in Fig. 39. These two sites are non-equivalent in photoelectron holography). Since the photoelectron holographic

image indicates an overall effect of the photoelectron diffraction contributed by all the emitters, including the equivalent and non-equivalent ones, the dimer structure can not be seen at first glance. Figure 39 demonstrates how to view the dimer structure from the images. Two non-equivalent Ge atoms (emitters) P and Q, will be viewed as the origin in the images. The Si atoms A and B can be seen from the emitter P, while the Si atoms C and D can be seen from the emitter Q. The superimposition of these two photoelectron diffraction patterns leads to the atomic images of Fig. 36 (a-c).

In conclusion, the Ge adsorption breaks the Si-Si dimers, remove the Si atoms from the terraces, and form Ge-Ge dimers. Table 4 lists the atomic positions in the images, while the comparison with the results from other groups is indicated in Table 5.

Table 4. Positions of the Si atoms in the images for the Ge/Si(100)-2x1 system. The atomic positions in the image could be off by the maximum of 0.2 Å. The coordinate unit: Å.

Si atom labeled by	Corresponding layer	Position
A	first	(−1.8, 0.5, −1.2)
B	first	(1.8, 0.5, −1.2)
C	first	(−1.8, −0.5, −1.2)
D	first	(1.8, −0.5, −1.2)

Table 5. Bond lengths obtained from the different groups for Ge/Si(100)-2x1 sample. In the calculation of the bond lengths from the image's atomic positions, it is assumed that in the first layer the Si atom separation is the bulk value (3.8 Å).

	Ge-Ge dimer's length (Å)	Ge-Si bond length (Å)
This work	2.8	2.2
Trans. ion channeling [43]	2.6	N/A
X-ray standing wave [44]	2.6	N/A

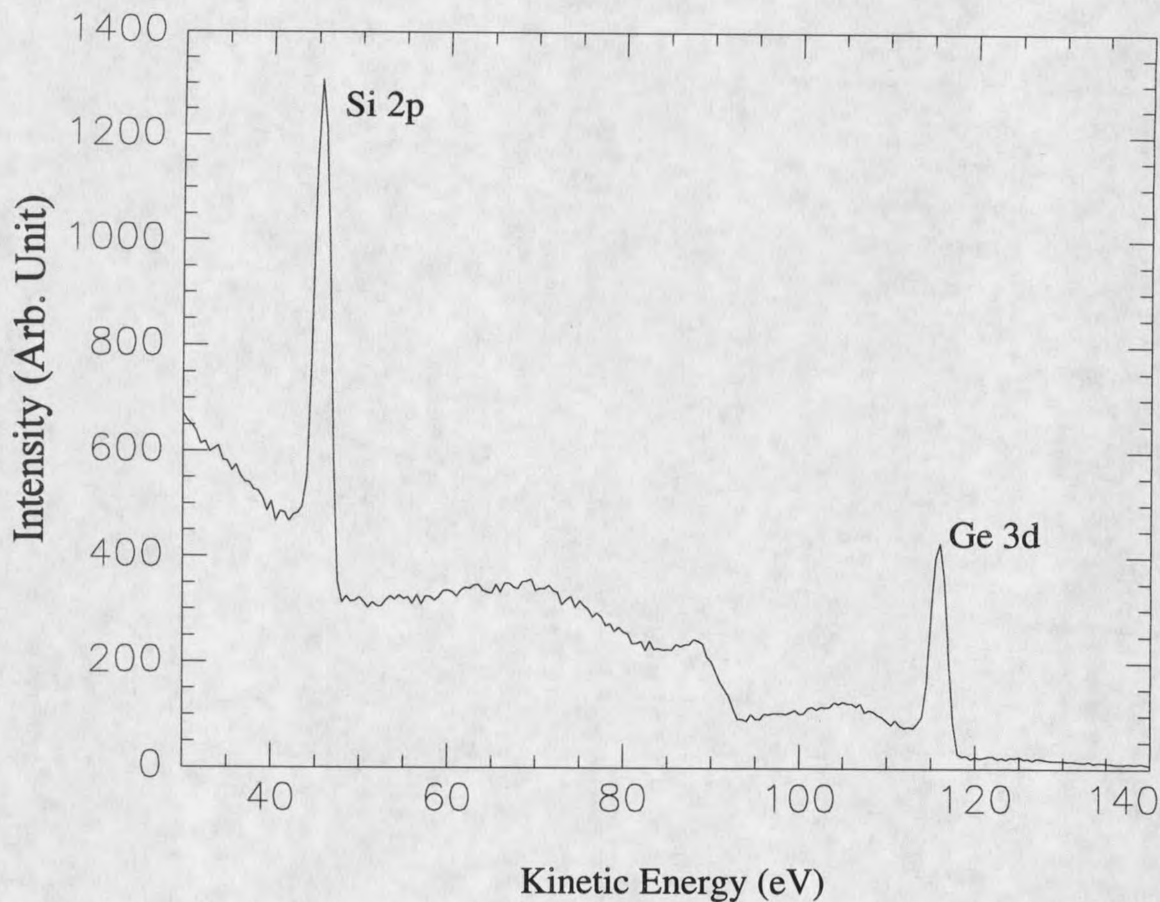

Fig. 33. Wide-scan energy distribution curve at the photon energy of 150 eV for the Ge/Si(100)-2x1 sample. It was taken at $\theta = 82.5^0$ and $\varphi = 90^0$.

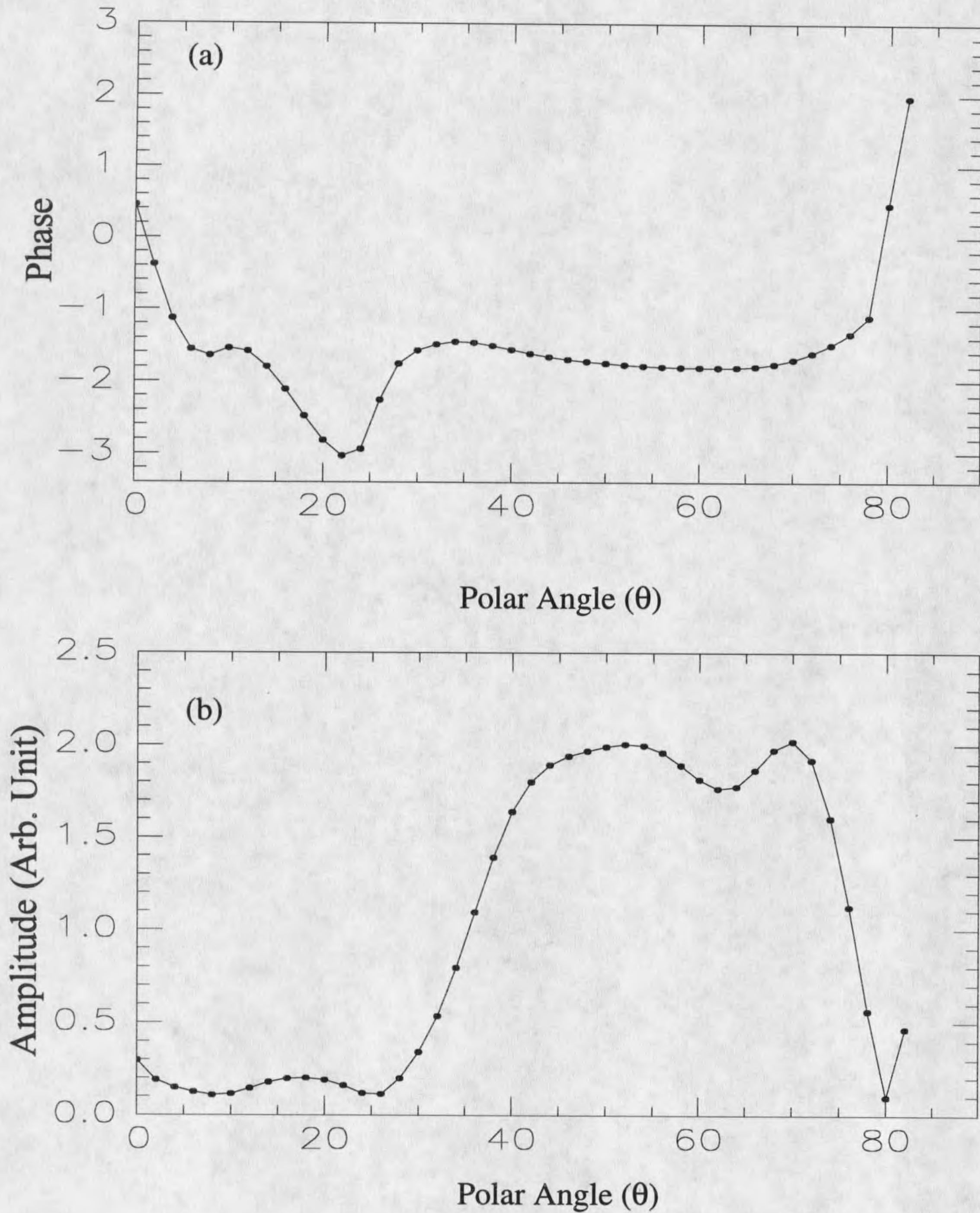

Fig. 34. (a) Phase and (b) amplitude of the CIS inversion vs. polar angle at the position of the Si atom A for Ge/Si(100)-2x1 sample. The azimuthal angle φ is 345^0.

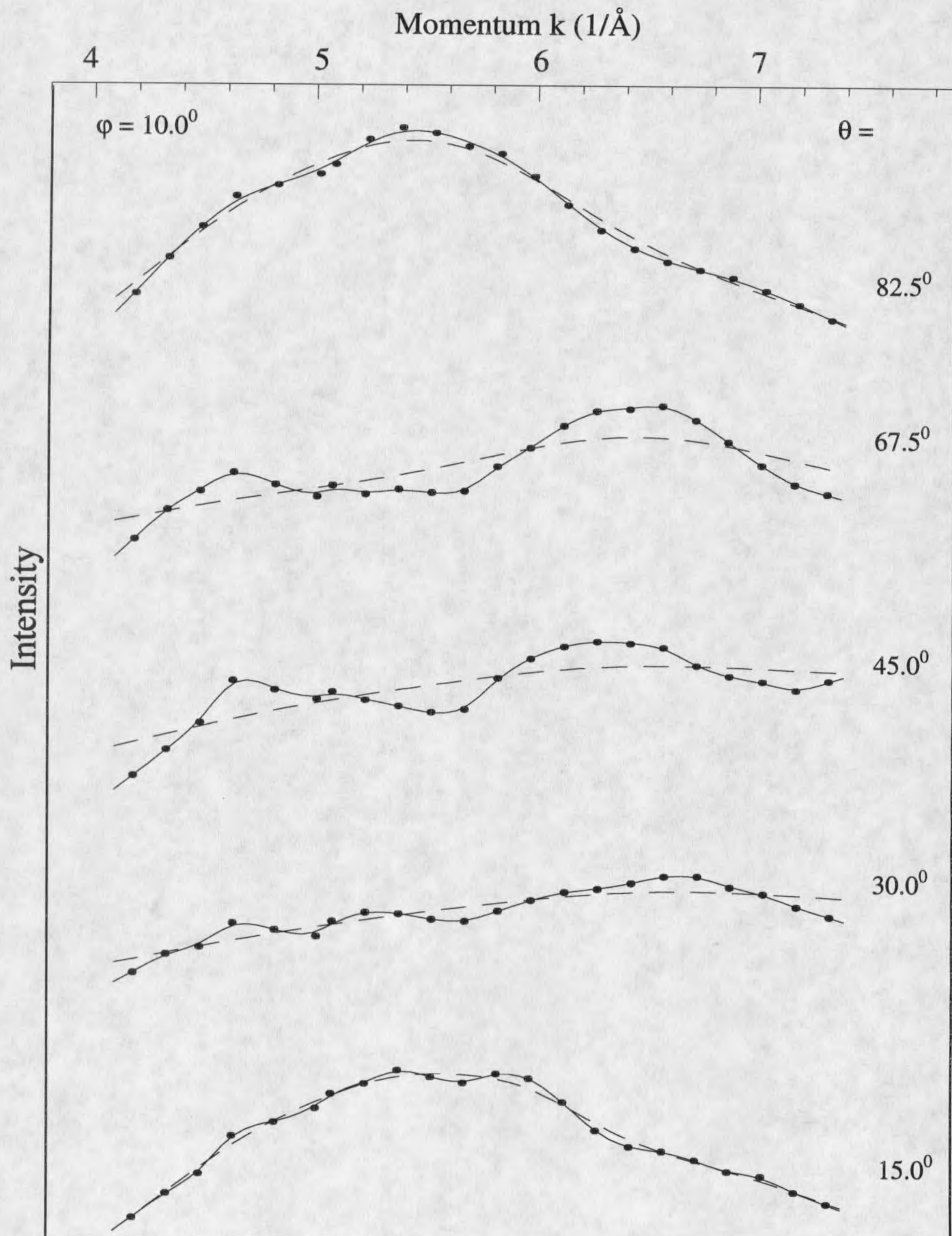

Fig. 35. Some CIS I(k) curves (dots and solid lines) from the Ge 3d core level and their non-diffractive background $I_0(k)$ curves (dashed curves) for Ge/Si(100)-2x1 sample.

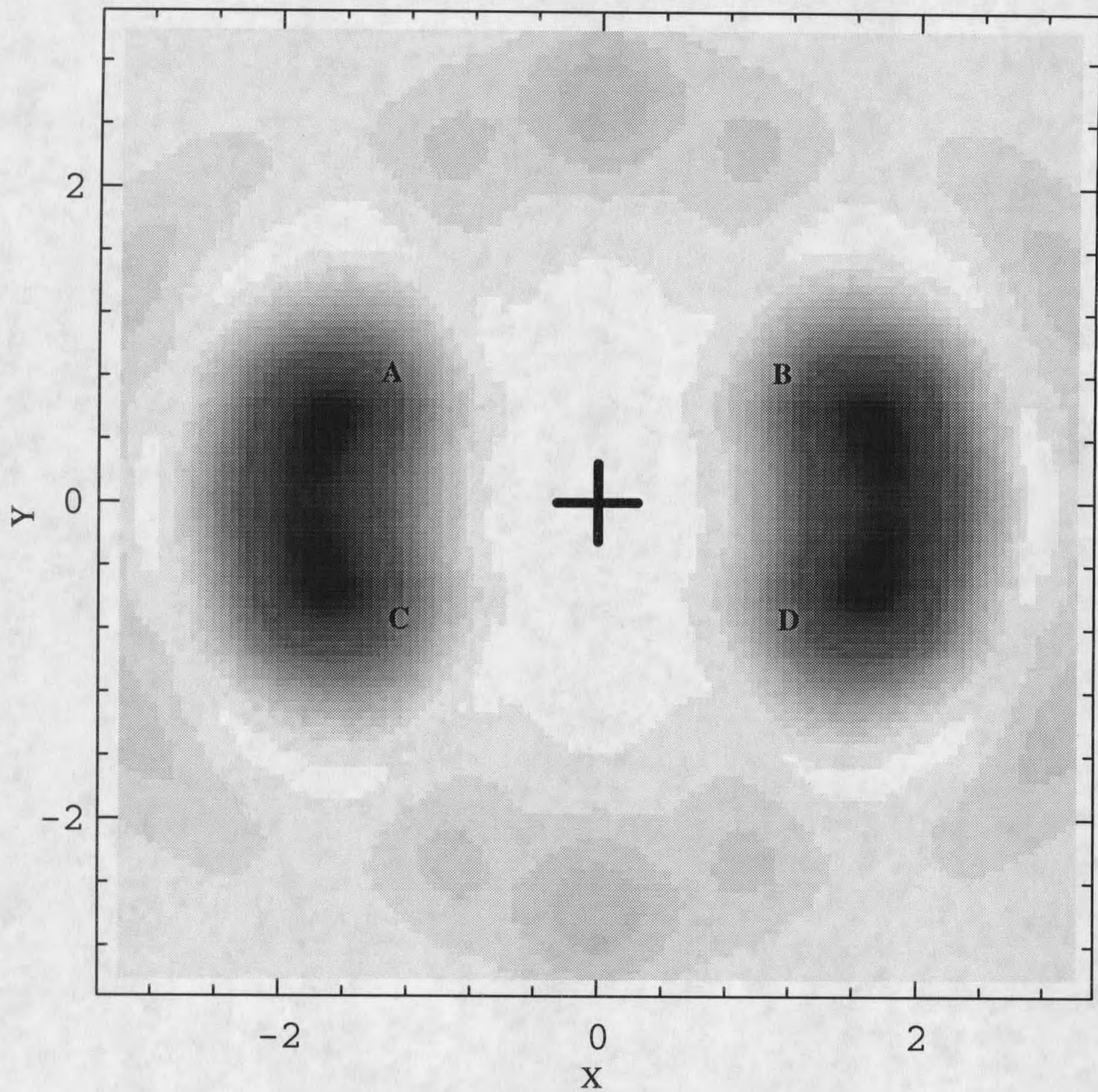

Fig. 36(a) X-Y horizontal planar cut of the image function at z = -1.2 Å for Ge/Si(100)-2x1. The four spots with maximum intensities labeled by A, B, C and D are due to the first-layer Si atoms. Coordinate units: Å.

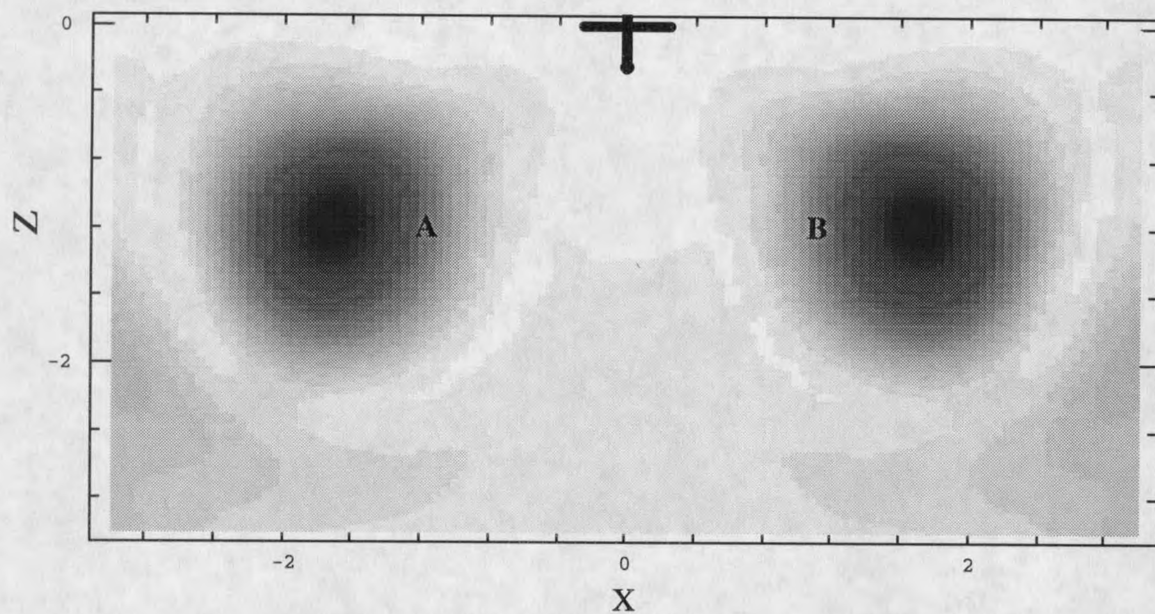

Fig. 36(b) X-Z vertical planar cut of the image function at y = 0.5 Å for Ge/Si(100)-2x1. The two spots with intensity maxima labeled by A and B are due to the first-layer Si atoms. Coordinate units: Å.

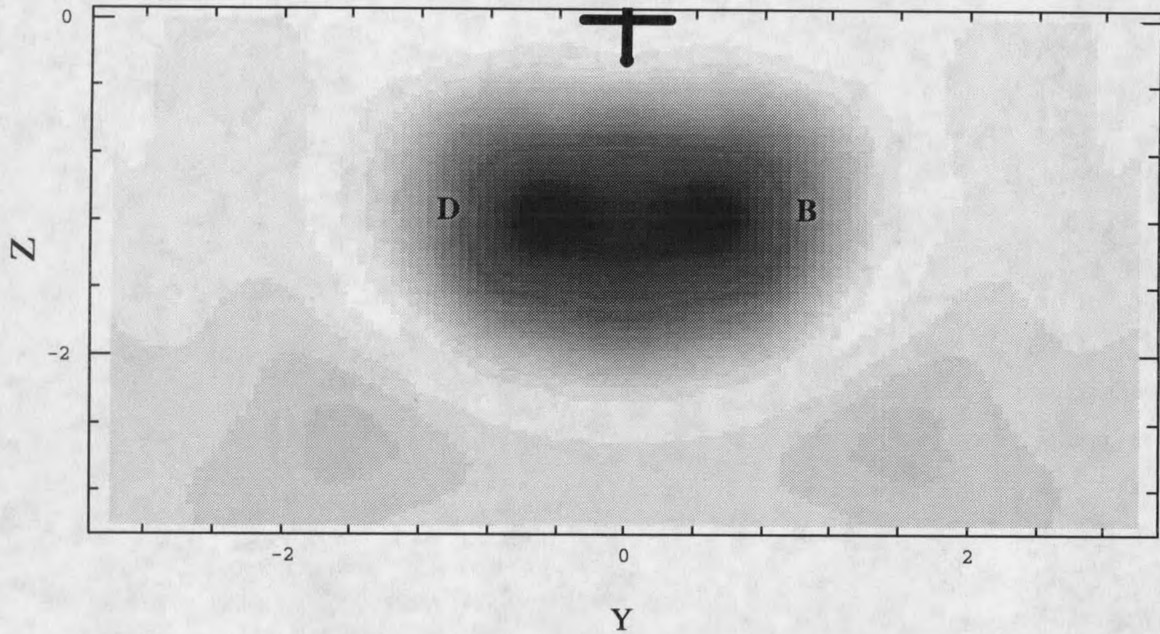

Fig. 36(c) Y-Z vertical planar cut of the image function at x = 1.8 Å for Ge/Si(100)-2x1. The two spots with highest intensities labeled by B and D are due to the first-layer Si atoms. Coordinate units: Å.

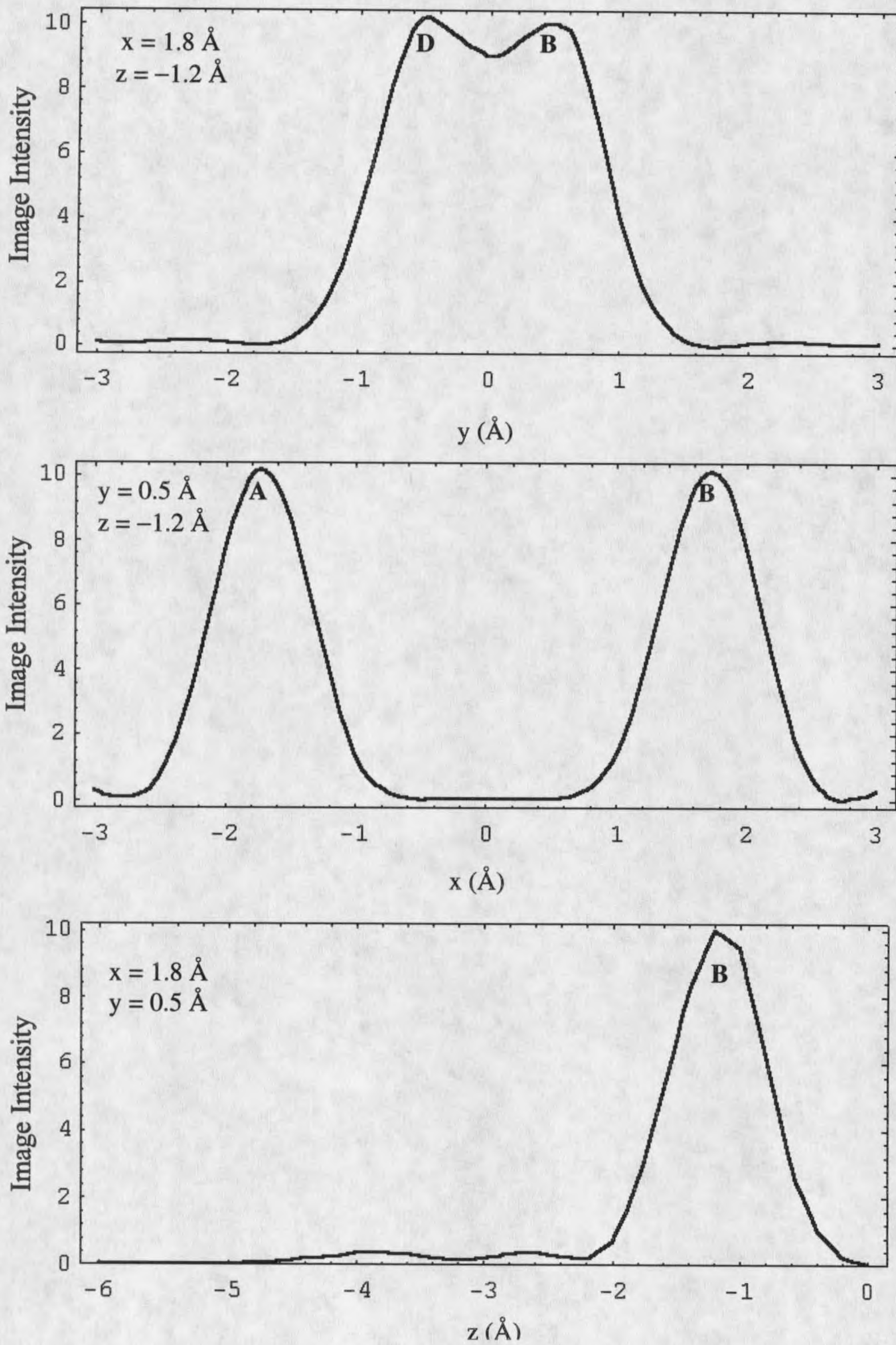

Fig. 37. The line scans passing through the spot B of the image for Ge/Si(100)-2x1 sample.

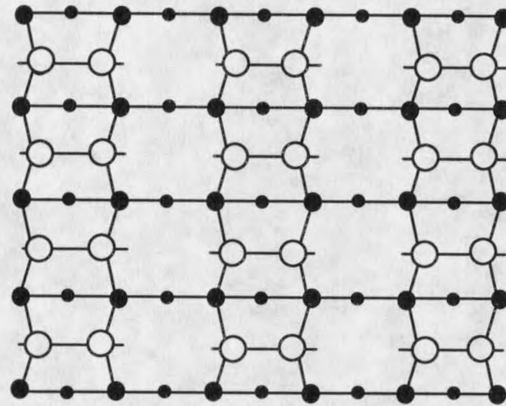

(a)

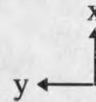

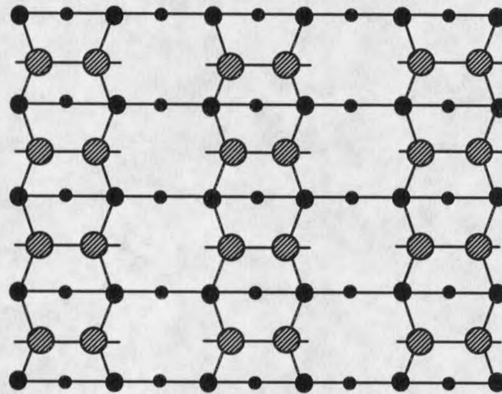

(b)

O—O Si-Si dimer ●—● Ge-Ge dimer ● second-layer Si atom for (a) or first-layer Si atom for (b) • third-layer Si atom for (a) or second-layer Si atom for (b)

Fig. 38. Diagram of the surface reconstruction for (a) Si(100)-2x1, (b) Ge/Si(100)-2x1. Si dimers are replaced by Ge dimers due to the Ge adsorption. Short bars are dangling bonds.

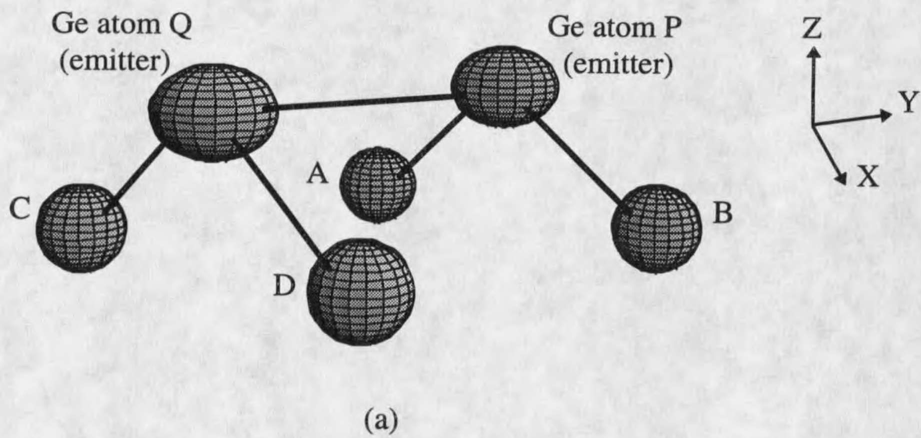

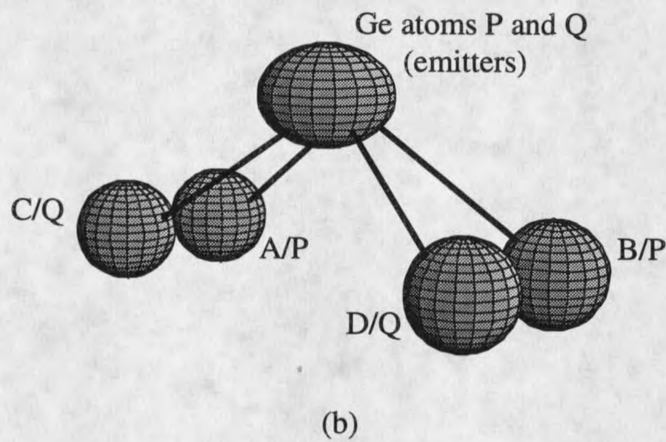

Fig. 39. (a) Three-dimensional structure model for Ge/Si(100)-2x1 sample. A Ge-Ge dimer in y direction is indicated on the Si displaced surface. (b) The holographic pattern of (a) by putting two emitters together at the origin.

CHAPTER 6

EXPERIMENTAL RESULTS AND DISCUSSION OF THE STUDIES OF MBE-GROWN GaAs(111) SURFACES

Introduction

GaAs(111) surfaces are terminated by either Ga atoms (GaAs(111)A) or As atoms (GaAs(111)B). The MBE-grown GaAs(111)A surfaces have shown the 2x2 reconstruction [13,35], while the MBE-grown GaAs(111)B surfaces exhibit three different surface reconstructions. These three surface phases (namely 1x1, 2x2 and $\sqrt{19}$x$\sqrt{19}$) depend on the growth temperatures and the incident As flux density [13, 15, 35]. In this work, only GaAs(111)B 2x2 structure has been investigated.

Since Si is one of group IV elements, the Si-dopant can be either a donor or acceptor. It is well known that Si acts as a donor for the MBE growth of GaAs on a (100)-oriented GaAs substrate [45-46]. The Si-doped GaAs(111)B epilayers also exhibit n-type conductivity. However, all of the MBE-grown Si-doped GaAs(111)A structures are p-type semiconductors [13,47]. Therefore, one can study the hole plasmon excitation on the GaAs(111)A surface and the electron plasmon excitation on the GaAs(111)B surface. The system in the CRISS lab is

set up so that one can perform the surface investigation after MBE growth without exposing the surface to air. The effects of hydrogen chemisorption are also presented in this chapter.

XPS uses the characteristic X-ray M_ζ emission of Zr at 151.4 eV photon energy to excite the core level electrons of the sample. Just as in UPS, the excited electrons have a specific kinetic energy determined by the photon energy and the core level binding energy. The main utility of XPS is that location of the line produced in the XPS spectrum can be used for element identification. while the intensity of the line reflects the relative concentration of the element measured. The latter property is used in this experiment to monitor the surface stoichiometry. UPS uses the narrow characteristic line of the He gas discharge glow to study the valence band structures or the Fermi-level. The shift of the VBM (valence band maximum) position reveals the band bending near the semiconductor surface.

The principle of HREELS involves the dipole scattering mechanism. There is an interaction between the incident electron and the dipole moment, caused by charge density fluctuations in the solid or by vibrations of adsorbates. The primary electron (e^-) has energy E_0 and momentum $\mathbf{k}_i$. Due to the dipole field, the primary electron is scattered into a final state $\mathbf{k}_f$ with energy E_f along the specular reflected direction. In the dielectric theory, let $\varepsilon = \varepsilon_1 + i\varepsilon_2$ be the dielectric function of the solid, the energy loss due to the interaction of the electric field with the medium is proportional to [59]

$$\text{Loss function} \propto \frac{\varepsilon_2}{|\varepsilon+1|^2} = \mathrm{Im}\left[\frac{-1}{\varepsilon+1}\right] \tag{6.1}$$

For the Drude model,

$$\varepsilon = \varepsilon_\infty + \chi_{\text{phonon}} - \frac{\omega_{\text{pl}}^2}{\omega^2 + i\omega\Gamma} \tag{6.2}$$

where χ_{phonon} is the optical phonon (Fuchs-Kliewer phonon) contribution to the dielectric function, ε_∞ is the background dielectric constant, and Γ is the damping term related to the mobility. The quantity ω_{pl} is the plasmon energy, which is

$$\omega_{pl} = 4\pi ne^2/m^* \tag{6.3}$$

for Drude model, where m^* is the effective mass of the carriers, and n is the carrier concentration. The information obtained from the loss spectrum is closely related to long-range correlations of the medium such as the collective excitations of plasmon and photon, as well as the stretching vibration between hydrogen atom and substrate atom in case of hydrogen adsorbed on the surface. Further details on the basics of HREELS are given in the book by Ibach [59].

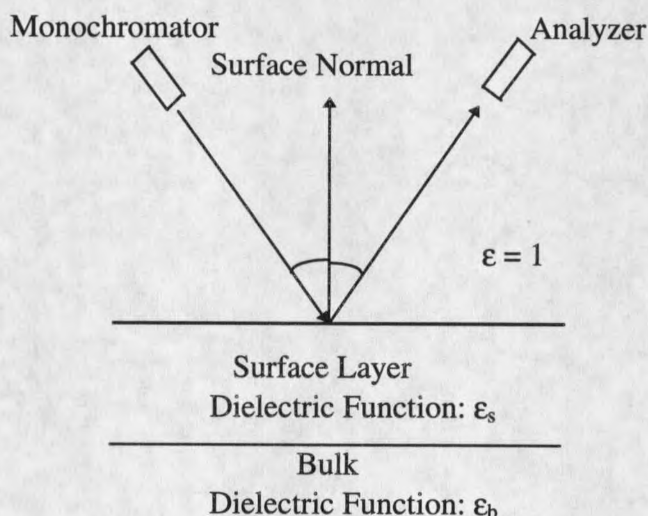

Fig. 40. HREELS phenomenon

MBE-grown GaAs(111)A

LEED, XPS and UPS studies

Chemisorption of hydrogen atoms on the semiconductor surfaces may induce changes of surface reconstructions, chemical composition (stoichiometry), as well as the band bending and work function. The information on both the clean surface and the hydrogen absorbed surfaces can be obtained by examining the LEED patterns, XPS and UPS spectra.

The changes in the surface reconstruction during atomic hydrogen exposure were monitored by LEED. For a small amount of hydrogen adsorption, the 2x2 LEED pattern was not noticeably changed, with only a slightly decrease in the intensities of fractional spots. For a hydrogen exposure in the 50 – 200 L range, the fractional spots became diffuse and faint and the background became higher without altering the overall structure. For the exposure beyond that range, the surface showed a 1x1 LEED pattern with a high background, which may suggest that a disordered surface was developed. This will be discussed further by examining the HREELS results and the vacancy buckling model of GaAs(111)A surface [48, 49].

Figure 41 shows the Ga 3d and As 3d core levels of XPS (Zr-M_ξ hν = 151.4 eV) spectra from the clean and hydrogen-adsorbed surfaces (The curves are normalized to emphasize changes in shape). The hydrogen-induced Ga 3d and As 3d shift to the lower kinetic energies, while the shift of As 3d is larger than that of Ga 3d. Another observable feature is that the As 3d line is most strongly affected by the hydrogen chemisorption, with

extra weight appearing on the low kinetic-energy side for the high hydrogen coverage. Similar phenomena have also been reported on the GaAs(100) and GaAs(111)B surfaces [50]. Each core level is fitted with Gaussian function plus linear background. Then the peak area is used as the intensity to examine the surface stoichiometry.

$$\frac{N_{Ga}}{N_{As}} = \frac{I_{Ga}}{I_{As}} \times \frac{\sigma_{As}}{\sigma_{Ga}} \tag{6.4}$$

where N_{Ga} is the number of Ga atoms on the surface, I_{Ga} is the integrated intensity (i.e. peak area) of Ga 3d peak, and σ_{Ga} is the photoionization cross section of Ga 3d at photon energy of a 151.4 eV. The same notations hold for the As atom. The photoionization cross section σ can be obtained from the theoretic calculation by J. Yeh, *etc* [56]. The ratio $\frac{N_{Ga}}{N_{As}}$ is 0.74 (very close to 3/4) for the clean surface, in agreement with the vacancy buckling model of GaAs(111)A surface [48, 49].

The vacancy buckling model (see Fig. 42) claims that there are an equal number of Ga and As atoms on the surface, but the 1/4 layer of the tetrahedrally bonded As atoms are only 0.2 Å below the surface. The As atoms on this layer should be also counted; then there will be three Ga atoms for every four As atoms. No significant variation in $\frac{N_{Ga}}{N_{As}}$ was observed during the hydrogen adsorption up to 1000 L, it indicates that the surface stoichiometry is not substantially changed by the hydrogen exposure.

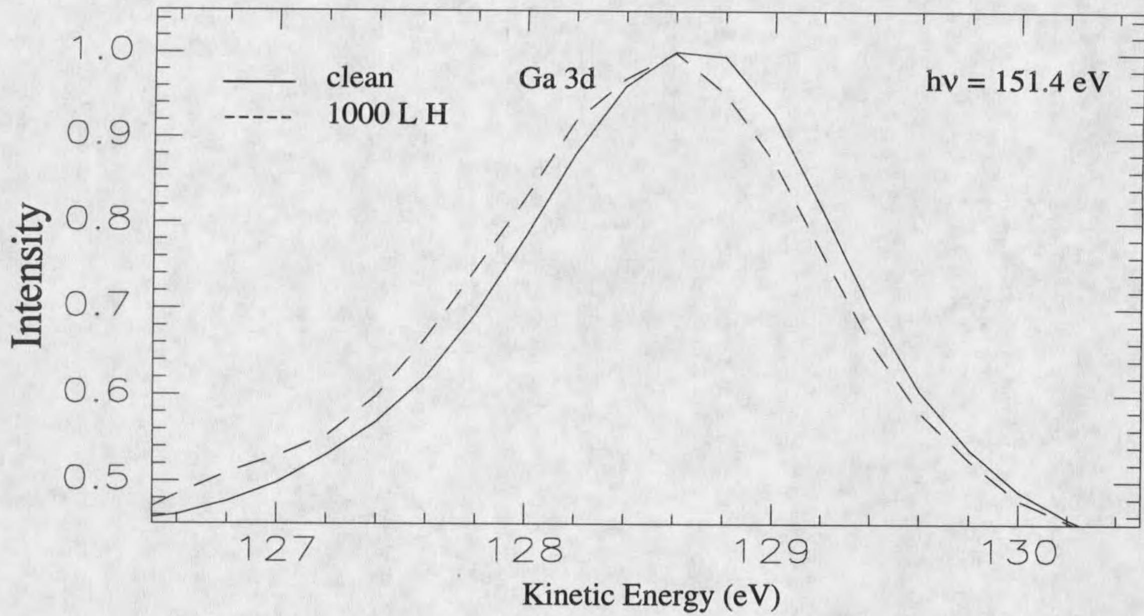

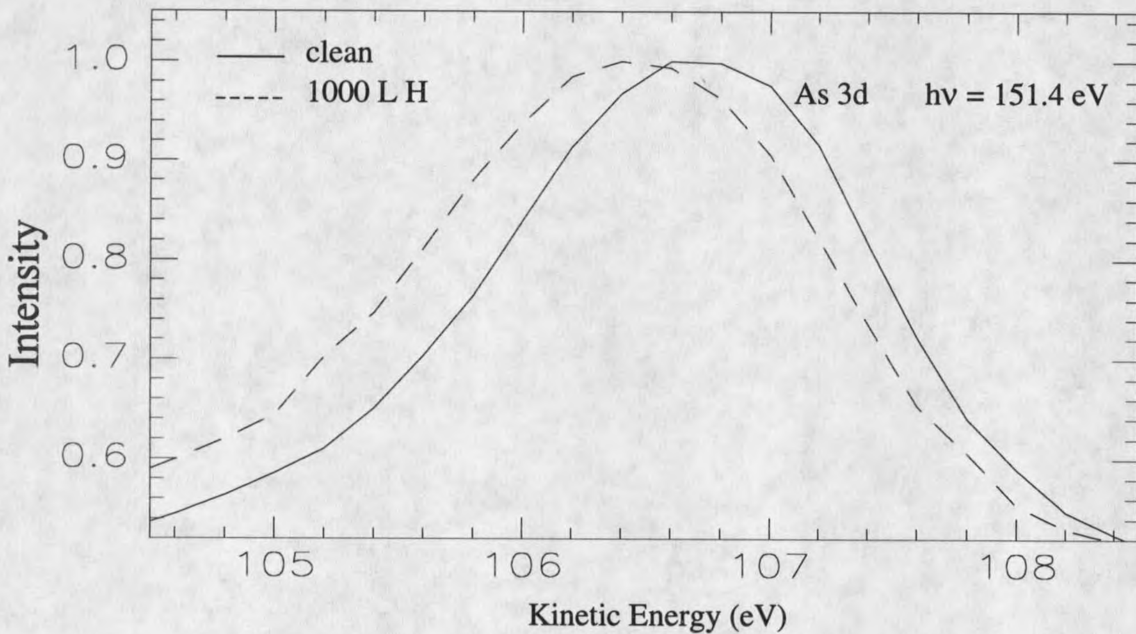

Fig. 41. The Ga 3d and As 3d line shapes for the GaAs(111)A surface. The intensities are normalized to emphasize changes in shape.

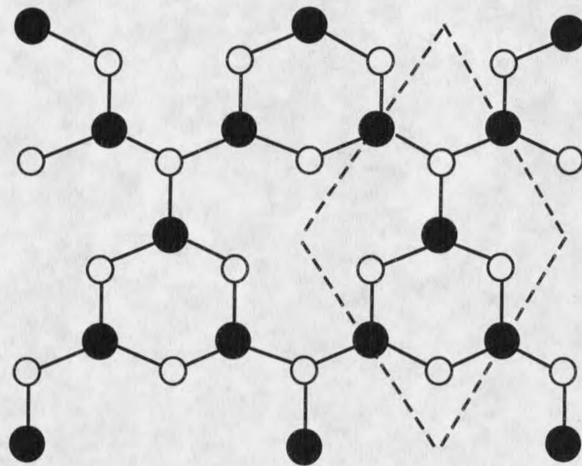

(a)

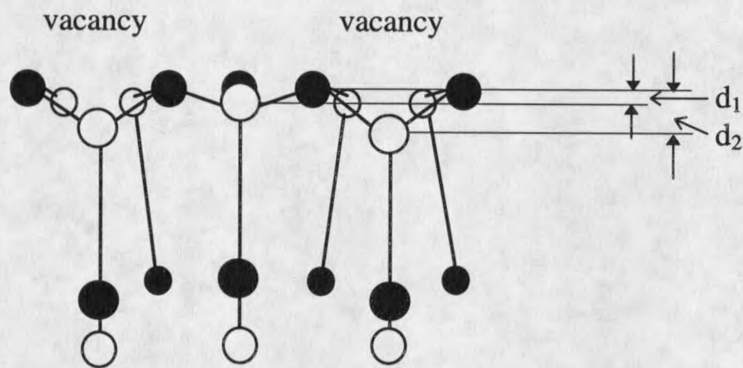

(b)

As Ga

Fig. 42. (a) Top schematic view; (b) side view of the (2x2) vacancy buckling model for GaAs(111)A. The dashed line represents one unit cell. d_1 = 0.07 Å, d_2 = 0.2 Å [48, 49].

The chemical shifts of Ga 3d and As 3d core levels due to the hydrogen adsorption suggest that the hydrogen atoms interact strongly with the GaAs(111)A surface, and form both Ga-H and As-H bonds in a way similar to that observed on the GaAs(110) surface [51]. The observed asymmetric broadening of As 3d line results from the unsaturated surface As atoms which will be discussed in the HREELS section.

By measuring the valence-band maximum (VBM) of the surface and the Fermi level (E_F) of the system from the UPS spectra (by He I, $h\nu = 21.2$ eV), we can obtain the value of the band bending on the clean surface. That is the difference between the bulk and surface VBM. The band bending on the clean surface was found to be 0.4 eV, probably caused by surface defects and surface states. Provided there is no emission from surface states within the band gap, the work function Φ_w of the surface

$$\Phi_w = h\nu - W_E \tag{6.4}$$

equals to the difference between the photon energy $h\nu$ and the width W_E of EDC spectrum (i.e. W_E is the energy range from the cutoff to the Fermi-energy). The work function Φ_w on the clean GaAs(111)A surface was determined to be 4.7 eV.

Analysis of the UPS spectra for a series of hydrogen exposures revealed a shift in the position of the VBM with hydrogen coverage (up to 100L H_2). It shifted down about 0.3 eV, caused by the charge transfer. The total band bending after hydrogen adsorption was 0.7 eV(shown in Fig. 43). When the surface is exposed to atomic hydrogen, the chemisorption induced defect states [51] or hydrogen related surface states can be in the gap. These acceptor-

type states are above the bulk Fermi-level. Thus the conduction band holes will fill these states, which leads to the shift of the surface VBM.

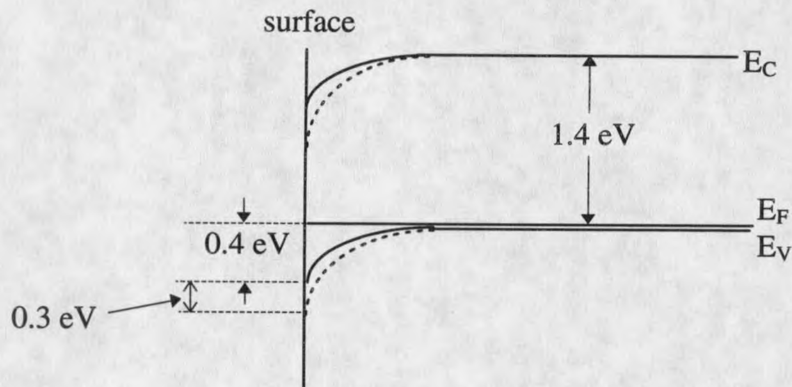

Fig. 43. Energy-level diagram for the p-type GaAs(111)A surface. E_C: energy-level of conduction-band minimum; E_F: the Fermi level; E_v: energy-level of valance-band maximum. The solid line presents the band-bending of the clean surface, the dashed line presents the band-bending of the hydrogen adsorbed surface.

HREELS studies

The HREELS measurements were performed on the MBE-grown p-type GaAs(111)A surface at room temperature. Figure 44 depicts the spectra of the clean surface taken at several different primary beam energies. The energy resolution is about 9 meV, as measured by the full width at half maximum of the elastic peak. One can observe a strong well-defined Fuchs-Kliewer optical phonon [59, 60] at 35 meV and the broad strong tail due to the hole-plasmon. Unlike the n-type GaAs sample, there is no well-defined plasmon peak in the p-type sample

spectrum. It is known that the effective mass (m*) of conduction band holes is 0.35 m_e, while the effective mass of conduction band electrons is 0.068 m_e, where m_e is the mass of a free electron. Also the plasmon frequency $\propto \frac{1}{\sqrt{m^*}}$, which brings the hole-plasmon peak closer to the elastic peak and harder to see. The mobility of hole is much lower than the mobility of electron. Thus the damping effect for the hole-plasmon is significant larger compared to the electron-plasmon [53, 54].

The loss features in Fig. 44 also show a significant dependence on the primary beam energy. The intensity of the phonon decreases with higher primary beam energy, while the broad tail due to the hole-plasmon becomes stronger as the primary beam energy increases. This phenomenon can be explained by the probing depth of primary beam electron, which is proportional to $\sqrt{E_0}$ [67]. It means the probing electron with higher primary energy sees farther into the surface and detects the plasmon excitation below the depletion layer. As a consequence, the relative weight of the phonon becomes smaller, while the relative weight of the plasmon becomes larger.

Figure 45 displays the HREELS spectra for the clean GaAs(111)A surface and hydrogen-adsorbed surfaces with the different coverages, all taken at the primary beam energy of 6 eV. The loss at 35 meV is due to Fuchs-Kliewer phonons. This mode is insensitive to the crystal orientation or to chemisorption of hydrogen [68] because it is mainly a bulk and not a surface phenomenon. Hydrogen exposure leads to a prominent peak at 232 meV, which is assigned to the Ga-H stretching vibration [55]. The normalized intensity of Ga-H stretch peak is plotted as function of hydrogen exposure in Fig. 46. One can see that the intensity of Ga-H

stretch vibration increases monotonically as a function of hydrogen exposure. The exposure is saturated at about 500 L, which indicates that the Ga dangling bonds are saturated. No significant As-H stretch mode was observed. The intensity of the small feature around 260 meV is close to the noise level of the spectra, preventing an unambiguous identification of the As-H stretch mode. The same phenomenon was also reported in the results obtained from the sputtered/annealed GaAs(111)A surface [55].

GaAs(111)A is a Ga-terminated surface. Within the surface bilayer, each Ga and As atom has one dangling bond. In terms of the vacancy buckling model [48, 49], the As dangling bonds are directed to the hollow formed by Ga vacancy and the Ga dangling bonds point out from the bulk. Therefore, both Ga-H and As-H stretch modes are expected since the hydrogen adsorbs on the surface atoms via the dangling bonds of the surface atoms. However, there is only Ga-H peak in the HREELS spectra, and no significant As-H peak appears, which is not consistent with the XPS results. The XPS spectra indicate that As 3d core level is strongly affected by the hydrogen adsorption.

As mentioned in Ref. 55, the absence of As-H feature in the HREELS spectra is related to the surface vacancy buckling structure. The surface reconstruction forces the surface Ga atoms to reduce towards the bulk and the As atoms to rotate outwards from the bulk. As a result, the distance between the surface Ga layer and the surface As layer is only 0.07 Å (shown in Fig. 42(b)), compared to bulk bilayer distance of 0.816 Å. Assuming the surface Ga-As bond length is the bulk value of 2.45 Å, then the angle θ between the As dangling bond and the surface normal is 88.4^0. Therefore, the normal component of the As-H stretching

vibration is very small. It is known that dipole-scattering HREELS can only detect the stretching vibration component in the surface normal direction in terms of the selection rules[59]. Therefore, even if the As-H stretch modes do exist on the surface, it would be very difficult to detect them. This is why no well-defined As-H stretch mode was observed on the GaAs(111)A surface. However, for the surface Ga atoms, their dangling bonds are in the surface normal direction. Thus, the feature of Ga-H stretching vibration is very prominent in the HREELS spectra. Figure 47 illustrates this picture for the Ga-H and As-H stretch modes based on the vacancy buckling model of GaAs(111)A surface.

In addition, there is not enough room to hold three As-H units in one hollow caused by the vacancy of one Ga atom. There can be only one or two As atoms bonded with the hydrogen atoms in each hollow. This also contributes to the absence of the As-H peak in the HREELS spectra, since the amount of As-H units is much less than the amount of Ga-H units on the surface. Since any of the three As atoms in each hollow can equally well bond with the hydrogen atom, the positions of As-H units will be randomly distributed in three possibilities in each hollow. This breaks the surface long-range order and gives a 1x1 LEED structure. This effect is consistent with the intensity reduction of the HREELS elastic peak on the hydrogen-adsorbed surface.

From the above discussion, one can see that the hydrogen adsorption will saturate all the Ga dangling-bonds. Hence the Ga 3d core line in the XPS spectra appears with a chemical shift without any significant change in the shape, since the surface is all covered by Ga-H. However, for the surface As atoms, some will bond with the hydrogen atoms, while others do

not form As-H units. Thus there are both As-H units and surface As atoms with dangling bonds on the surface. As a consequence, the As 3d peak in the XPS spectra consists of three components: bulk, surface and As-H. That is why the As 3d peak becomes broader on the low kinetic energy side.

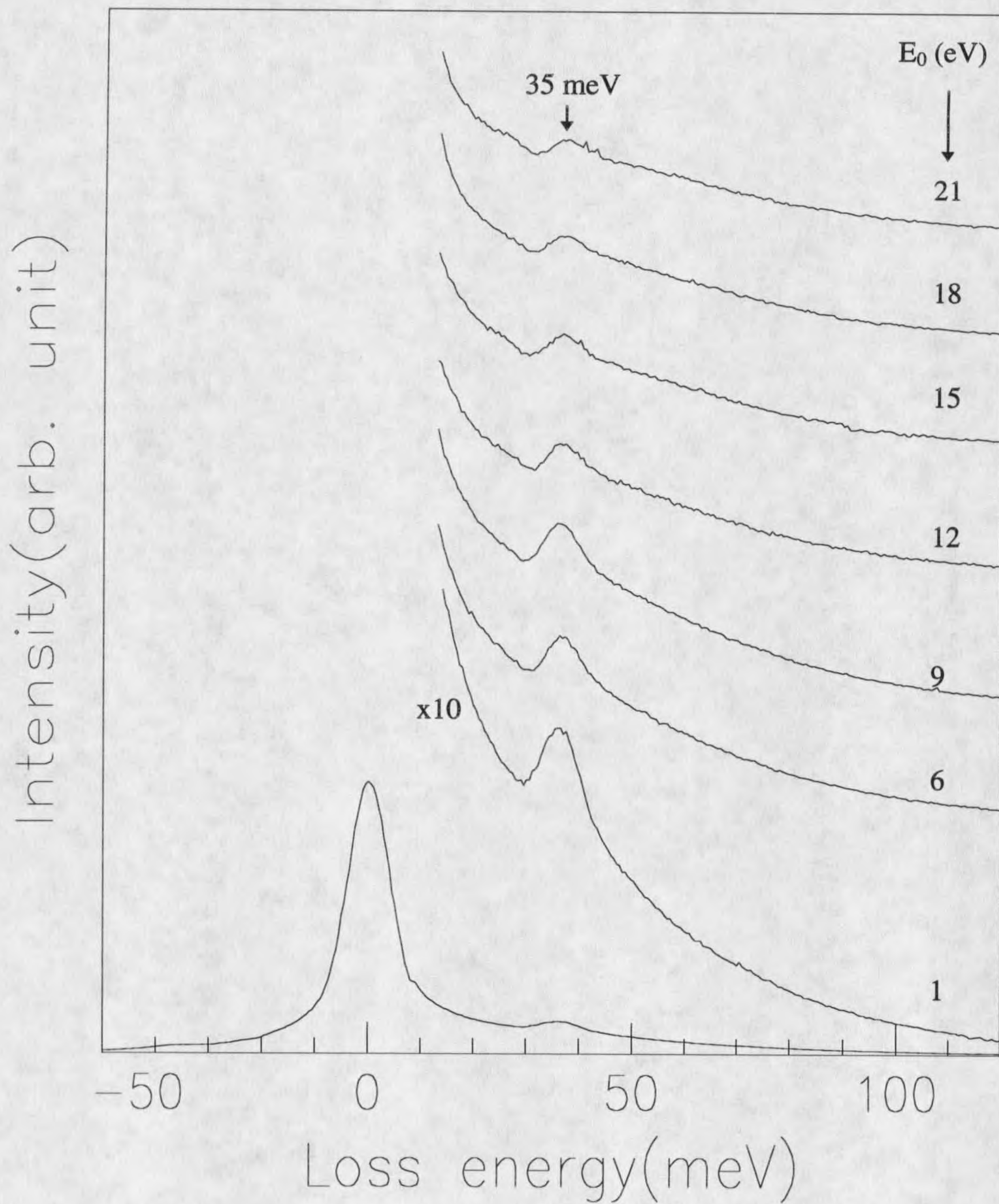

Fig. 44. HREELS spectra of the MBE-grown GaAs(111)A surface taken with different primary beam energies. The incident angle is 45^0.

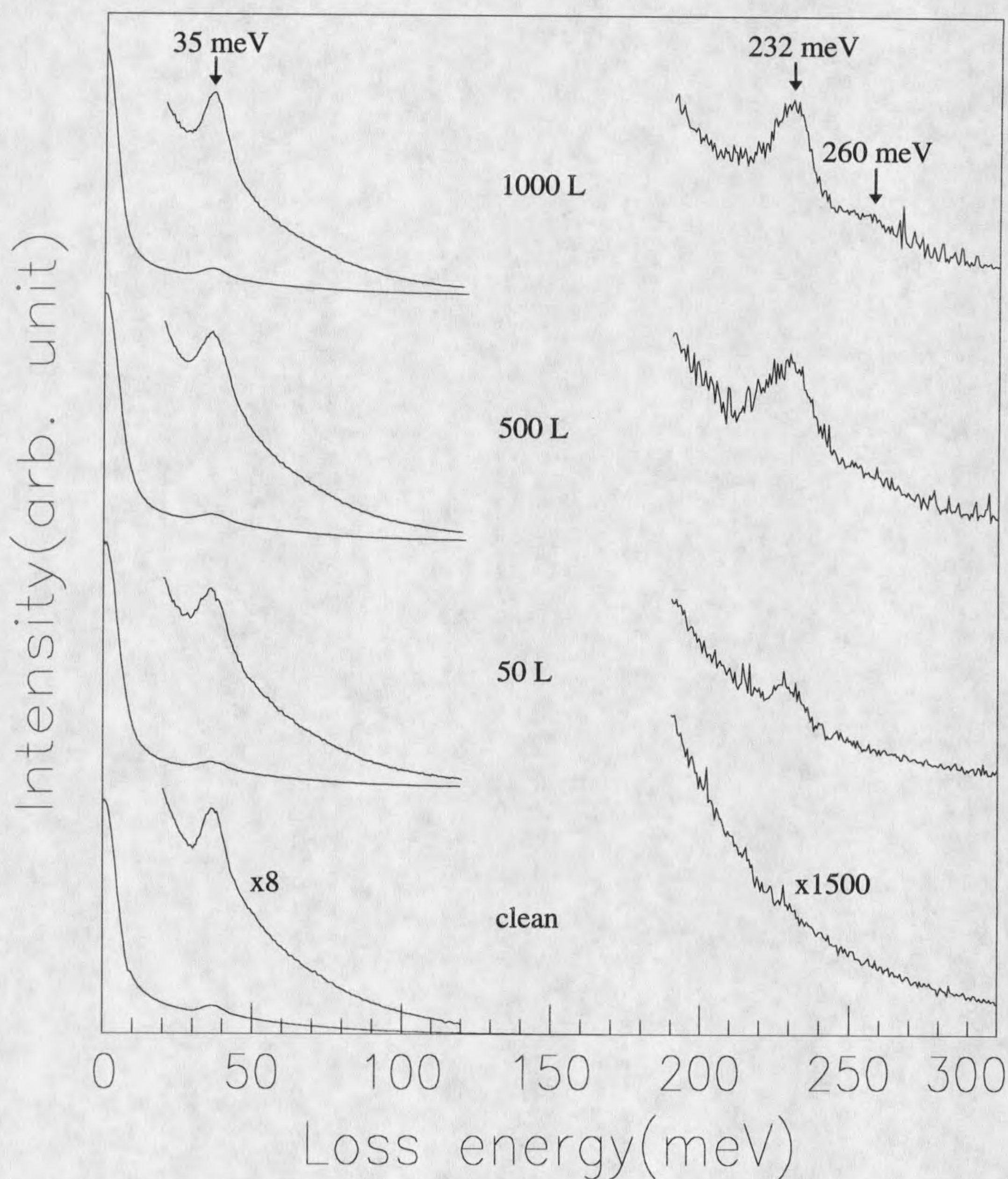

Fig. 45. HREELS spectra of the MBE-grown GaAs(111)A clean surface and subsequently hydrogen-adsorbed surfaces. The primary beam energy is 6 eV and the incident angle is 45^0.

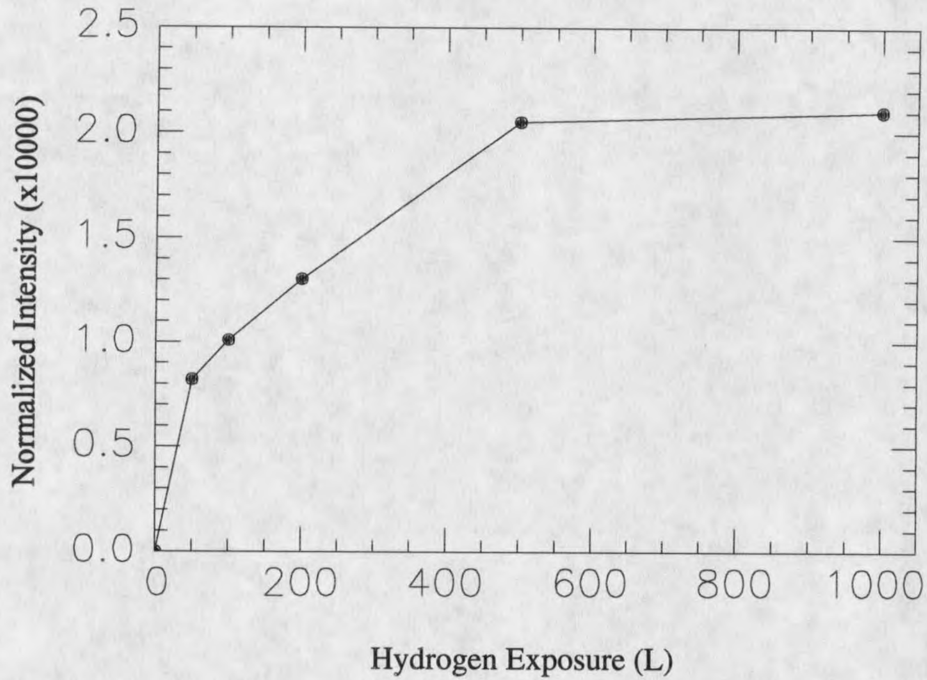

Fig. 46. The hydrogen uptake behavior for the MBE-grown GaAs(111)A surface. The intensity of Ga-H peak is normalized to the elastic peak.

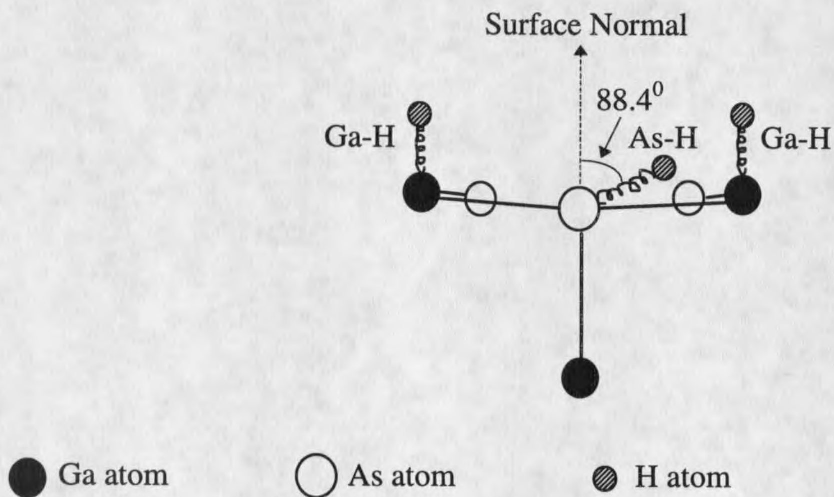

Fig. 47. Structure of hydrogen-adsorbed GaAs(111)A surface.

MBE-grown GaAs(111)B

The MBE growth on the GaAs(111)B substrate, at the growth temperature of 530^0C and the As/Ga flux ratio of 7.3, resulted in a 2x2 LEED pattern. The integrated intensity of As 3d and Ga 3d core levels were obtained from the XPS measurements. Then from Eq. (6.4), the ratio of the number of As atoms over the number of Ga atoms on the surface was calculated to be 1.8 (about 7/4). This result is in agreement with the As-trimer model of the GaAs(111)B-2x2 surface[57, 58]. This model claims that the As-rich 2x2 reconstruction of the GaAs(111)B has adsorbed As trimers at the T_4 sites bonded to the underlying surface As atoms. Figure 48 shows this structural model, and the dashed lines represent one unit cell. It can be seen that one unit cell has a total of seven As atoms, including three As adatoms, one As rest atom, and three first-layer As atoms, plus four Ga first-layer atoms on the surface. (The As rest atom refers to the surface As atom which does not bond with the As adatoms).

There was no significant change in the As/Ga ratio in the initial hydrogen adsorption (0-500 L), which indicated that no disruptive effect induced by atomic hydrogen adsorption occurred on the surface at this stage. The further hydrogen exposure caused a reduction in the value of As/Ga, which suggested the possible onset of a disruptive effect on the surface. UPS measurements showed that the surface Fermi-level was pinned at 0.7 eV above the valence band edge, that was the middle of the band gap. This value for the pinning position has been reported on GaAs(100) surface [61, 62]. The work function of the clean surface was measured

to be 4.5 eV. The hydrogen adsorption leading to the shift of the valence band edge resulted in the band-bending of 0.4 eV and it was saturated at about 1000 L. Such an energy-level diagram is depicted in Fig. 49.

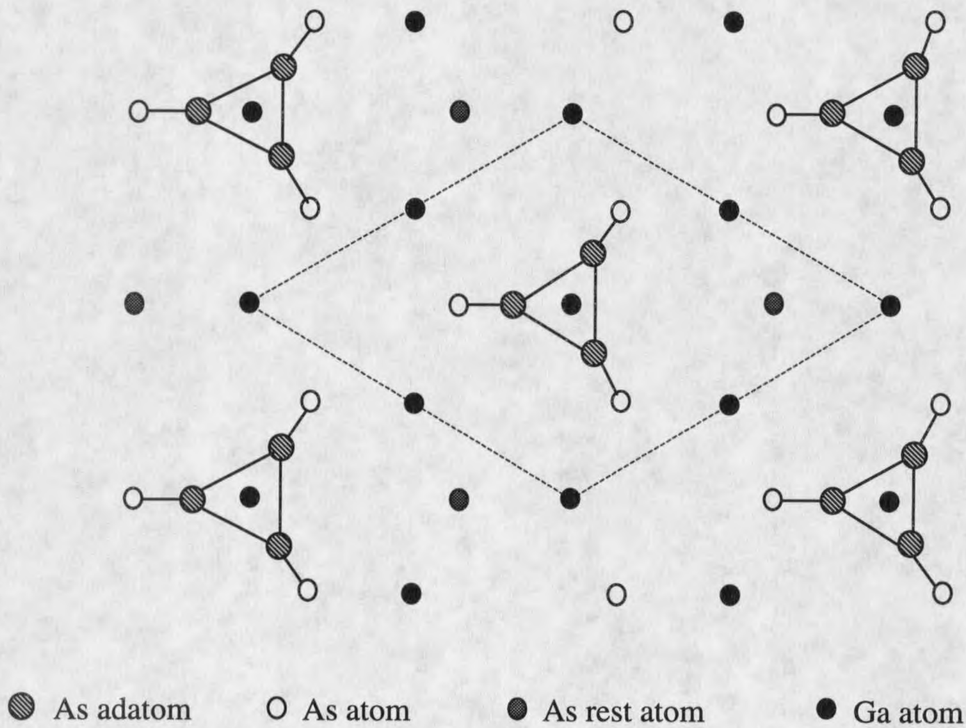

Fig. 48. Top view of the As trimer model of the GaAs(111)B-2x2 surface [57]. The dashed lines represent an unit cell.

Figure 50 shows the HREELS spectra of the MBE-prepared GaAs(111)B-2x2 surface for two different primary beam energies, E_0 = 9 eV and E_0 = 3 eV. Two main features are

evident in the spectra: the losses at 35.5 meV and 100 meV. A gain feature at -35.5 meV (anti-stokes), corresponding to the 35.5 meV loss feature, is the Fuchs-Kliewer surface phonon mode. Unlike the p-type GaAs(111)A sample, this n-type GaAs(111)B surface exhibits a very strong electron plasmon [59, 63] peak at 100 meV, due to the high Si-doping. The position of this plasmon is critically dependent on the carrier concentration as described in Eq. (6.3) and also the space charge distribution resulting from the band bending [69]. From this plasmon position of 100 meV and the band bending of 0.7 eV on the clean surface, the plasmon energy of 114 meV was obtained by extrapolating the plasmon energy to the flat band condition, using the data of Chen [69] for cleaved GaAs(110). This plasmon energy corresponds to a carrier concentration of 7.8×10^{18} cm^{-3}. Based on the value of the band bending and the carrier concentration, the thickness of depletion layer at the surface is found to be 130 Å [69].

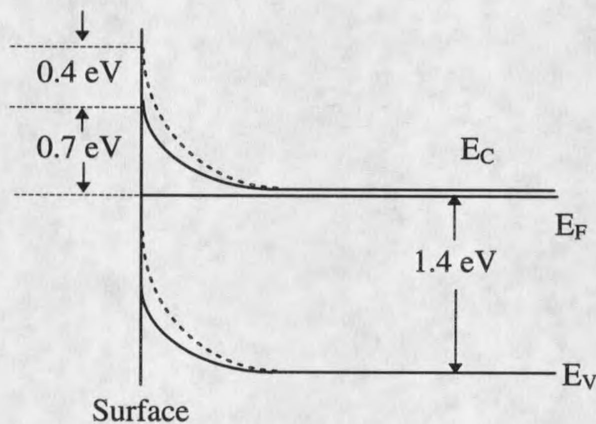

Fig. 49. Energy-level diagram at the surface for the n-type GaAs(111)B-2x2 semiconductor. The solid represents the band-bending of the clean surface, the dashed line represents the band-bending of the hydrogen-adsorbed surface.

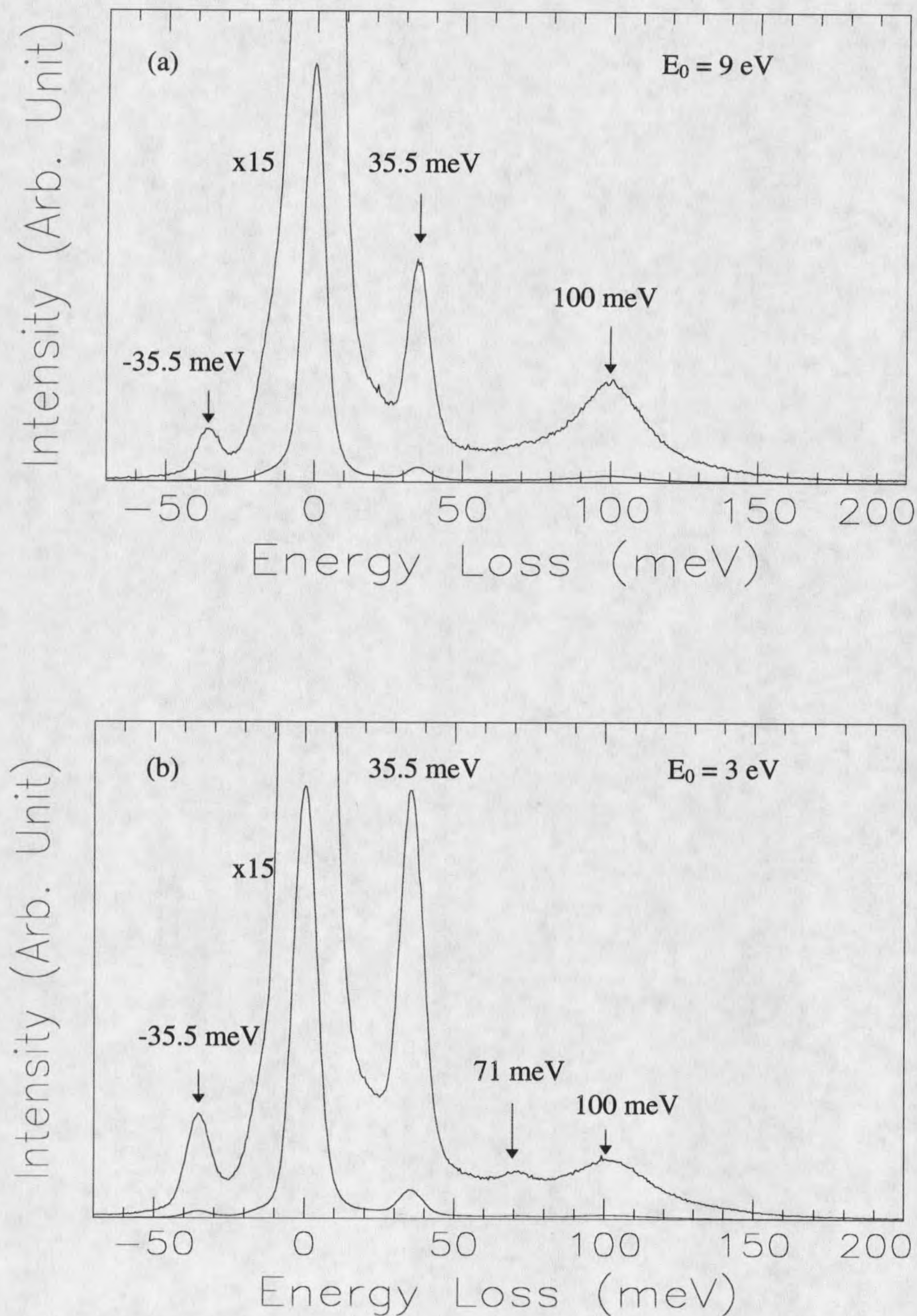

Fig. 50. HREELS spectra of the MBE-grown GaAs(111)B-2x2 at two different primary beam energies. The loss peak at 71 meV in (b) is due to the double phonon loss.

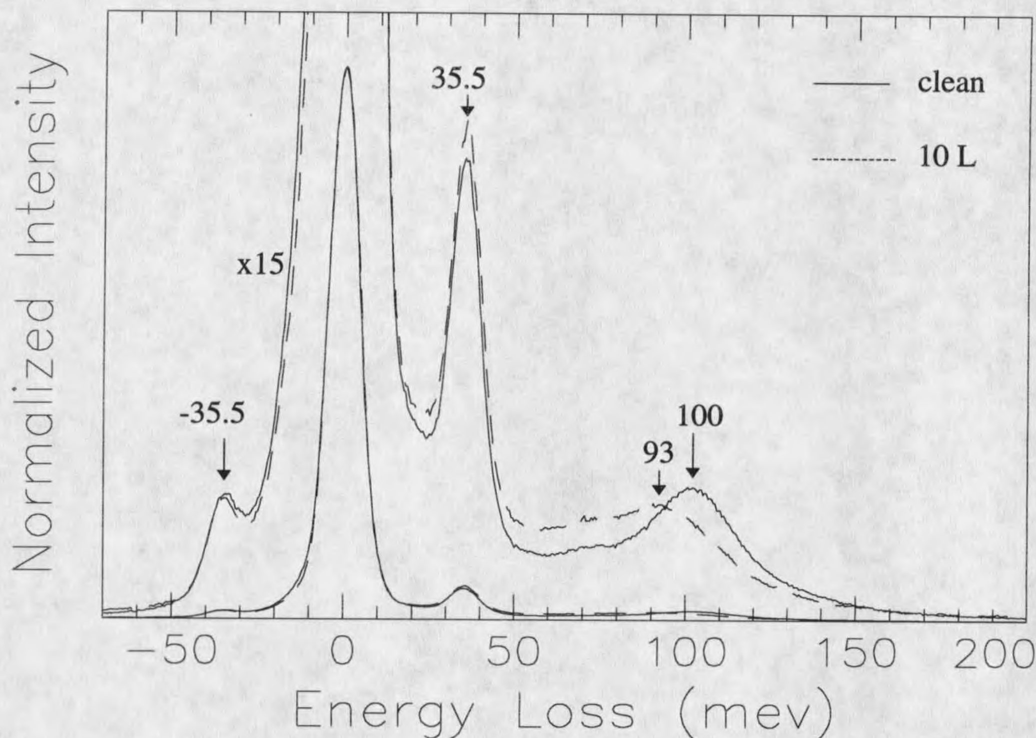

Fig. 51. HREELS spectra of the MBE-grown GaAs(111)B-2x2 before and after hydrogen exposure (10 L). The beam energy is 5.2 eV.

The feature at 71 meV in Fig. 50(b) is related to the second overtone of the surface phonon loss [70]. For the low beam energy, the probing depth is relatively small, so a larger portion of the phonons are unscreened by the free carrier plasmon since there is no free carrier in the depletion layer and makes a stronger contribution to the loss spectrum. While the plasmon is localized at the interface of the depletion layer, the plasmon loss weakens at the low beam energy. Hence, it is possible that the multiple phonon loss can appear in the

spectrum at a low beam energy. The intensity of the surface optical phonon is about 1.78 higher for $E_0 = 3$ eV as compared to that for $E_0 = 9$ eV. This is in good agreement with the $E_0^{-1/2}$ dependence for the excitation of surface phonon modes [59].

After a hydrogen exposure of 50 L a 1x1 LEED pattern was fully developed. It also caused the shift and attenuation of the plasmon peak [see Fig. 51], which are the result of depletion layer becoming thicker because of hydrogen adsorption. No shift was observed in the position of optical phonon peak. Based on two-layer model shown in Fig. 40, the plasmon energy is $\omega_{\mathrm{pl}}/\sqrt{1+\varepsilon(\infty)}$ for the sample without depletion layer at the surface, and $\omega_{\mathrm{pl}}/\sqrt{2\varepsilon(\infty)}$ for an infinitely thick depletion layer [69]. $\varepsilon(\infty)$ is the high frequency limit of the dielectric constant, which is 10.9 for GaAs. For a finite depletion layer thickness, the plasmon energy lies between the two limits. Thus as the depletion layer becomes thicker upon hydrogen exposure, the plasmon energy shifts down, and the intensity becomes weaker.

Both As-H (at 260 meV) and Ga-H (at 228 meV) stretch modes were fully developed with the hydrogen exposure up to 1000 L (see Fig. 52). This is quite different from the results obtained from the sputtered/annealed GaAs(111)B-1x1 surface [55], where the spectra were dominated by the Ga-H stretch mode, while the As-H stretch mode only showed a very small feature. This may be related to the surface stoichiometry and structure. According to the As-trimer model of the GaAs(111)B-2x2, there are 0.75 ML As adatoms on the As-terminated surface. Thus, the significant As-H loss feature is expected. The further hydrogen exposure beyond 600 L resulted in the small reduction of As-H peak intensity, which suggested that the

hydrogen adsorption started etching the surface by removing the surface As atoms. This is consistent with the results of the XPS measurements.

GaAs(111)B surface is not fully understood yet. There are still some different models about the surface reconstruction, two well-known structures are As-trimer model [57, 58] and Ga-vacancy model [64, 65]. Some recent theoretical calculation is in favor of the As-trimer model [66]. Our results from the XPS and HREELS measurements (the surface is covered with 3/4 ML As adatoms and the hydrogen disruption by breaking the As-backbonds) also favors the surface As-trimer reconstruction model.

Compared to the results obtained on the sputtered/annealed GaAs(111) surfaces [55], the MBE-grown GaAs(111)A surface shows a different surface reconstruction behavior upon hydrogen exposure. In addition, the MBE-grown GaAs(111)A surface reveals a hole-plasmon excitation, while the sputtered/annealed GaAs(111)A surface reveals an electron-plasmon excitation. For the GaAs(111)B surfaces, the sputtered/annealed preparation results in a 1x1 LEED pattern, while the MBE-growth results in a 2x2 LEED structure. Both Ga-H and As-H stretch modes are prominent in the HREELS spectra for the hydrogen adsorbed GaAs(111)B surface prepared by MBE-growth, while the only Ga-H stretch mode is significant in the HREELS spectra for the hydrogen adsorbed GaAs(111)B surface prepared by cycles of sputtering and annealing.

To conclude this chapter, high quality GaAs(111)A and GaAs(111)B surfaces have been obtained by MBE growth. At the same growth condition and with the same dopant, these two surfaces show the same 2x2 LEED pattern, but different types of free carriers. The free

carrier on the GaAs(111)A surface is hole (p-type), while the free carrier on the GaAs(111)B surface is electron. Hydrogen atoms interact with both surfaces via Ga and As dangling bonds. The absence of As-H stretch mode in HREELS spectra on the GaAs(111)A is related to the buckling vacancy structure. No hydrogen disruption has been found on the GaAs(111)A surface, while it does take place on the GaAs(111)B surface at heavy hydrogen exposure.

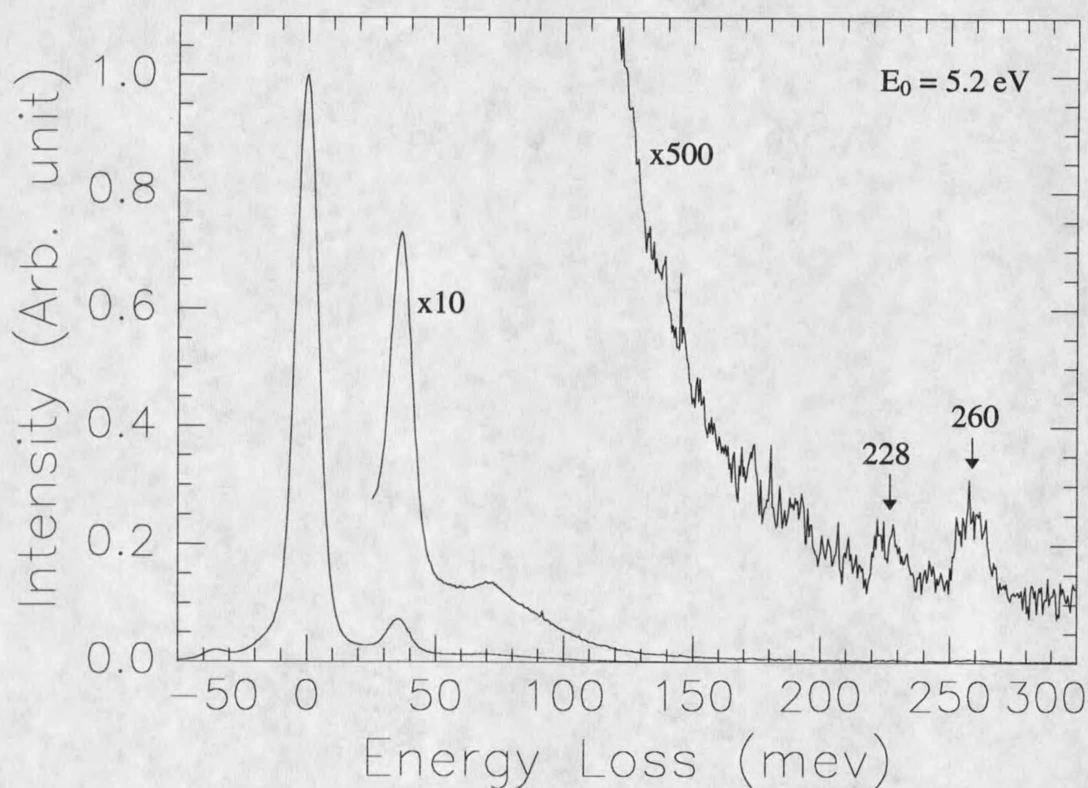

Fig. 52. HREELS spectrum of the MBE-grown GaAs(111)B surface with the hydrogen coverage of 1000 L. The feature at 260 meV is due to the As-H stretch vibration, the feature at 228 meV is due to the Ga-H stretch vibration.

CHAPTER 7

CONCLUSIONS

The first part of this thesis has dealt with the surface atomic structures of Se/Ge(100)-1x2, Ga/Ge(111)-1x1 and Ge/Si(100)-2x1 samples by the small-cone photoelectron holographic imaging (PHI) technique.

First, the interfacial structure of Se/Ge(100)-1x2 was studied by the PHI method and the results suggest that two kinds of regions coexist on the surface. The Se deposition breaks the Ge-Ge dimers on the surface, and some of the Se atoms occupy the bridge sites. This type of the region (Region I) is fully Se-terminated surface. In addition, the Ge atoms in some regions of the surface are displaced due to the Se adsorption, the Se atoms occupy the bridge sites in every other row (see Fig. 25) on the displaced surface, which results in a 1x2 LEED pattern. This type of the region (Region II) is half Se-terminated surface. This is the first time the surface atomic structure for Se/Ge(100) has been studied, and so there are no other experimental or theoretic results are available for comparison.

Next, the PHI technique was applied to determine the structure of Ga/Ge(111)-1x1. The images show that the Ga adsorbates occupy both the T_4 site and H_3 site. This implies that the surface does not have any long-range order due to the Ga adsorption at room temperature, which leads to a 1x1 LEED pattern. The parameters obtained from this work are close to the ones from the theoretical calculations, where the model is based on the assumption of the

single site structure (i.e. $\sqrt{3}x\sqrt{3}$ LEED pattern). This work extends the studying field of PHI technique to the disordered surfaces, since only the ordered surfaces have been investigated by this technique so far.

For the Ge/Si(100)-2x1 interfacial structure, the results show that Ge adsorption breaks the Si dimers and removes the surface Si atoms from the terraces. Then the Ge atoms occupy the bridge sites and form the Ge-Ge dimers very similar to the Si-Si dimers on the clean Si(100) surface. This determination is in agreement with the combined results of the studies by LEEM, LEED and STM [41].

In the second part of this thesis, the GaAs(111)A and GaAs(111)B surfaces, prepared by the molecular beam epitaxy growth technique, were investigated by HREELS, XPS, UPS and LEED.

The sharpness of spots and the background in the LEED patterns, as well as the elastic peak intensities in the HREELS spectra, indicate that the MBE growth has produced very high quality films. The results obtained from the XPS measurements have shown that the GaAs(111)A surface stoichiometry is consistent with the Ga-vacancy buckling model, and the surface stoichiometry of GaAs(111)B-2x2 is in agreement with the As-trimer model.

It has been shown that under the same growth conditions, the MBE growth with Si-doping produces a p-type semiconductor for GaAs(111)A and an n-type for GaAs(111)B, and both surfaces have the same 2x2 reconstruction after growth. For the p-type surface, the HREELS spectra do not show a prominent hole-plasmon peak, but rather a very strong wide tail; while for the n-type surface, a well-defined electron-plasmon feature emerges in the

HREELS spectra. Another observable difference between these two types of carriers appears in the UPS measurements. The energy levels of the conduction-band minimum and the valance-band maximum are bent downwards at the surface for the p-type and upwards for the n-type at the surfaces. The Fermi-level is pinned at 0.4 eV above the VBM for the GaAs(111)A surface, while the Fermi-level is pinned at the middle of the energy band gap for the GaAs(111)B surface.

The chemisorption of atomic hydrogen on these two surfaces has also been studied. It has been found that H adsorbs on both surface Ga and As atoms via their dangling bonds. Both As-H stretch mode at 260 meV and Ga-H stretch mode at 228 meV have been observed on the hydrogen adsorbed GaAs(111)B surface, while only the Ga-H stretch mode at 232 meV has been observed on the hydrogen adsorbed GaAs(111)A surface. Surface disruption due to removal of As atoms by hydrogen adsorption has been observed on GaAs(111)B surface, but it does not occur on GaAs(111)A surface.

In summary, we have successfully determined the interfacial atomic structures of some samples by the PHI technique, and have investigated the electronic properties of the MBE-grown GaAs(111)A-2x2 and GaAs(111)B-2x2 surfaces. The results obtained are valuable for further studies in the field of semiconductor surface science and technology.

REFERENCES

1. A. Liebsch, Phys. Rev. Lett. **32**, 1203 (1974).

2. A. Szoke, *in Short Wavelength Coherent Radiation: Generation and Applications*, edited by D. T. Attwood and J. Boker, AIP Conference Proceedings No. 147.

3. G. R. Harp, D. K. saldin and B. P. Tonner, Phys. Rev. Lett. **65**, 1012 (1990).

4. S. Thevuthasan, R.X. Ynzunza, E. D. Tober, C. S. Fadley, A. P. Kaduwela and M. A. Van Hove, Phys. Rev. Lett. **70**, 5 (1993).

5. S. Y. Tong, C. M. Wei, T. C. Zhao, H. Huang and Hua Li, Phys. Rev. Lett. **66**, 60 (1991).

6. G. S. Herman, S. Thevuthasan, T. T. Tran, Y. J. Kim and C. S. Fadley, Phys. Rev. Lett. **68**, 650 (1992).

7. S. Y. Tong, H. Huang and C. M. Wei, Phys. Rev. B **46**, 2452 (1992).

8. H. Wu, G. J. Lapeyre, H. Huang and S. Y. Tong, Phys. Rev. Lett. **71**, 251 (1993).

9. H. Wu and G. J. Lapeyre, Phys. Rev. B **51**, 14549 (1995).

10. H. Wu, Ph. D. thesis *Direct Determination of Adsorbate Positions with Energy-dependent and Angle-resolved Photoelectron Diffraction*, Montana State University-Bozeman, 1994.

11. H. Yu, Ph. D. thesis *Application of Photoelectron Holographic Imaging to the Study of Si(100) Interfacial Structures*, Montana State University-Bozeman, 1995.

12. M. T. Sieger, J. M. Roesler, D. S. Lin, T. Miller and T. C. Chiang, Phys. Rev. Lett. **73**, 3117 (1994).

13. D. A. Woolf, D. I. Westwood and R. H. Williams, Semicond. Sci. Technol. **8**, 1075 (1993).

14. M. R. Fahy, J. H. Neave, M. J. Ashwin, R. Murray, R. C. Newman and B. A. Joyce, J. Crystal Growth **127**, 871 (1993).

15. K. Yang and L. J. Schowalter, Appl. Phys. Lett. **60**, 1851 (1992).

16. E. A. Caridi, T. Y. Chang, K. W. Goossen and L. F. Eastman, Appl. Phys. Lett. 56, 659 (1990).

17. T. Hayakawa, M. Kondo, T. Suyama, K. Takahashi, S. Yamamoto and T. Hijikata, J. Appl. Phys. **26**, L302 (1987).

18. S. Y. Tong, Prog. Surf. Sci. **7**, 1 (1975).

19. D. Park, *Introduction to the Quantum Theory*, McGraw-Hill, Inc. (1974).

20. J. J. Sakurai, *Modern Quantum Mechanics*, The Benjamin/Cummings Publishing Company, Inc. (1985).

21. C. M. Wei, T. C. Zhao and S. Y. Tong, Phys. Rev. B **43**, 6354 (1991).

22. G. J. Lapeyre, A. D. Baer, J. Anderson, J. C. Hermanson, J. A. Knapp and P. L. Gobby, Solid State Communication **15**, 1601 (1974).

23. Z. Hussain, D. A. Shirley, C. H. Li and S. Y. Tong, Proc. Natl. Acad. Sci. U.S.A. **78**, 5293 (1981).

24. Users Guide, Synchrotron Radiation Center, University of Wisconsin-Madison.

25. C. G. Olson, Nuclear Instruments and Methods in Physics Research A**266**, 205 (1988).

26. M. Cardona and L. Ley, *Photoemission in Solids I* (Spring-Verlag, 1978).

27. J. E. Griffith and G. P. Kochanski, Critical Rev. in Solid State and Materials Sci. **16**, 255 (1990).

28. D. E. Aspnes and J. Ihm, Phys. Rev. Lett. **57**, 3054 (1986).

29. GENPLOT software package from Computer Graphic Service, 52 Genung Circle, Ithaca, NY 14850.

30. MATHEMATICA, Wolfram Research Inc., 100 Trade Center Dr., Champaign, IL 61820.

31. C. T. Foxon and B. A. Joyce, Surf. Sci. **64**, 293 (1977).

32. H. Ibach, Phys. Rev. Lett. **24**, 1416 (1970).

33. H. Froitzheim, *Topics in Current Physics*, Vol. 4, Springer-Verlag, New York, 1976.

34. *Instruction and Operation Manual for ELS 86-40-01*, Leybold-Heraeus.

35. D. A. Woolf, D. I. Westwod and R. H. Williams, Appl. Phys. Lett. **62**, 1370 (1993).

36. H. Kroemer, *Materials Research Society Symposium Proceedings: Heteroepitaxy on Silicon*, Vol. **67**, J. C. C. Fan and J. M. Poate, eds., Pittsburgh, PA 1986.

37. R. D. Bringans, Critical Rev. in Solid State and Materials Sci. **17**, 353 (1992). R. D. Bringans and M. A. Olmstead, Phys. Rev. B **39**, 12985 (1989).

38. J. P. LaFemina, Surf. Sci. Reports **16**, 133 (1992).

39. M. T. Sieger, J. M. Roesler, D. -S. Lin, T. Mille and T. -C. Chiang, Phys. Rev. Lett. **73**, 3117 (1994).

40. J. M. Ricart, J. Rubio and F. Illas, Phys. Rev. B **42**, 5212 (1990).

41. R. M. Tromp, Phys. Rev. B **47**, 7125 (1993).

42. R. M. Tromp and M. C. Reuter, Phys. Rev. Lett. **68**, 954 (1992).

43. M. W. Grant, D. J. Dieleman, M. A. Boshart and L. E. Seiberling, Phys. Rev. B **49**, 16534 (1994).

44. E. Fontes, J. R. Patel and F. Comin, Phys. Rev. Lett. **70**, 2790 (1993).

45. T. Ishibashi, S. Tarucha and H. Okamoto, Japanese J. Appl. Phys. **21**, L476 (1982).

46. M. Ogawa and T. Baba, Japanese J. Appl. Phys. **24**, L572 (1985).

47. W. I. Wang, E. E. Mendez, T. S. Kuan and L. Esaki, Appl. Phys. Lett. **47**, 826 (1985).

48. S. Y. Tong and W. N. Mei, J. Vac. Sci. Technol. B **2**, 393 (1984).

49. S. Y. Tong, G. Xu, W. Y. Hu and M. W. Puga, J. Vac. Sci. Technol. B **3**, 1076 (1985).

50. R. D. Bringans and R. Z. B achrach, J. Vac. Sci. Technol. A **1**, 676 (1983).

51. O. F. Sankey, R. E. Allen, S. F. Ren and J. D. Dow, J. Vac. Sci. Technol. **133**(4), 1162 (1985).

52. S. Y. Tong, W. N. Mei and G. Xu, J. Vac. Sci. Technol. B **2**, 393 (1984).

53. Y. Meng, J. R. Anderson, J. C. Hermanson and G. J. Lapeyre, Phys. Rev. B **44**, 4040 (1991).

54. R. Biagi, C. Mariani and U. del Pennino, Phys. Rev. B **46**, 2467 (1992).

55. D. J. Frankel, J. Anderson, G. J. Lapeyre and H. H. Farrel, J. Vac. Sci. Technol. B **3**, 1093 (1985).

56. J. J. Yeh and I. Lindau, Atomic Data and Nuclear data Tables **32**, 1-155 (1985).

57. D. K. Biegelsen, R. D. Bringans, J. E. Northrup and L.-E. Swartz, Phys. Rev. Lett. **65**, 452 (1990).

58. J. M. C. Thornton, P. Weightman, D. A. Woolf and C. J. Dunscombe, Phys. Rev. B **51**, 14459 (1995).

59. H. Ibach and D. L. Mills, *Electron Energy Loss Spectroscopy and Surface Vibrations*, Academic Press, 1982. H. Ibach, *Electron Spectroscopy for Surface Analysis*, Springer-Verlin, Berlin, 1977).

60. H. Lüth and R. Matz, Phys. Rev. Lett. **46**, 1652 (1981).

61. R. D. Bringans and R. Z. Bachrach, J. Vac. Sci. Technol. A **1**, 676 (1983).

62. S. P. Svensson, J. Kanski, T. G. Anderson and P. O. Pearton, J. Vac. sci. technol. B **2**, 235 (1984).

63. Y. Chen, S. Nannarone, J. A. Schaefer, J. C. Hermanson and G. J. Lapeyre, Phys. Rev. B **39**, 7653 (1989).

64. D. J. Chadi, Phys. Rev. Lett. **52**, 1911 (1984); Phys. Rev. Lett. **57**, 102 91986).

65. A. D. Katnani and D. J. Chadi, Phys. Rev. B **31**, 2554 (1985).

66. E. Kaxiras, Y. Bar-Yam, J. D. Joannopoulos and K. C. Panday, Phys. Rev. B **35**, 9625 (1987).

67. Y. Meng, Ph. D. thesis *Study of Collective Excitations and Schottky Barrier Formation at III-V Semiconductor Surfaces and Interfaces*, Montana State University-Bozeman, 1991.

68. L. H. Dubois and G. P. Schwartz, Phys. Rev. B **26**, 794 (1982).

69. Y. Chen, Ph. D. thesis *Space Charge Layers and Hydrogen Adsorption on the Cleavage*

Surfaces of III-V Compound Semiconductors, Montana State University-Bozeman, 1989.

70. L. H. Dubois, and G. P. Schwartz, Phys. Rev. B **26**, 794 (1982).

71. R. S. Becker, T. Klitsner, and J. S. Vickers, J. Microsc. **152**, 157 (1988).

72. R. M. Tromp, A. Denier van der Gon and M.C. Reuter, Phys. Rev. Lett. **68**, 2313 (1992).

MONTANA STATE UNIVERSITY LIBRARIES
3 1762 10229542 3